

# Searching for the Cosmic Dawn

Thesis by  
Michael William Eastwood

In Partial Fulfillment of the Requirements for the  
Degree of  
Doctor of Philosophy in Astrophysics

The Caltech logo, consisting of the word "Caltech" in a bold, orange, sans-serif font.

CALIFORNIA INSTITUTE OF TECHNOLOGY  
Pasadena, California

2019  
Defended September 3, 2018

© 2019

Michael William Eastwood  
ORCID: 0000-0002-4731-6083

Some rights reserved. This thesis is distributed under a “Creative Commons Attribution-ShareAlike License”

## ACKNOWLEDGEMENTS

This thesis would not have been possible without the support of my family and friends.

First, and most importantly, *thank you* to my parents whom have always been my first port of call for advice and support. *Thank you* to Shawn for his extraordinary patience in helping me pass my first physics class, and teaching me through example that math is rewarding (although I still maintain my assertion that math is a subfield of physics). *Thank you* to Kevin for being my lifelong friend.

*Thank you* to my entire thesis committee, but especially to my advisor Gregg Hallinan.

Sebastian

Melodie

Jackie

*Thank you* to Marin Anderson for being a wonderful friend and peer. We started on the OVRO-LWA project together,

Ryan M

*Thank you* to Stephen Bourke and Jake Hartman without whom the OVRO-LWA would not be the instrument it is today. *Thank you* to Harish Vedantham whose patient and thorough discussions with me were often extremely influential in helping me find new direction in my research.

*Thank you* to the entire Owens Valley Radio Observatory staff, without whom the OVRO-LWA would not even exist.

*Thank you* to Richard Shaw for developing the *m*-mode analysis framework that was foundational for this thesis, and to Adrian Liu who first introduced me to his work.

*Thank you* to Gita Patel and Althea Keith for dealing with my occasional delinquency.

*Thank you* to Patrick Shopbell

*Thank you* to my mentor Ryan Trainor, who in spite of the fact that he is a Liverpool fan, helped me settle and find my feet within the Caltech community. *Thank you* to Jacob Jencson and Chris Bochenek

Caltech peoples Yi

Judd, Tzu-Ching, Sievers

Maci, Eva, John

*Thank you* to professors Marjorie Corcoran, Christopher Johns-Krull, Patrick Hartigan, James Hannon, Mark Embree, and Anthony Chan who collectively guided me through my time at Rice University.

*Thank you* to everybody who has played on the Cataclysmics soccer team. We occasionally won a game or two. Maybe results will improve with the new management.

Finally, *thank you* to Jessica Tran for helping me grow in my faith and praying the rosary with me daily.

## ABSTRACT

[This abstract must provide a succinct and informative condensation of your work. Candidates are welcome to prepare a lengthier abstract for inclusion in the dissertation, and provide a shorter one in the CaltechTHESIS record.]

## PUBLISHED CONTENT AND CONTRIBUTIONS

[Fill this out with my publications]

## TABLE OF CONTENTS

<b>Acknowledgements</b>	<b>iii</b>
<b>Abstract</b>	<b>v</b>
<b>Published Content and Contributions</b>	<b>vi</b>
<b>Table of Contents</b>	<b>vii</b>
<b>List of Illustrations</b>	<b>ix</b>
<b>List of Tables</b>	<b>xix</b>
<b>Chapter I: Introduction</b>	<b>1</b>
1.1 Fundamental Physics . . . . .	1
1.2 A History of the Universe through the 21 cm Transition . . . . .	3
1.3 First Generation 21 cm Experiments . . . . .	6
1.4 Observational Challenges . . . . .	12
1.5 Future Outlook . . . . .	17
<b>Chapter II: A Path Towards Calibration of the OVRO-LWA</b>	<b>24</b>
2.1 Design and Construction of the OVRO-LWA . . . . .	24
2.2 Calibration of a Low-Frequency Interferometer . . . . .	26
2.3 Source Removal and Direction-Dependent Calibration . . . . .	31
2.4 Commissioning Challenges . . . . .	32
<b>Chapter III: The Radio Sky at Meter Wavelengths: <i>m</i>-mode Analysis</b>	
<b>Imaging with the OVRO-LWA</b>	<b>36</b>
3.1 Introduction . . . . .	37
3.2 All-sky Imaging . . . . .	39
3.3 Observations . . . . .	50
3.4 Results . . . . .	60
3.5 Error Analysis . . . . .	77
3.6 Conclusion . . . . .	84
<b>Chapter IV: The 21 cm Power Spectrum from the Cosmic Dawn: First Results from the OVRO-LWA</b>	<b>89</b>
4.1 Introduction . . . . .	89
4.2 Observations . . . . .	91
4.3 Formalism . . . . .	95
4.4 Covariance Matrices . . . . .	99

4.5 Foreground Filtering . . . . .	106
4.6 Results and Error Analysis . . . . .	111
4.7 Conclusion . . . . .	121
<b>Acknowledgments</b>	<b>122</b>
.1 Converting a Spatial Power Spectrum to an Angular Power Spectrum	122
<b>Appendix A: Conclusion</b>	<b>128</b>

## LIST OF ILLUSTRATIONS

<i>Number</i>	<i>Page</i>
1.1 (top) A simulated light cone of the 21 cm brightness temperature illustrating the anisotropy in the expected signal. (bottom) A simulation of the globally averaged brightness temperature due to the high redshift 2 cm transition. This figure is reproduced with permission from Pritchard & Loeb (2012). . . . .	3
1.2 An <i>H</i> -band image of GN-z11, the most distant spectroscopically confirmed galaxy with the dispersion direction for the Hubble Space Telescope grism spectra that confirmed that this galaxy originates from $z \approx 11.1$ . This figure is reproduced from Oesch et al. (2016). <b>get permission to republish this figure</b> . . . . .	6
1.3 A collection of spectra for high-redshift quasars illustrating the trend towards a completely saturated Gunn–Peterson trough with increasing redshift, but variations between quasars at comparable redshifts provide evidence for patchy reionization. This figure is reproduced from Fan et al. (2006). <b>get permission to republish this figure</b> . . . . .	7
1.4 Power spectrum amplitude upper limits (95% confidence or lowest systematically limited data point) as a function of redshift. The shaded region denotes roughly where current theoretical predictions fall. . . . .	11
1.5 (a) Illustration of the foreground wedge. The emission near the edge of the foreground wedge typically originates from sources located far from the delay center. (b) Illustration of the contamination arising after calibration errors. Emission leaks out of the foreground wedge and into the otherwise clean “EoR Window.” Reproduced from Morales et al. (2012) (permission not yet received). . . . .	14
1.6 (a) The calibrated sky spectrum measured by the EDGES experiment. (b) The residuals after fitting a model of the foreground emission. (c) The residuals after performing a joint fit of the foreground emission and an absorption trough. (d) The best-fit absorption trough. (e) The best-fit absorption trough including residual noise. This figure is reproduced with permission from Bowman et al. (2018). . . . .	18

1.7	A radial map of the universe. Known quasars are marked with circles and galaxies are marked with stars. The range of comoving distances probed by the OVRO-LWA and HERA are marked with a red rectangle and a blue rectangle respectively. . . . .	20
2.1	The first OVRO-LWA completed on 2013 March 8 with the class of Ay 122b (including the author of this thesis with the fractured ankle). . . . .	24
2.2	Picture of an OVRO-LWA antenna. . . . .	25
2.3	Snapshot image of the sky captured with the OVRO-LWA and using only the antennas located within the core of the array. The image covers the entire visible hemisphere in sine-projection. A similar image constructed using the newer long-baseline antennas can be seen in Figure 2.4. . . . .	27
2.4	Snapshot image of the sky captured with the OVRO-LWA and using the new long-baseline antennas. The image covers the entire visible hemisphere in sine-projection. A similar image constructed using only the core of the interferometer can be seen in Figure 2.3. . . . .	28
2.5	Illustration of the error in the WCS prior to a correction to the antenna positions. The image is a difference between an image constructed with the incorrect antenna positions and the corrected antenna positions. The arrow denotes the direction and approximate center of the rotation. . . . .	33
2.6	(a) The localization region for a source of RFI south of the OVRO-LWA and near the town of Big Pine. Satellite imagery ©2018 Google. Map data ©2018 Google. (b) Image of a high-voltage power line overlooking OVRO near the localization region. . . . .	33
3.1	Example L curve computed from OVRO-LWA data at 36.528 MHz by trialing 200 different values of the regularization parameter $\varepsilon$ . The x-axis is the norm of the solution (in this case, the spherical harmonic coefficients) given in arbitrary units, and the y-axis is the least-squares norm given in arbitrary units. Where the regularization parameter is small, the norm of the solution grows rapidly. Where the regularization parameter is large, the least-squares norm grows rapidly. . . . .	45

- 3.2 Antenna layout for the OVRO-LWA. Black dots correspond to antennas within the 200 m diameter core of the array. The 32 triangles are the expansion antennas built in early 2016 in order to increase the longest baseline to  $\sim 1.5$  km. The red dots are core antennas that are disconnected from the correlator in order to accommodate these antennas. The five crosses are antennas equipped with noise-switched front ends. . . . . 51
- 3.3 The  $m$ -mode analysis imaging PSF at three declinations (top row:  $\delta = +75^\circ$ , middle row:  $\delta = +45^\circ$ , bottom row:  $\delta = +0^\circ$ ) and three frequencies (left column: 36.528 MHz, middle column: 52.224 MHz, right column: 73.152 MHz). The PSF is computed by evaluating Equation 3.16. Above 55 MHz, the angular extent of the PSF does not follow the expected scaling with frequency because the angular resolution is limited by the selection of  $l_{\max} = 1000$ . The FWHM at  $\delta = +45^\circ$  is listed in Table 3.1. . . . . 52
- 3.4 Empirical fits to the OVRO-LWA Stokes  $I$  primary beam (the response of the  $x$  and  $y$  dipoles has been summed) at three frequencies: 36.528 MHz (left panel), 52.224 MHz (middle panel), and 73.152 MHz (right panel). The source tracks used to measure the beam model are overlaid. From north to south, these tracks correspond to Cas A, Cyg A, 3C 123, Tau A, Vir A, Her A, 3C 353, and Hya A. The fitting process is described in §3.3, and residuals for Cyg A and Cas A are in Figure 3.5. . . . . 54
- 3.5 Panels (a) and (b) show the measured apparent flux of Cyg A and Cas A at 36.528 MHz (red points) and 73.152 MHz (blue points) as a function of time over the observing period. The solid black curves show the expected flux computed using the empirical beam model fits. The thermal noise contribution to each point is about 50 Jy. Cyg A is occulted by the White Mountains when it is low on the horizon to the east. Panels (c) and (d) show the measured position offset of Cyg A and Cas A relative to their true astronomical positions at 36.528 MHz (red line) and 73.152 MHz (blue line). . . . . 55
- 3.6 Median vertical TEC within 200 km of OVRO during the time of the observation. The gray shaded regions indicate times outside of the observing period. The gray vertical lines indicate sunrise and sunset (as labeled). . . . . 56

3.7	Measured fluxes (black points) of 11 sources plotted against the published spectra from Perley & Butler (2017) (solid line above 50 MHz, dotted line below 50 MHz), Scaife & Heald (2012) (dashed line), and Baars et al. (1977) (dot-dashed line). Cas A is compared against a spectrum assuming a secular decrease of 0.77% per year (Helmboldt & Kassim, 2009).	59
3.8	These eight panels illustrate (with a Mollweide projection and logarithmic color scale) the eight full-sky maps generated with Tikhonov-regularized $m$ -mode analysis imaging and the OVRO-LWA. Each map covers the sky north of $\delta = -30^\circ$ with angular resolution of $\sim 15'$ . Eight bright sources have been removed from each map (Cyg A, Cas A, Vir A, Tau A, Her A, Hya A, 3C 123, and 3C 353). The small blank region near $l = +45.7^\circ$ , $b = -47.9^\circ$ corresponds to the location of the Sun during the observation period. A detailed summary of the properties of each map is given in Table 3.1.	62
3.8	continued	63
3.8	continued	64
3.8	continued	65
3.8	continued	66
3.8	continued	67
3.8	continued	68
3.8	continued	69
3.9	This Mollweide-projected map is constructed from three maps of the sky at 36.528 MHz (red), 52.224 MHz (green), and 73.152 MHz (blue). The maps are scaled by $\nu^{2.5}$ before combining, and the color scale is logarithmic (as in Figure 3.8). Therefore, regions with a spectral index of $-2.5$ will tend to appear white, and regions with a flatter spectral index will tend to appear blue.	70
3.10	Cutout of the galactic plane from Figure 3.9.	71

- 3.11 Local spectral index measured between the 36.528 MHz map and the 73.152 MHz map estimated by means of a local T-T plot. The color scale gives the spectral index, where blue is flat spectrum and red is steep spectrum. The contours give the coefficient of determination ( $R^2$ ) for the linear fit to the local T-T plot. If  $R^2$  is low, the quality of the fit is low, and the estimated spectral index is unreliable. This can be due to either insufficient dynamic range in the local T-T plot or multiple emission mechanisms operating in close proximity. Consequently,  $R^2$  tends to drop at higher galactic latitudes (due to dynamic range) and near H II regions in the galactic plane (due to multiple emission mechanisms). . . . . 72
- 3.12 Local spectral index measured between the 73.152 MHz OVRO-LWA map and the reprocessed 408 MHz Haslam map (Remazeilles et al., 2015). The color scale gives the spectral index, where blue is flat spectrum and red is steep spectrum. The contours give the coefficient of determination ( $R^2$ ) for the linear fit to the local T-T plot. See the caption of Figure 3.11 for more details about the coefficient of determination. . . . . 73
- 3.13 Fractional difference between maps from the LLFSS and the OVRO-LWA maps (Figure 3.8) after interpolating to the corresponding frequency and smoothing to the corresponding resolution. A positive value indicates regions where the OVRO-LWA map has more emission than the corresponding LLFSS map. Cas A, Cyg A, Vir A, and Tau A are masked due to the fact that they are subtracted from the OVRO-LWA maps. . . . . 75
- 3.14 This Mollweide-projected map compares the fractional difference between the Guzmán 45 MHz map and the OVRO-LWA maps (Figure 3.8) interpolated to 45 MHz (degraded to  $5^\circ$  resolution). A positive value indicates regions where the OVRO-LWA map has more emission than the Guzmán map, and a negative value indicates regions where the Guzmán map has more emission than the OVRO-LWA map. Cas A, Cyg A, Vir A, and Tau A are masked due to the fact that they are subtracted from the OVRO-LWA maps but not the Guzmán map. . . . . 76

- 3.15 Illustration of the corrupting influence of the ionosphere at 36.528 MHz (left column) compared with 73.152 MHz (right column). Each panel shows the simulated PSF for a source at the location of Cas A and illustrates the percent difference (relative to the peak flux of the uncorrupted PSF) due to including an ionospheric effect. In the top row, the simulated source scintillates using the measured light curve for Cas A in Figure 3.5. In the bottom row, the simulated source is refracted from its true position using the measured refractive offsets for Cas A in Figure 3.5. . . . . 78
- 3.16 Zoom-in of 3C 134 at 36.528 MHz (left panel), 52.224 MHz (middle panel), and 73.152 MHz (right panel). At 36.528 MHz there are  $\sim 10\%$  artifacts around 3C 134 that persist after CLEANing due to ionospheric effects. As expected for an ionospheric origin, these artifacts decrease in amplitude as frequency increases. Figure 3.15 shows the typically expected amplitude of these effects for ionospheric scintillation and refractive offsets. . . . . 79
- 3.17 Terrestrial sources of correlated noise that are apparent after averaging the visibilities at 62.688 MHz over the entire 28 hour observing period (keeping the phase center at zenith such that astronomical sources of radio emission are smeared along tracks of constant declination). Each panel represents a different component that is removed from the visibilities. The images are generated using WSClean (Offringa et al., 2014), uniform weighting, and only baselines longer than 15 wavelengths. Panels (a) and (b) illustrate components that appear noise-like in image space, but are in fact a constant offset to the measured visibilities likely associated with cross-talk or common-mode pickup. Panel (c) illustrates a component that is clearly associated with an RFI source on the horizon to the west–northwest of the OVRO-LWA. This RFI source is likely an arcing power line. Figure 3.18 illustrates the characteristic ringlike artifacts introduced into the maps if these three components are not removed prior to  $m$ -mode analysis imaging. The component shown in panel (a) has about twice the amplitude ( $\|\mathbf{v}_{\text{terrestrial}}\|$ ) of those in panels (b) and (c), and for all three components,  $\|\mathbf{B}^*\mathbf{v}_{\text{terrestrial}}\| / (\|\mathbf{B}\| \|\mathbf{v}_{\text{terrestrial}}\|) \sim 0.035$ . . . . . 82

- 3.18 A Mollweide-projected image of the artifacts introduced to the  $m$ -mode analysis maps by the three terrestrial sources shown in Figure 3.17. Because these sources are not moving through the sky sidereally, they tend to be smeared along rings of constant declination. The spurs seemingly radiating from the NCP are a Moiré pattern (i.e., an artifact of the pixelization). . . . . 83
- 4.1 A flow chart describing the data analysis steps performed in this paper. Radio waves are received by antennas (depicted in the upper-left corner), which are correlated to produce raw visibilities. These visibilities are then flagged, calibrated, and bright point sources are removed. After a full sidereal day's worth of data has been collected, these visibilities can be Fourier transformed to compute the measured  $m$ -modes. Separately, an empirical beam model is used to calculate the transfer matrix elements that describe the interferometer's sensitivity to the sky. Full covariance matrices are computed for the foreground emission, 21 cm signal, and thermal noise. These matrices are used to compress, filter foreground emission, and whiten the noise covariance. Finally, the resulting filtered  $m$ -modes are used to estimate the spatial power spectrum of 21 cm emission. Images of the sky can be constructed through the use of Tikhonov-regularized imaging (Eastwood et al., 2018), which are useful for diagnosing errors in the analysis. . . . . 92
- 4.2 A Molleweide projection of a Tikhonov-regularized image of the sky constructed from all baselines representable with  $l_{\max} \leq 200$ , and 2.6 MHz of bandwidth centered on 73.2 MHz. The color scale is linear between  $-1000$  K and  $+1000$  K, and logarithmic outside of this range. No cleaning has been performed, so all point sources are convolved with a point spread function, and no masking of low declinations has been performed. The resolution of the maps naturally degrades at low declinations and the regularization scheme naturally encourages the map to be zero below the horizon. Negative rings at the declination of bright point sources are an artifact of the fact that  $m = 0$  modes are filtered from the dataset due to their susceptibility to RFI and common-mode pickup. (top) Before bright point sources are removed from the dataset. (bottom) After point source removal. . 96

4.3 The system temperature $T_{\text{sys}}$ (scaled by the antenna efficiency $\eta$ ) measured as a function of frequency (left panel, solid black line), and local sidereal time (right panel, solid black line). The hatched region denotes the range of sky temperatures measured by the LEDA experiment (Price et al., 2018). The shaded region denotes the range of sky temperatures measured by the EDGES experiment in the southern hemisphere (Mozdzen et al., 2017). . . . .	99
4.4 The angular power spectrum of the sky as measured by the OVRO-LWA at 73.260 MHz. Measurements (with 95% uncertainty) are indicated with red bars. The uncertainty is dominated by sample variance. The dashed black line is the best-fit power-law spectrum, and the solid black line is the best-fit solution when the power-law index is allowed to run. The dash-dot line is a model derived, in part, from the Haslam 408 MHz sky map (Haslam et al., 1981, 1982; Santos et al., 2005). The feature at $l \sim 30$ is sensitive to the choice of covariance matrix, and is therefore likely instrumental. . . . .	100
4.5 The relative error involved with making the flat-sky approximation for a hat function power spectrum (i.e., the relative difference between Equations 4.19 and 4.20) with $l = 10$ (solid line) and $l = 100$ (dashed line). The hat function is centered at $k_{\parallel} = 0.1 \text{ Mpc}^{-1}$ with a domain that extends from $0.095 \text{ Mpc}^{-1}$ to $0.105 \text{ Mpc}^{-1}$ . The spikes in relative error correspond to when $C_l^{\text{curved}}(\Delta\nu) \approx 0$ . . . . .	104
4.6 Illustration of the action of foreground filtering on each of the covariance matrices discussed in §4.4. The left column corresponds to the noise covariance matrix, the middle column corresponds to the high-redshift 21 cm contribution to the covariance, and the right column corresponds to the foreground covariance matrix. The top row is before any filtering has been applied, the middle row is after the first KL transform, and the bottom row is after the second KL transform. . . . .	106
4.7 The fractional increase in the size of the error bars in each power spectrum bin due to the application of a double KL transform foreground filter (moderate strength). . . . .	107

4.8 Mollweide projected illustration of the sky where shaded regions are down-weighted by the foreground filter. From darkest to lightest, these regions of the sky are filtered by the mild, moderate, and extreme foreground filters respectively. . . . .	108
4.9 (top) Mollweide projected image of the sky after point source removal and moderate foreground filtering. The dominant residual feature in the residuals is associated with the Sun. (bottom) The power spectrum estimated without point source removal (left) and with point source removal (right) at a range of filter strengths. Points correspond to the estimated power spectrum amplitude and the dashed lines correspond to the computed thermal noise. Mild foreground filtering is red, moderate foreground filtering is black, and extreme foreground filtering is blue. . . . .	112
4.10 (top) Mollweide projection of the sky in galactic coordinates after differencing even and odd-numbered integrations. The Sun is the dominant artifact in this image due to the sporadic failure of source subtraction. Large residuals are also present at low declinations that do not rise above $10^\circ$ elevation. These low-elevation artifacts are generated by RFI. (bottom) The power spectrum estimated without point source removal (left) and with point source removal (right). Point correspond to the estimated power spectrum amplitude and the dashed line corresponds to the computed thermal noise. Red and blue points are estimates from the even and odd numbered integrations respectively. Black points are estimates after computing the difference between the two halves of data. . . . .	114
4.11 (top) Orthographic projection of the sky constructed from data collected only during the day (left), and only during the night (right). (bottom) The power spectrum estimated without point source removal (left) and with point source removal (right). Points correspond to the estimated power spectrum amplitude and the dashed line corresponds to the computed thermal noise. Measurements from the day are red, and measurements from the night are blue. . . . .	116

4.12 (top) Mollweide projection of the sky in galactic coordinates after differencing the $xx$ and $yy$ correlations. Note that this is not true linear polarization because it does not account for the full polarization of the antenna response pattern. (bottom) The power spectrum estimated without point source removal (left) and with point source removal (right). Point correspond to the estimated power spectrum amplitude and the dashed line corresponds to the computed thermal noise. Red and blue points are estimates from the $xx$ and $yy$ correlations respectively. Black points are estimates from the mean of the $xx$ and $yy$ correlations. . . . .	118
4.13 (top) Mollweide projection of the sky in galactic coordinates after differencing two adjacent 240 kHz frequency channels. (bottom) Simulated power spectrum estimates as a result of a foreground model and gain errors that are incoherent between antennas (left) and coherent between antennas (right). Blue corresponds to 0.1% errors, black corresponds to 1% errors, and red corresponds to 10% errors in the complex gains. . . . .	119
.14 A comparison of two approximations (thin black lines) to the spherical Bessel function $j_l(x)$ with $l = 100$ (thick gray lines). The top panel shows the approximation derived from the limiting behavior of $j_l(x)$ as $x \rightarrow \infty$ . This is a poor approximation near $x \sim l$ . The bottom panel shows the approximation derived from the method of steepest descent. This approximation maintains the same limiting behavior as $x \rightarrow \infty$ and greatly improves the accuracy of the approximation near $x \sim l$ . . . . .	124

## LIST OF TABLES

<i>Number</i>	<i>Page</i>
3.1 A summary of the generated all-sky maps. . . . .	61

## *Chapter 1*

# INTRODUCTION

### 1.1 Fundamental Physics

The discovery of the cosmic microwave background (CMB) radiation by Penzias & Wilson (1965) provided the first direct evidence that the universe had a beginning. Arno Penzias and Robert Wilson shared the 1978 Nobel Prize in Physics for this discovery, and astronomers have been studying this relic of the Big Bang ever since. In fact, a second Nobel Prize was awarded to John Mather and George Smoot in 2006 for their work on the Cosmic Background Explorer (COBE) satellite, which was amongst the first experiments to demonstrate that the background radiation was anisotropic (Smoot et al., 1992). These studies of the CMB have fundamentally advanced humanity’s understanding of the universe: its origin, evolution, and composition. We continue to study the CMB today in part because it illuminates everything in the universe. It is a flashlight for the darkness of space within our expanding universe.

As the universe expands, the wavelength of a photon is similarly stretched or redshifted (so-called because it gradually drifts to longer, redder wavelengths). Photons originating from a star 1000 light-year away will travel through the universe for 1000 years before they are collected by our telescopes. Consequently, we observe this star as it was 1000 years ago. However, the photon was also stretched by a small factor of 0.000007% during its travels due to the expansion of the universe. For nearby stars, this expansion is too small to be conceivably measured. However, with the discovery of the first quasar by Schmidt (1963) it soon became apparent that the stretching factor, the redshift  $z$ , can be  $> 10\%$ . Today, the most distant known quasars and galaxies are so far away that the wavelength has more than doubled ( $z > 1$ ) due to the expansion of the universe (e.g., Mortlock et al., 2011; Zitrin et al., 2015; Oesch et al., 2016; Bañados et al., 2018).

Due largely to careful and detailed work studying the CMB (e.g., Hinshaw et al., 2013; Planck Collaboration et al., 2016a), Type Ia supernova explosions (e.g., Riess et al., 1998; Perlmutter et al., 1999), and cosmological galaxy surveys (e.g., Colless et al., 2001), we have a coherent and consistent understanding of the expansion history of the universe. The redshift  $z$  is therefore commonly used as a proxy for

distance. The higher the redshift, the longer the photon has been in transit, and the further its origin. However, in order to measure the redshift, the detected photon must originate from a known spectral feature.

Despite its abundance, neutral hydrogen (H I) has few low energy transitions that allow it to be traced. Due to this limitation, astronomers resort to using a hyperfine structure transition arising from the magnetic dipole interaction between proton and electron. This interaction leads to a slight energy difference between the spin-symmetric state and the spin-antisymmetric state. The energy difference is  $hc/(21 \text{ cm})$  where  $h$  is Planck's constant, and  $c$  is the speed of light. When a hydrogen atom transitions from the spin-symmetric state (higher energy;  $F = 1$ ) to the spin-antisymmetric state (lower energy;  $F = 0$ ), it emits a photon with a wavelength of 21 cm or a frequency of 1420 MHz. The redshift  $z$  of a 21 cm photon is therefore computed from the observed frequency  $\nu$  as

$$z = \frac{1420 \text{ MHz}}{\nu} - 1. \quad (1.1)$$

The 21 cm transition is exceptionally weak. The half-life of a neutral hydrogen atom in the  $F = 1$  state is over 10 Myr. However, the early universe following recombination is almost entirely composed of neutral hydrogen.

When H I is illuminated by the CMB, a portion of the incident photons are 21 cm photons. These photons can be absorbed by a hydrogen atom in the  $F = 0$  state, or stimulate the emission of 21 cm photon from a hydrogen atom in the  $F = 1$  state. A careful calculation of the radiative transfer for a clump of atomic hydrogen gas illuminated by the CMB at the redshift  $z$  yields (Pritchard & Loeb, 2012, but neglecting the contribution of peculiar velocities)

$$\Delta T_{21} \approx 27 \left[ \overbrace{x_{\text{HI}}(1 + \delta) \left( \frac{\Omega_b h}{0.0327} \right) \left( \frac{\Omega_m}{0.307} \right)^{-1/2} \left( \frac{1+z}{10} \right)^{1/2}}^{\text{quantity of HI}} \overbrace{\left( \frac{T_{\text{spin}} - T_{\text{CMB}}(z)}{T_{\text{spin}}} \right)}^{\text{relative temperature}} \right] \text{mK}, \quad (1.2)$$

where  $\Delta T_{21}$  is the expected 21 cm brightness temperature. If  $\Delta T_{21} > 0$ , the 21 cm transition appears in emission against the CMB. If  $\Delta T_{21} < 0$ , it appears in absorption.  $x_{\text{HI}}$  is the neutral fraction of hydrogen,  $\delta$  is the local baryon overdensity,  $h$  is the Hubble constant,  $\Omega_b$  is the density parameter for baryons,  $\Omega_m$  is the density parameter for matter,  $T_{\text{spin}}$  is the spin temperature (the excitation temperature of the 21 cm transition), and  $T_{\text{CMB}}(z) = 2.73(1+z)$  K is the temperature of the CMB at the redshift  $z$ .

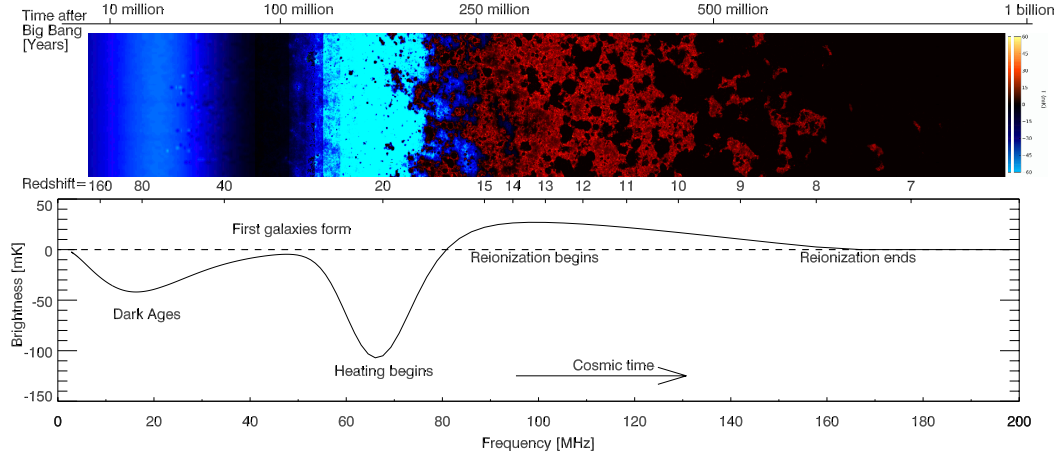


Figure 1.1: (top) A simulated light cone of the 21 cm brightness temperature illustrating the anisotropy in the expected signal. (bottom) A simulation of the globally averaged brightness temperature due to the high redshift 21 cm transition. This figure is reproduced with permission from Pritchard & Loeb (2012).

Equation 1.2 is fundamental to determining what can be learned through detecting the 21 cm transition at high redshift. First, the 21 cm transition of neutral hydrogen at  $z \sim 10$  can perturb the 2.73 K thermal CMB spectrum by typically 10–100 mK. Second, If the spin temperature is greater than the CMB temperature, the 21 cm transition appears in emission. However, the signal saturates at high spin temperatures. If the spin temperature is less than the CMB temperature, the 21 cm transition appears in absorption with no saturation point. There is no measurable 21 cm signal if the transition is in radiative equilibrium with the CMB. Finally, the amplitude of the signal is proportional to the total quantity of H I. Therefore, the amplitude tends to be larger while the universe is predominantly neutral. Because redshift can be computed from the observed frequency (Equation 1.1), the highly redshifted 21 cm transition can be used to map the three dimensional structure of the universe and chronicle its history through the Cosmic Dawn and Epoch of Reionization (EoR). A fiducial prediction for  $\Delta T_{21}(z)$  can be seen in Figure 1.1.

## 1.2 A History of the Universe through the 21 cm Transition

There are three relevant temperatures that affect the spin temperature:  $T_{\text{gas}}$ , the temperature of the gas,  $T_{\text{CMB}}$ , the temperature of the CMB, and  $T_{\text{Ly}\alpha}$ , the color temperature of the Ly $\alpha$  radiation from early star formation. More exotic theories might also include the temperature of the dark matter,  $T_{\text{DM}}$ . Generally, Ly $\alpha$  photons scatter through the intergalactic medium (IGM), which sets  $T_{\text{Ly}\alpha} = T_{\text{gas}}$ . In the

absence of any heating mechanisms, the matter and radiation are both cooling adiabatically with the expansion of the universe. The adiabatic indices are  $\gamma = 5/3$  and  $\gamma = 4/3$  respectively, so the matter cools faster than the radiation. Consequently, the 21 cm transition tends to appear in absorption prior to early star formation, and in emission after the IGM has been heated.

While there are currently few observational constraints on the 21 cm brightness temperature, fiducial theoretical models tell the following story (e.g., Furlanetto et al., 2006; Pritchard & Loeb, 2012). Prior to star formation—the dark ages ( $z \gtrsim 40$ )—the density of the universe is high enough for collisions between hydrogen atoms to dominate the excitation of the 21 cm transition. During this time  $T_{\text{spin}} = T_{\text{gas}}$ , and the 21 cm transition appears in absorption against the CMB. Later ( $z \sim 30$ ), as the mean density of the universe decreases, collisions become more infrequent and the 21 cm transition is instead excited by CMB photons. During this time the 21 cm signal vanishes because  $T_{\text{spin}} = T_{\text{CMB}}$ .

With the onset of star formation in the universe, the Cosmic Dawn, the IGM is inundated with Ly $\alpha$  photons. These Ly $\alpha$  photons scatter through the IGM. With the absorption and re-emission of a Ly $\alpha$  photon, a hydrogen atom can transition between the spin-symmetric state and the spin-antisymmetric state. This process, called the Wouthuysen-Field effect, sets the relative abundance of H I in each state such that  $T_{\text{spin}} = T_{\text{Ly}\alpha} = T_{\text{gas}}$  (Wouthuysen, 1952; Field, 1958). Therefore, after early star formation begins, the 21 cm transition reappears in absorption against the CMB.

However, as star formation progresses, the gas in the IGM is heated. X-rays are particularly effective at heating the IGM due to their large mean-free path. Consequently the heating rate is sensitive to, for example, the number density, luminosity and spectral hardness of X-ray binaries (Fialkov et al., 2014; Greig & Mesinger, 2017). Eventually the gas is heated above the temperature of the CMB, bringing the 21 cm transition into emission, and eventually the signal saturates. At this point the 21 cm transition begins to disappear with the onset of reionization at  $z \lesssim 15$  due to the ionization of the IGM. A prediction of the spectral distortion this process applies to the low-frequency ( $\nu < 200$  MHz) CMB spectrum can be seen in the bottom panel of Figure 1.1.

Due to the extremely wide fields of view of low-frequency radio telescopes, the use of the 21 cm transition is unique in its ability to directly probe the temperature, density, and ionization state of the IGM over extremely large volumes. However,

the EoR is also the focus of a number of other complementary studies that inform this prediction. Careful observations of the CMB constrain the mean redshift of reionization through the Thomson scattering optical depth, and the duration of reionization through the kinetic Sunyaev–Zel’dovich (kSZ) effect. The final nine-year results from the Wilkinson Microwave Anisotropy Probe (WMAP) favored a mean reionization redshift of  $z \sim 10$  (Hinshaw et al., 2013). More recently, the Planck experiment measured a lower optical depth that prefers a reionization history with a mean at  $z \sim 7.8 - 8.8$  and a duration of  $\Delta z < 2.8$  (Planck Collaboration et al., 2016b), which is easier to reconcile with the measured ultraviolet (UV) luminosity functions of high-redshift galaxies.

The discovery of ever-distant high-redshift galaxies has begun to constrain the ultraviolet luminosity function during the EoR. These galaxies are typically discovered by searching for the Lyman break in deep galaxy surveys (pioneered by Steidel et al., 1996). The most distant spectroscopically confirmed galaxy is GN-z11 at  $z \approx 11.1$  (Oesch et al., 2016). An image of this galaxy can be seen in Figure 1.2. The UV luminosity function constrains the number of ionizing photons generated by these high-redshift galaxies, however flux-limited galaxy surveys necessarily only discover the most exceptionally luminous galaxies. In contrast, measuring the 21 cm brightness temperature will constrain the integrated UV luminosity function. Current limits (including a “reasonable” extrapolation to unseen fainter galaxies) suggest that high-redshift star-forming galaxies produce enough photons to ionize the universe on a timescale consistent with constraints from the CMB (Robertson et al., 2015).

The timing of reionization has also been constrained by the discovery of high-redshift quasars, which can be used to map the Ly $\alpha$  opacity—and hence the neutral fraction of hydrogen—along the line of sight. Variations between lines of sight additionally provides evidence for the patchiness of reionization (see Figure 1.3). The highest redshift quasars at  $z > 7$ , however, are exceptionally rare. Mortlock et al. (2011) discovered a quasar at  $z \approx 7.1$ , and by measuring the damping wing of the near-zone Ly $\alpha$  absorption determined that the neutral fraction is at least 0.1 in the vicinity of this quasar. Bañados et al. (2018) found another quasar at  $z \approx 7.5$  and performed a similar analysis to determine that the neutral fraction is at least 0.33. The EoR therefore appears to be in progress and drawing to a close by  $z \sim 6$ .

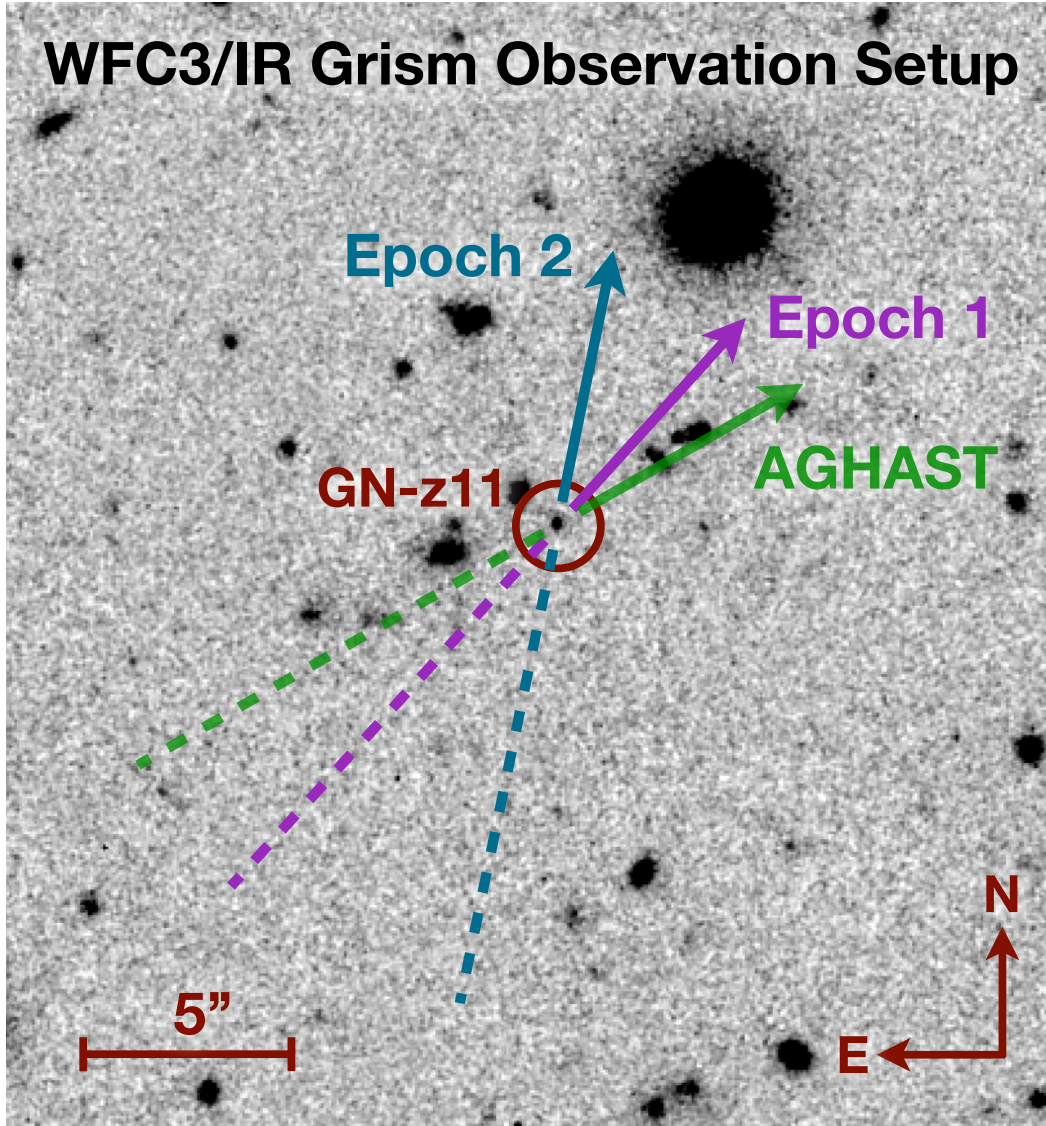


Figure 1.2: An  $H$ -band image of GN-z11, the most distant spectroscopically confirmed galaxy with the dispersion direction for the Hubble Space Telescope grism spectra that confirmed that this galaxy originates from  $z \approx 11.1$ . This figure is reproduced from Oesch et al. (2016). [get permission to republish this figure](#)

### 1.3 First Generation 21 cm Experiments

The first successful attempt make use of the 21 cm emission to map the three-dimensional structure of the universe was conducted by Chang et al. (2010) using the Green Bank Telescope (GBT) across redshifts 0.53–1.12. This measurement demonstrated the feasibility of using low-resolution spectral-line maps to study Baryon Acoustic Oscillations (BAO) at the onset of the accelerating expansion of the universe.

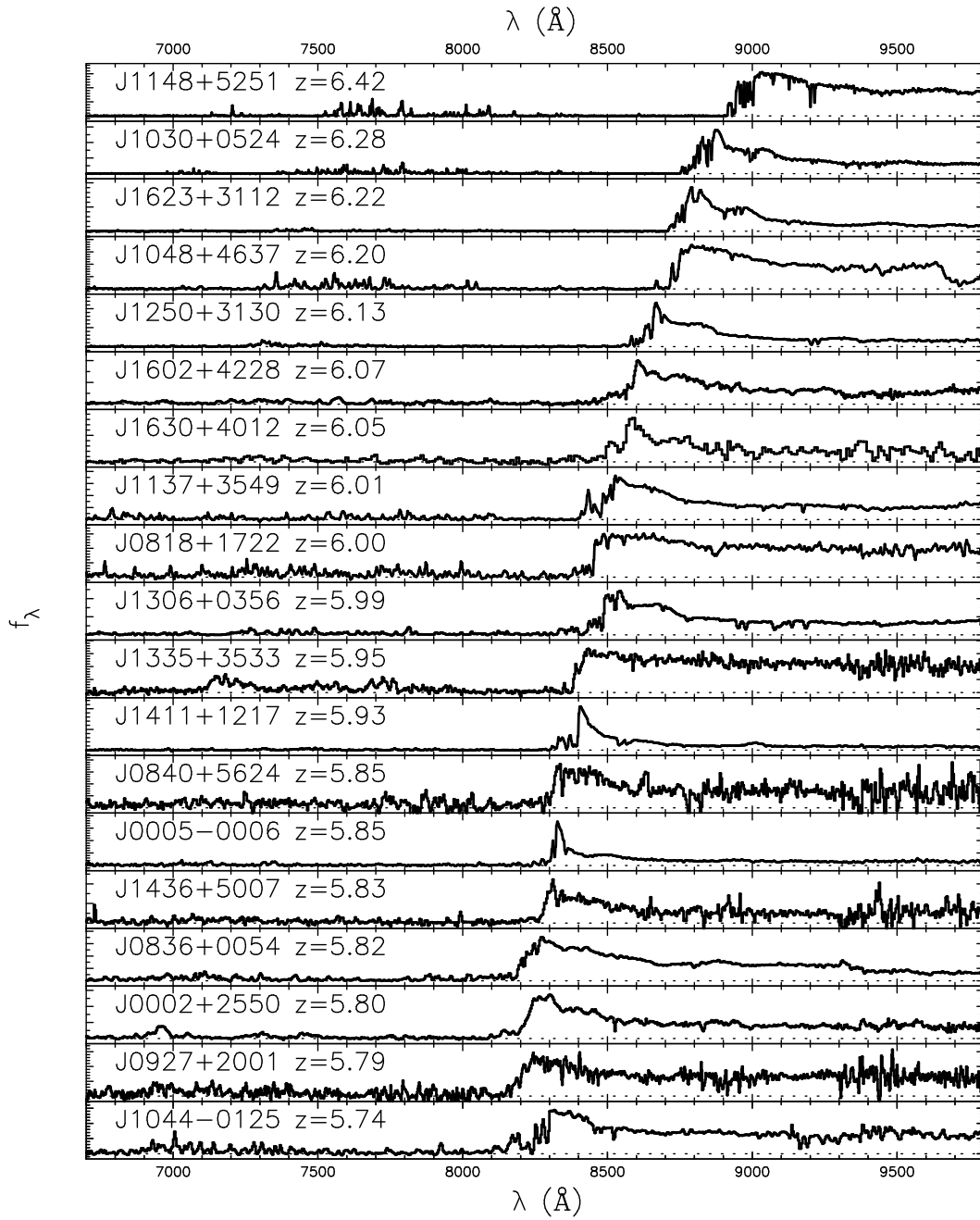


Figure 1.3: A collection of spectra for high-redshift quasars illustrating the trend towards a completely saturated Gunn–Peterson trough with increasing redshift, but variations between quasars at comparable redshifts provide evidence for patchy reionization. This figure is reproduced from Fan et al. (2006). **get permission to republish this figure**

Ultimately, it may be possible to map the EoR and Cosmic Dawn through the 21 cm line (Madau et al., 1997). In fact, this is called a “main science goal” for the future Square Kilometer Array (SKA; Mellema et al., 2013). First generation experiments, however, are of somewhat more limited scope and therefore employ statistical averages to boost sensitivity to the high-redshift 21 cm signal.

The two most popular statistics are the global average and the power spectrum. The global average—or monopole—is computed by averaging over all lines of sight. The global signal is therefore simply the mean 21 cm brightness temperature within a spherical shell of the universe:

$$T_{21}^{\text{global}}(z) = \frac{1}{\Omega} \int \Delta T_{21}(z; \hat{r}) d\Omega, \quad (1.3)$$

where  $T_{21}^{\text{global}}(z)$  is the global 21 cm signal at the redshift  $z$ ,  $\Delta T_{21}(z; \hat{r})$  is the 21 cm brightness temperature at the redshift  $z$  in the direction  $\hat{r}$ , and the integral runs over solid angle  $\Omega$ .

The power spectrum statistic leverages the line of sight distance information from the observed frequency to measure the power in fluctuations on a given spatial scale within a volume of the universe:

$$P_{21}(z; \vec{k}) = \frac{1}{V} \left| \int \Delta T_{21}(\vec{r}) e^{-i\vec{k}\cdot\vec{r}} d^3 r \right|^2, \quad (1.4)$$

where  $P_{21}(z; \vec{k})$  is the three-dimensional spatial power spectrum at the redshift  $z$  and wavevector  $\vec{k}$ , and the integral runs over the observed volume  $V$  of the universe. Neglecting redshift-space distortions, the spatial power spectrum of 21 cm fluctuations is expected to be isotropic. Therefore, typically the power spectrum  $P(\vec{k})$  is averaged over the orientation of the wavevector  $\vec{k}$ . Instrumental considerations typically lead to different sources of systematic errors along the line of sight and perpendicular to the line of sight, so parameterizing the power spectrum in terms of the parallel and perpendicular to the line of sight wavenumbers ( $k_{\parallel}$  and  $k_{\perp}$  respectively) is common.

The global signal and the power spectrum are both statistics of the same underlying 21 cm brightness temperature and therefore both statistics can be used to answer high-level questions such as: When did reionization occur? How quickly was the universe heated after initial star formation began? The power spectrum contains additional information about the sources of heating and ionization. During the Cosmic Dawn, a detection of the 21 cm power spectrum could constrain the X-ray

emissivity and spectral hardness (Fialkov et al., 2014) the strength of Lyman–Werner feedback (Fialkov et al., 2013), and the spatial scale on which this X-ray emission originates. During the EoR, a detection of the 21 cm power spectrum could constrain the ionizing efficiency of early galaxies, the mean-free path of ionizing photons, and the minimum halo mass for star formation (Greig & Mesinger, 2015). However, both approaches are complementary because they employ substantially different instrumental designs and are subject to different (but not exclusively different) systematic errors.

### Global Signal Experiments

Most global signal experiments are composed of a single dipole antenna with a total power radiometer. This approach was pioneered by the Experiment to Detect the Global EoR Signature (EDGES). After deploying to the Murchison Radio-astronomy Observatory (MRO) in a remote region of Western Australia, Bowman & Rogers (2010) observed for three months. If reionization was an instantaneous event, this initial EDGES deployment would have expected to see a step function in their sky-averaged spectrum. Therefore the authors converted the observed spectral smoothness to a lower bound on the duration of reionization  $\Delta z > 0.06$ . However, because no such feature was detected, the redshift of reionization was not constrained by this measurement.

EDGES has continued to improve on this initial constraint. Monsalve et al. (2017) reported results from the updated EDGES high-band instrument (90–190 MHz), which now rules out most reionization histories with  $\Delta z \lesssim 0.4$  and histories with  $\Delta z \lesssim 1.0$  if the central redshift of reionization is near  $z \approx 8.5$ . Even more recently, Bowman et al. (2018) reported results from the new EDGES low-band instrument (50–100 MHz), which is effectively a scaled copy of the high-band instrument. The latter results will be discussed in more detail in §1.5.

The Large-aperture Experiment to Detect the Dark Age (LEDA; Price et al., 2018) similarly equips low-frequency (30–85 MHz) dipole antennas with radiometers. Located at the Owens Valley Radio Observatory (OVRO) near Big Pine, California, these antennas are embedded within the OVRO-LWA. This configuration provides LEDA with additional leverage for self-calibration and foreground imaging, which may prove crucial for overcoming latent concerns about beam modeling and foreground removal in many global signal experiments.

The SARAS 2 experiment, like EDGES, is a single antenna radiometer. However,

SARAS 2 has chosen an unconventional sphere-disk monopole antenna in order to minimize the frequency structure in the antenna response pattern. Singh et al. (2017) reported initial results from a 63 hr integration over the frequency range 110–200 MHz from the Timbaktu Collective in Southern India. By comparing against parameterized models of the 21 cm signal, the authors concluded that their initial results generally rule out models with weak X-ray heating and rapid reionization. These models generally produce sharp spectral features in the observing band, and so this limit arises from the measured spectral smoothness.

Although most global signal experiments are composed of isolated dipole antennas, there have been several attempts to design and use more exotic instruments. Liu et al. (2013) found that an instrument with a 5° beam could achieve a higher significance detection by using the improved angular resolution to mitigate foreground contamination. Vedantham et al. (2015) used lunar occultation to constrain the global signal between 35 and 80 MHz using LOFAR. This technique uses an interferometer to measure the contrast between the moon and the surrounding sky, but is complicated by radio frequency interference (RFI) reflecting off of the moon and potentially by the assumption that the moon is a thermal source at low frequencies. Drawn by the calibration advantages of interferometers, other groups have proposed designing interferometers that have nonzero sensitivity to the monopole. Presley et al. (2015) developed a framework for measuring the global signal from interferometric measurements, and Singh et al. (2015) designed a zero-spacing interferometer using a resistive screen to separate two antennas. However, ultimately the calibration advantages of using an interferometer to measure the global signal may have been overstated. Venumadhav et al. (2016) demonstrated that interferometers may only have any sensitivity to the global signal if there is some amount of cross talk between the correlated elements or a source of noise that can radiate coherently into both receivers.

### **Power Spectrum Experiments**

In contrast to the global signal experiments, which are typically composed of a single antenna, power spectrum experiments are generally interferometers composed of up to hundreds or thousands of antennas. A high-level overview of existing upper limits on the 21 cm power spectrum can be seen in Figure 1.4.

The Donald C. Backer Precision Array for Probing the Epoch of Reionization (PAPER; Parsons et al., 2010) began attempting to measure the 21 cm power spectrum

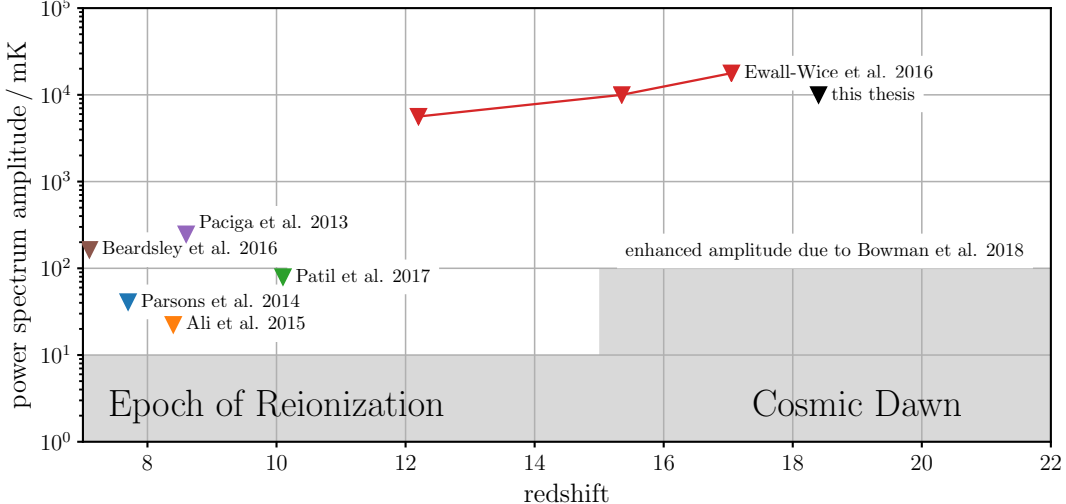


Figure 1.4: Power spectrum amplitude upper limits (95% confidence or lowest systematically limited data point) as a function of redshift. The shaded region denotes roughly where current theoretical predictions fall.

with a deployment of eight antennas in Green Bank, West Virginia. Later deployed with 32 antennas to the Karoo desert in South Africa, Parsons et al. (2014) measured a  $2\sigma$  upper limit of  $(41 \text{ mK})^2$  on the amplitude of the power spectrum at  $z = 7.7$ . This measurement ruled out the possibility that the universe was entirely unheated by this redshift. Later, with PAPER now composed of 64 antennas, Ali et al. (2015) improved the best  $2\sigma$  upper limit to  $(22.4 \text{ mK})^2$  at  $z = 8.4$ , however this result is currently subject to revision due to a number of errors including unexpected signal loss and underestimated error bars (Cheng et al. in prep.). PAPER is notable for its decision to part with traditional interferometry. Starting with its 32-antenna deployment, PAPER opted for a maximally redundant antenna configuration, which maximizes the interferometer’s raw sensitivity to a particular spatial scale.

The Low-Frequency Array (LOFAR) EoR Key Science Project (KSP) is attempting a similar measurement of the 21 cm power spectrum. In contrast to PAPER, LOFAR is composed of  $\sim 30,000$  high-band antennas (120–240 MHz) and  $\sim 3,000$  low-band antennas (30–80 MHz). These antennas are grouped into stations and stations are correlated with each other. This design is a trade off that sacrifices field of view for gain. The LOFAR EoR KSP recently published its first limits on the 21 cm power spectrum, finding a  $2\sigma$  upper limit of  $(79.6 \text{ mK})^2$  at  $z = 10.1$  (Patil et al., 2017). In this measurement, LOFAR attempted to leverage its superior imaging and source-removal capabilities, but ultimately this measurement was limited by residual systematic errors. The removal of contaminating diffuse radio emission has

been the focus of ongoing work with some reported success (Koopmans, 2017).

Several attempts have been made to measure the 21 cm power spectrum with the Murchison Widefield Array (MWA) using multiple different techniques (Jacobs et al., 2016). Beardsley et al. (2016) reported results from the first season of observing, and placed an upper limit of  $(164 \text{ mK})^2$  at  $z = 7.1$  with a 32 hr integration. While all previous power spectrum measurements had attempted to constrain the power spectrum of 21 cm fluctuations during the EoR, Ewall-Wice et al. (2016) used the MWA to place upper limits on the 21 cm power spectrum during the Cosmic Dawn. In their highest redshift measurement, the authors placed a limit of  $\sim (18,000 \text{ mK})^2$  at  $z \sim 17$ . A simple comparison between these two upper limits from the MWA illustrates the difficulty involved with constraining the Cosmic Dawn at a higher redshift than the EoR.

Finally, the Giant Metrewave Radio Telescope (GMRT) EoR experiment, located near Pune, India, first reported a  $2\sigma$  upper limit of  $(70 \text{ mK})^2$  at  $z \approx 8.6$  (Paciga et al., 2011). However, this limit was later revised to  $(248 \text{ mK})^2$  after a careful study of the signal loss associated with foreground removal (Paciga et al., 2013).

#### **1.4 Observational Challenges**

The two most substantial challenges faced by all attempts to measure the cosmological 21 cm emission are:

1. the blindingly bright foreground radio emission that must be subtracted, removed, or otherwise suppressed, and
2. the instrumental calibration, which must be completed with a high degree of accuracy or else residual foreground emission could be confused with the cosmological 21 cm signal.

#### **Foreground Emission**

Prior to the commencement of this thesis, the most commonly used model of the low-frequency sky was the Global Sky Model (GSM; de Oliveira-Costa et al., 2008). The GSM is effectively an interpolation of previously published sky maps between 10 MHz and 100 GHz. However, the majority of the modern, high fidelity sky maps are located at frequencies above 1.4 GHz. Below 1.4 GHz, there is the 408 MHz Haslam map (Haslam et al., 1981, 1982), which covers the sky at  $1^\circ$  resolution. At 45 MHz, Guzmán et al. (2011) compiled a sky map from a northern hemisphere

survey and a southern hemisphere survey each at  $5^\circ$  resolution (Alvarez et al., 1997; Maeda et al., 1999). At 22 MHz, Roger et al. (1999) mapped the sky from the Canadian Dominion Radio Astrophysical Observatory (DRAO) at  $1^\circ$ – $2^\circ$  resolution.

At large angular scales  $\theta \gg 1^\circ$ , the low-frequency radio sky is dominated by galactic synchrotron emission generated by relativistic electrons spiraling around galactic magnetic field lines. The EDGES experiment, in the southern hemisphere, measured the brightness temperature of this emission at *high* galactic latitudes to be (Mozdzen et al., 2017)

$$T \sim 300 \left( \frac{\nu}{150 \text{ MHz}} \right)^{-2.6} \text{ K.} \quad (1.5)$$

At smaller angular scales  $\theta \ll 1^\circ$ , the galactic emission gives way to a sea of active galactic nuclei (AGN), the brightest of which—Cyg A—has a flux  $> 15,000 \text{ Jy}$  at frequencies  $< 80 \text{ MHz}$  (Baars et al., 1977). A simple comparison between Equations 1.2 and 1.5 reveals that the foreground radio emission must be suppressed by four to five orders of magnitude before the 21 cm fluctuations can be detected. However, this foreground emission is typically synchrotron and free-free, both of which generate smooth power-law spectra. The 21 cm signal, on the other hand, is not expected to be so smooth. This is due to the fact that sweeping through frequency along a line of sight probes different causally disconnected regions of the universe. Each of these regions experiences a different star formation, heating and reionization history, which ultimately produces a different 21 cm brightness temperature. While spectral structure can be used to separate the signal from contaminating foreground emission, there is still a relative paucity of suitable modern, high-fidelity sky maps at frequencies  $< 200 \text{ MHz}$ .

Compounding the problem, global signal experiments have no intrinsic angular resolution of their own. To date, these experiments have typically relied on low-order polynomial fits to remove the foreground contamination in their measurements. This is a fine balancing routine, because if the polynomial order is chosen to be too low, residual foreground contamination dominates the measurement. If the polynomial order is chosen to be too high, the 21 cm signal itself can be removed. Similarly, some power spectrum experiments, notably PAPER, have opted for a maximally redundant baseline configuration that greatly inhibits the interferometer’s ability to image the sky with high fidelity. Consequently there is a growing demand for modern, high-fidelity sky maps at these frequencies.

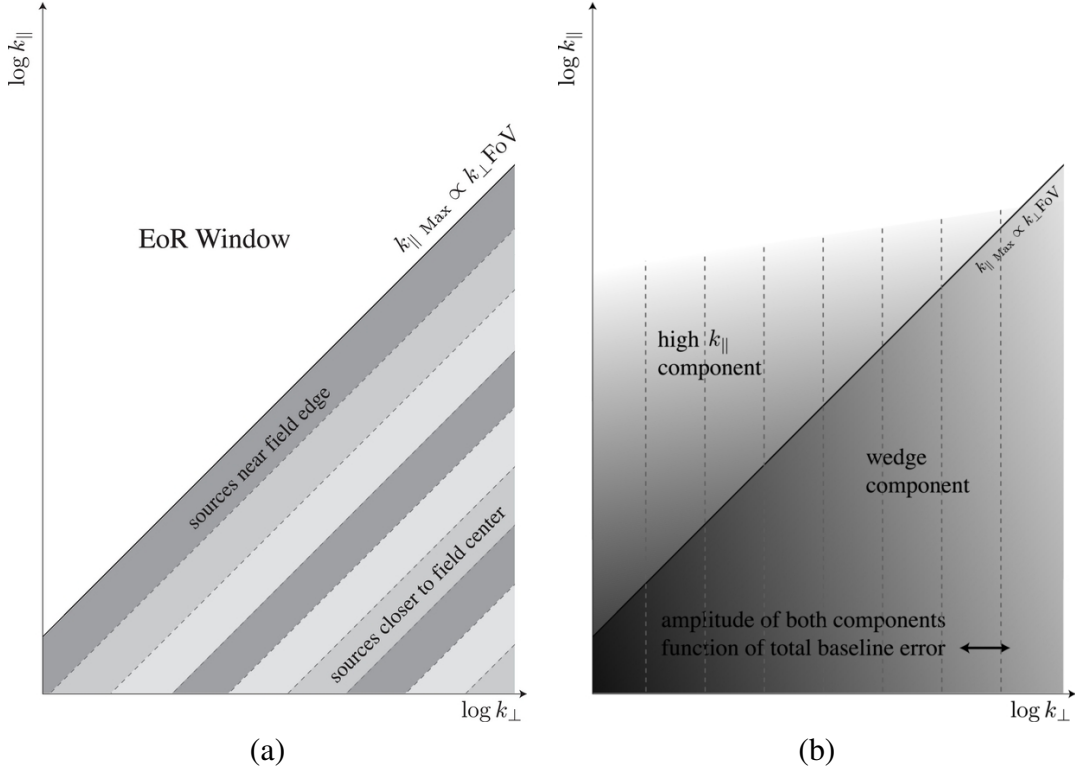


Figure 1.5: (a) Illustration of the foreground wedge. The emission near the edge of the foreground wedge typically originates from sources located far from the delay center. (b) Illustration of the contamination arising after calibration errors. Emission leaks out of the foreground wedge and into the otherwise clean “EoR Window.” Reproduced from Morales et al. (2012) (permission not yet received).

## Foreground Avoidance

In the absence of a reliable foreground model, some power spectrum experiments—notably PAPER—have opted for a delay-spectrum technique to separate foreground emission from the cosmological 21 cm signal (Parsons et al., 2012). This technique has also been coined “foreground avoidance,” because it applies a transformation to the dataset that—under ideal circumstances—restricts the extent of foreground contamination to a wedge-like feature in power spectrum space (see Figure 1.5 for an illustration). The existence of the foreground wedge can be seen with a simple argument presented below.

In the flat-sky approximation, an interferometer measures a visibility  $V_\nu^{ij}$  between the pair of antennas  $i$  and  $j$  at the frequency  $\nu$ . For isotropic antennas, the visibility is related to the sky brightness  $I_\nu(l, m)$  through

$$V_v^{ij} = \int I_\nu(l, m) \exp\left(2\pi i(u l + v m)\right) dl dm, \quad (1.6)$$

where  $l$  and  $m$  are direction cosines, and  $u$  and  $v$  are the east–west and north–south components of the baseline vector measured in units of wavelengths. Equation 1.6 is a Fourier transform over the plane of the sky, and so in order to construct a three-dimensional power spectrum, an additional Fourier transform along the line of sight is needed. This can be accomplished by expanding the comoving distance with the Taylor expansion  $r \approx r_0 + (\partial r / \partial v)(v - v_0)$  at the appropriate redshift. Under this approximation, a Fourier transform along the line of sight is a Fourier transform over frequency. The Fourier dual variable to the frequency is delay. That is, by taking a Fourier transform along the line of sight, we are actually undoing the F stage of the correlator, and computing a series of correlations at a range of time delays. Consequently, the perpendicular wavenumber  $k_{\perp} \propto$  the baseline length, and the parallel wavenumber  $k_{\parallel} \propto$  delay.

For a smooth spectrum radio source, the maximum possible delay between the two antennas  $i$  and  $j$  is the light-travel time between the two antennas. More generally the delay is given by the path difference, and sources located far from the delay center have larger delays. The pattern of contamination for smooth spectrum radio sources is therefore generally restricted to a wedge-like structure that is illustrated in the left panel of Figure 1.5. With the foreground emission contained within this wedge, the power spectrum may simply be estimated from the set of modes outside of the wedge, and in this way avoid the contamination of the foreground emission.

The technique of foreground avoidance is predicated on the assumption that the spectral structure of the foreground emission is smooth enough for it to be contained within the foreground wedge. Instrumental chromaticity and polarization leakage are of particular concern. Faraday-rotated linearly polarized emission, for instance, is not contained within the foreground wedge. Furthermore, widefield effects such as baseline foreshortening towards the horizon can introduce additional leakage (Thyagarajan et al., 2015).

## Foreground Subtraction

A more direct approach to suppressing foreground contamination is to model and remove as much of the contamination as possible. This has been the focus of the LOFAR EoR KSP, which has dedicated substantial resources towards subtracting all of the radio emission in their deep fields (Patil et al., 2017). In total within a  $3^{\circ}$  field of view, they have removed almost 21,000 sky components down to a limit of 3 mJy using over 100 direction-dependent calibrations to account for beam and

ionospheric errors.

On top of this modeling effort, Patil et al. (2017) applied Generalized Morphological Component Analysis (GMCA; Chapman et al., 2013) to suppress the residual contamination. GMCA is a blind technique for decomposing the remaining emission into a number of statistically independent components. In fact, the implementation used here did not incorporate any prior astrophysical information about the nature of the foreground emission, which raises the possibility of subtracting the cosmological 21 cm emission alongside the foreground emission. Chapman et al. (2013) showed that they could recover the 21 cm signal for simulated LOFAR data with signal loss between 10–40%, but real instrumental considerations could drive the signal loss higher. Future iterations of this technique will likely need to build in some prior astrophysical information.

Unanticipated signal loss is not a new problem to foreground subtraction efforts. Paciga et al. (2013) used detailed simulations to compute the signal loss when removing foreground emission using a Singular Value Decomposition (SVD), which is another blind technique for subtracting foreground emission. Similarly Patil et al. (2016) realized that their process for removing point sources with a direction-dependent calibration was also capable of unintentionally removing diffuse foreground emission. Finally, Cheng et al. (in prep.) discovered that using a covariance matrix derived from the measured data can lead to signal loss due to the down-weighting of the cosmological 21 cm signal.

### **Instrumental Calibration**

The process of avoiding or subtracting foreground emission is compounded by the difficulty of calibrating low-frequency interferometers. With a field of view typically  $\gtrsim 10^\circ$  across and a proclivity for the most troublesome sources to be far from the delay center (see Figure 1.5), a detailed understanding of the—potentially inhomogeneous—antenna response pattern is essential. For instance, Shaw et al. (2015) concluded that the Canadian Hydrogen Intensity Mapping Experiment (CHIME) must measure its beam to better than one part in  $10^{-4}$  to avoid biasing a measurement of the power spectrum. Furthermore, a standard sky-based calibration procedure will require a model for the entire field of view. An incomplete sky model will introduce ripples into the bandpass that impedes the observer’s ability to separate foreground emission from the cosmological 21 cm emission (e.g., Figure 1.5; Barry et al., 2016; Ewall-Wice et al., 2017).

In order to address some of the difficulties associated with sky-based calibration, some power spectrum experiments—notably PAPER and HERA—have implemented redundant baseline calibration (Liu et al., 2010). While redundant calibration is useful for discovering instrumental errors and deriving calibration parameters in a way that is robust to modeling errors, there are some calibration parameters that cannot be constrained with redundant calibration. Notably this includes the overall bandpass, which must still be measured from the spectrum of a known point source. Yet at this time, few flux calibrators exist at frequencies below 200 MHz (Scaife & Heald, 2012; Perley & Butler, 2017).

Propagation effects through the ionosphere additionally complicate low-frequency observations. The refractive index of the ionosphere  $n = \sqrt{1 - v_{\text{plasma}}^2/v^2}$ , where the plasma frequency  $v_{\text{plasma}}$  is typically  $\sim 10$  MHz. When the diffractive scale of the ionosphere is small, point sources can break apart into multiple images (Vedantham & Koopmans, 2015), but even when ionospheric conditions are mild, it can still contribute 50% amplitude scintillation on 13 s timescales and 20' variable refractive offsets on 10 minute timescales (see §3.3). At least while conditions are mild, ionospheric propagation effects may be described with a direction-dependent calibration. However, as previously discussed, direction-dependent calibration may lead to unintentional signal loss, and must therefore be applied judiciously.

## 1.5 Future Outlook

Despite the practical difficulties involved in detecting the 21 cm transition from the EoR and Cosmic Dawn, it promises to open up a new window towards the high-redshift universe and the first generation of stars and galaxies. Recently, a significant development came from the first putative detection of the Cosmic Dawn through the global 21 cm signal by the EDGES experiment (Bowman et al., 2018). In this paper, the authors claimed the detection of an absorption feature centered at 78 MHz ( $z \sim 17$ ), which they attribute to early star formation and heating (see Figure 1.6).

The absorption feature reported by Bowman et al. (2018) is remarkable for its extreme amplitude ( $\sim 500$  mK), which cannot be attained through purely adiabatic cooling of the IGM. Currently there is some skepticism in regards to how EDGES modeled and subtracted foreground emission (Hills et al., 2018), but the result has nevertheless sparked a flurry of new ideas ranging from the absurd (i.e.,  $\Omega_m = \Omega_b$ ) to the exotic. The most plausible of these theories are new ideas for either cooling the IGM (e.g., Barkana, 2018) or positing a new source of radio emission originating

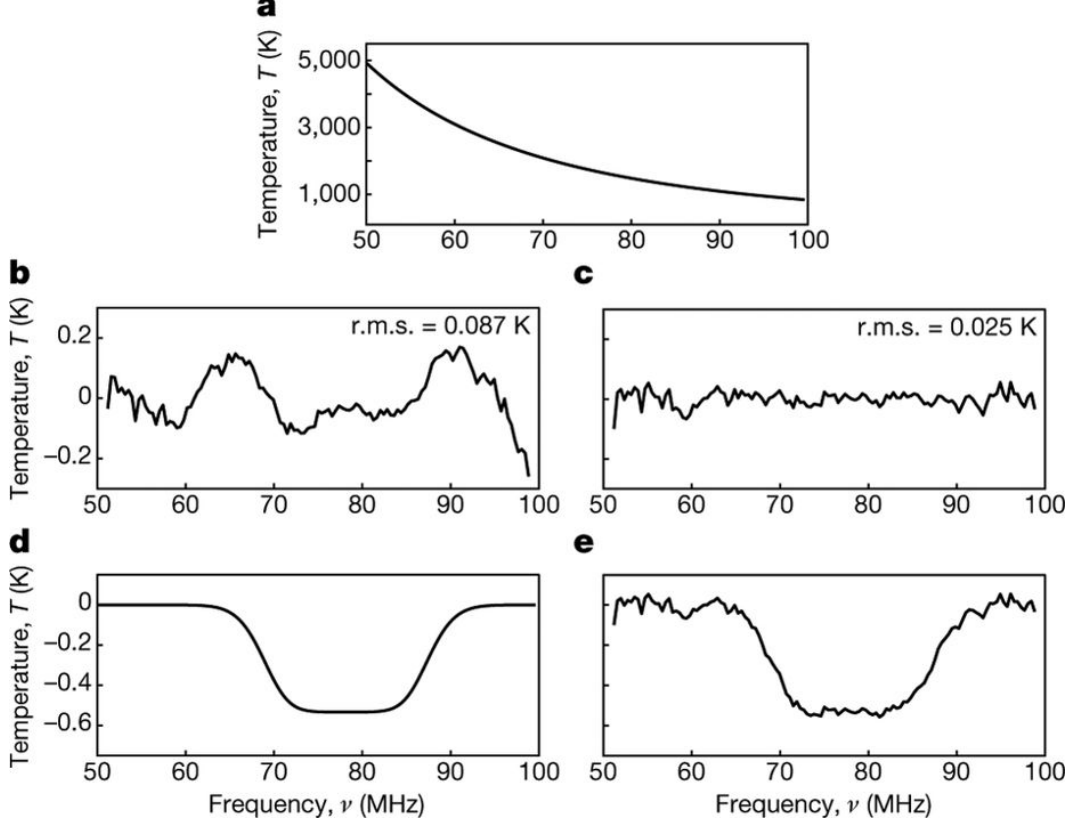


Figure 1.6: (a) The calibrated sky spectrum measured by the EDGES experiment. (b) The residuals after fitting a model of the foreground emission. (c) The residuals after performing a joint fit of the foreground emission and an absorption trough. (d) The best-fit absorption trough. (e) The best-fit absorption trough including residual noise. This figure is reproduced with permission from Bowman et al. (2018).

from  $z > 20$  (e.g., Ewall-Wice et al., 2018).

As an example, Barkana (2018) noted that because Compton scattering of CMB photons off of residual free electrons after recombination heats the baryons until  $z \sim 150$ , the dark matter has been able to cool adiabatically for longer and therefore has a lower temperature. A potential interaction between baryons and dark matter could therefore allow the baryons to cool super-adiabatically. In this scenario, the amplitude of the 21 cm power spectrum at  $z \sim 17$  is expected to be  $\sim (140 \text{ mK})^2$ , substantially larger than previous predictions. In a separate paper, Barkana et al. (2018) also argued that existing dark matter experiments make this possibility somewhat unlikely, which is a reflection of the fact that this initial detection has produced more questions than answers.

Power spectrum experiments can offer an independent verification and continue to

advance in sophistication and sensitivity with upgrades to LOFAR, the MWA, and the construction of the Hydrogen Epoch of Reionization Array (HERA; DeBoer et al., 2017). HERA will be composed of  $\sim 350$  parabolic dishes (each 14 m in diameter) hexagonally packed within a core 300 m across. Each dish will be equipped with a feed that operates between 50 and 250 MHz ( $z \sim 5 - 27$ ). HERA incorporates lessons learned from the preceding PAPER experiment, and so with a major increase in collecting area with respect to PAPER, promises to deliver a compelling detection of the 21 cm power spectrum. On even longer timescales, the SKA may be capable of constructing a tomographic map of the universe through the 21 cm transition (Mellema et al., 2013).

At Caltech, multiple experiments are attempting to measure spectral features from the EoR and Cosmic Dawn. The Owens Valley Radio Observatory Long Wavelength Array (OVRO-LWA) is a 288 element interferometer with instantaneous bandwidth covering 30–85 MHz. In this thesis I will present, to date, the highest angular-resolution maps of the sky available below 100 MHz using the OVRO-LWA and a new imaging technique designed for drift-scanning interferometers. These maps have been made publicly available on the Legacy Archive for Microwave Background Data Analysis (LAMBDA).<sup>1</sup> I will also present the deepest upper limits on the amplitude of the 21 cm power spectrum of the Cosmic Dawn, and the only existing limits at  $z > 18$ . Figure 1.7 presents a radial map of the universe that compares the comoving radial distances probed by the OVRO-LWA and HERA to other probes of the high-redshift universe.

These measurements are highly complementary to other ongoing experiments at Caltech, notably the CO Mapping Array Pathfinder (COMAP; Cleary et al., 2016) and the Tomographic Ionized carbon Intensity Mapping Experiment Pilot (TIME-Pilot; Crites et al., 2017), which aim to ultimately detect transitions of CO and C II from the EoR respectively. While the 21 cm power spectrum of the EoR originates from the neutral gas surrounding the expanding ionized bubbles, CO and C II emission originates from the sites of star formation, therefore helping to build a more complete picture of the EoR. Furthermore, correlations with the 21 cm signal will help to mitigate systematics in both measurements.

In Chapter 2 I will introduce the OVRO-LWA, its construction, commissioning, and the its calibration. In Chapter 3 I will describe Tikhonov-regularized  $m$ -mode analysis imaging and cleaning, and demonstrate its application by generating maps

---

<sup>1</sup> <https://lambda.gsfc.nasa.gov/>

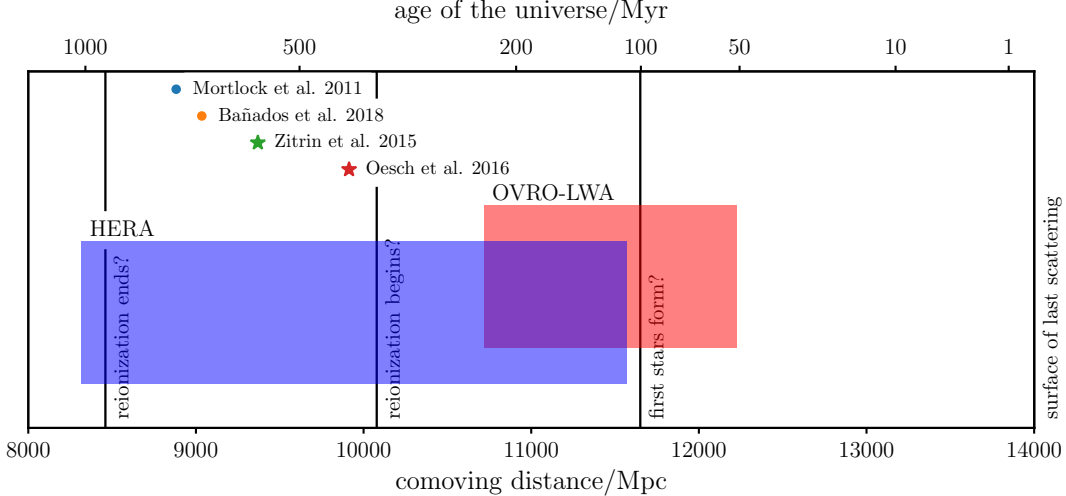


Figure 1.7: A radial map of the universe. Known quasars are marked with circles and galaxies are marked with stars. The range of comoving distances probed by the OVRO-LWA and HERA are marked with a red rectangle and a blue rectangle respectively.

of the full sky visible from OVRO with  $15'$  angular resolution. In Chapter 4 I will present the most sensitive upper limits on the 21 cm power spectrum of the Cosmic Dawn using a new technique for foreground filtering, and finally in Chapter A I will present my conclusions.

## Bibliography

- Ali, Z. S., Parsons, A. R., Zheng, H., et al. 2015, ApJ, 809, 61
- Alvarez, H., Aparici, J., May, J., & Olmos, F. 1997, A&AS, 124, 205
- Baars, J. W. M., Genzel, R., Pauliny-Toth, I. I. K., & Witzel, A. 1977, A&A, 61, 99
- Barkana, R. 2018, Nature, 555, 71
- Barkana, R., Outmezguine, N. J., Redigolo, D., & Volansky, T. 2018, ArXiv e-prints, arXiv:1803.03091
- Barry, N., Hazelton, B., Sullivan, I., Morales, M. F., & Pober, J. C. 2016, MNRAS, 461, 3135
- Bañados, E., Venemans, B. P., Mazzucchelli, C., et al. 2018, Nature, 553, 473
- Beardsley, A. P., Hazelton, B. J., Sullivan, I. S., et al. 2016, ApJ, 833, 102
- Bowman, J. D., & Rogers, A. E. E. 2010, Nature, 468, 796

- Bowman, J. D., Rogers, A. E. E., Monsalve, R. A., Mozdzen, T. J., & Mahesh, N. 2018, *Nature*, 555, 67
- Chang, T.-C., Pen, U.-L., Bandura, K., & Peterson, J. B. 2010, *Nature*, 466, 463
- Chapman, E., Abdalla, F. B., Bobin, J., et al. 2013, *MNRAS*, 429, 165
- Cleary, K., Bigot-Sazy, M.-A., Chung, D., et al. 2016, in American Astronomical Society Meeting Abstracts, Vol. 227, American Astronomical Society Meeting Abstracts #227, 426.06
- Colless, M., Dalton, G., Maddox, S., et al. 2001, *MNRAS*, 328, 1039
- Crites, A., Bock, J., Bradford, M., et al. 2017, in American Astronomical Society Meeting Abstracts, Vol. 229, American Astronomical Society Meeting Abstracts #229, 125.01
- de Oliveira-Costa, A., Tegmark, M., Gaensler, B. M., et al. 2008, *MNRAS*, 388, 247
- DeBoer, D. R., Parsons, A. R., Aguirre, J. E., et al. 2017, *PASP*, 129, 045001
- Ewall-Wice, A., Chang, T.-C., Lazio, J., et al. 2018, ArXiv e-prints, arXiv:1803.01815
- Ewall-Wice, A., Dillon, J. S., Liu, A., & Hewitt, J. 2017, *MNRAS*, 470, 1849
- Ewall-Wice, A., Dillon, J. S., Hewitt, J. N., et al. 2016, *MNRAS*, 460, 4320
- Fan, X., Strauss, M. A., Becker, R. H., et al. 2006, *AJ*, 132, 117
- Fialkov, A., Barkana, R., Pinhas, A., & Visbal, E. 2014, *MNRAS*, 437, L36
- Fialkov, A., Barkana, R., Visbal, E., Tseliakhovich, D., & Hirata, C. M. 2013, *MNRAS*, 432, 2909
- Field, G. B. 1958, *Proceedings of the IRE*, 46, 240
- Furlanetto, S. R., Oh, S. P., & Briggs, F. H. 2006, *Phys. Rep.*, 433, 181
- Greig, B., & Mesinger, A. 2015, *MNRAS*, 449, 4246
- . 2017, *MNRAS*, 472, 2651
- Guzmán, A. E., May, J., Alvarez, H., & Maeda, K. 2011, *A&A*, 525, A138
- Haslam, C. G. T., Klein, U., Salter, C. J., et al. 1981, *A&A*, 100, 209
- Haslam, C. G. T., Salter, C. J., Stoffel, H., & Wilson, W. E. 1982, *A&AS*, 47, 1
- Hills, R., Kulkarni, G., Meerburg, P. D., & Puchwein, E. 2018, ArXiv e-prints, arXiv:1805.01421

- Hinshaw, G., Larson, D., Komatsu, E., et al. 2013, ApJS, 208, 19
- Jacobs, D. C., Hazelton, B. J., Trott, C. M., et al. 2016, ApJ, 825, 114
- Koopmans, L. V. E. 2017, Proceedings of the International Astronomical Union, 12, 71–76
- Liu, A., Pritchard, J. R., Tegmark, M., & Loeb, A. 2013, Phys. Rev. D, 87, 043002
- Liu, A., Tegmark, M., Morrison, S., Lutomirski, A., & Zaldarriaga, M. 2010, MNRAS, 408, 1029
- Madau, P., Meiksin, A., & Rees, M. J. 1997, ApJ, 475, 429
- Maeda, K., Alvarez, H., Aparici, J., May, J., & Reich, P. 1999, A&AS, 140, 145
- Mellema, G., Koopmans, L. V. E., Abdalla, F. A., et al. 2013, Experimental Astronomy, 36, 235
- Monsalve, R. A., Rogers, A. E. E., Bowman, J. D., & Mozdzen, T. J. 2017, ApJ, 847, 64
- Morales, M. F., Hazelton, B., Sullivan, I., & Beardsley, A. 2012, ApJ, 752, 137
- Mortlock, D. J., Warren, S. J., Venemans, B. P., et al. 2011, Nature, 474, 616
- Mozdzen, T. J., Bowman, J. D., Monsalve, R. A., & Rogers, A. E. E. 2017, MNRAS, 464, 4995
- Oesch, P. A., Brammer, G., van Dokkum, P. G., et al. 2016, ApJ, 819, 129
- Paciga, G., Chang, T.-C., Gupta, Y., et al. 2011, MNRAS, 413, 1174
- Paciga, G., Albert, J. G., Bandura, K., et al. 2013, MNRAS, 433, 639
- Parsons, A. R., Pober, J. C., Aguirre, J. E., et al. 2012, ApJ, 756, 165
- Parsons, A. R., Backer, D. C., Foster, G. S., et al. 2010, AJ, 139, 1468
- Parsons, A. R., Liu, A., Aguirre, J. E., et al. 2014, ApJ, 788, 106
- Patil, A. H., Yatawatta, S., Zaroubi, S., et al. 2016, MNRAS, 463, 4317
- Patil, A. H., Yatawatta, S., Koopmans, L. V. E., et al. 2017, ApJ, 838, 65
- Penzias, A. A., & Wilson, R. W. 1965, ApJ, 142, 419
- Perley, R. A., & Butler, B. J. 2017, ApJS, 230, 7
- Perlmutter, S., Aldering, G., Goldhaber, G., et al. 1999, ApJ, 517, 565
- Planck Collaboration, Ade, P. A. R., Aghanim, N., et al. 2016a, A&A, 594, A25

- Planck Collaboration, Adam, R., Aghanim, N., et al. 2016b, *A&A*, 596, A108
- Presley, M. E., Liu, A., & Parsons, A. R. 2015, *ApJ*, 809, 18
- Price, D. C., Greenhill, L. J., Fialkov, A., et al. 2018, *MNRAS*, 478, 4193
- Pritchard, J. R., & Loeb, A. 2012, *Reports on Progress in Physics*, 75, 086901
- Riess, A. G., Filippenko, A. V., Challis, P., et al. 1998, *AJ*, 116, 1009
- Robertson, B. E., Ellis, R. S., Furlanetto, S. R., & Dunlop, J. S. 2015, *ApJ*, 802, L19
- Roger, R. S., Costain, C. H., Landecker, T. L., & Swerdluk, C. M. 1999, *A&AS*, 137, 7
- Scaife, A. M. M., & Heald, G. H. 2012, *MNRAS*, 423, L30
- Schmidt, M. 1963, *Nature*, 197, 1040
- Shaw, J. R., Sigurdson, K., Sitwell, M., Stebbins, A., & Pen, U.-L. 2015, *Phys. Rev. D*, 91, 083514
- Singh, S., Subrahmanyam, R., Udaya Shankar, N., & Raghunathan, A. 2015, *ApJ*, 815, 88
- Singh, S., Subrahmanyam, R., Udaya Shankar, N., et al. 2017, *ApJ*, 845, L12
- Smoot, G. F., Bennett, C. L., Kogut, A., et al. 1992, *ApJ*, 396, L1
- Steidel, C. C., Giavalisco, M., Pettini, M., Dickinson, M., & Adelberger, K. L. 1996, *ApJ*, 462, L17
- Thyagarajan, N., Jacobs, D. C., Bowman, J. D., et al. 2015, *ApJ*, 804, 14
- Vedantham, H. K., & Koopmans, L. V. E. 2015, *MNRAS*, 453, 925
- Vedantham, H. K., Koopmans, L. V. E., de Bruyn, A. G., et al. 2015, *MNRAS*, 450, 2291
- Venumadhav, T., Chang, T.-C., Doré, O., & Hirata, C. M. 2016, *ApJ*, 826, 116
- Wouthuysen, S. A. 1952, *AJ*, 57, 31
- Zitrin, A., Labb  , I., Belli, S., et al. 2015, *ApJ*, 810, L12

## Chapter 2

# A PATH TOWARDS CALIBRATION OF THE OVRO-LWA

### 2.1 Design and Construction of the OVRO-LWA

The OVRO-LWA is a new low-frequency (27–85 MHz instantaneous) radio interferometer constructed during the course of this thesis and located near Big Pine, California. Construction began in 2013 with the first antenna completed in March of that year (see Figure 2.1).

The OVRO-LWA was initially composed of 256 antennas, with 251 of those antennas arranged within a dense 200 m diameter core in a configuration that is optimized for sidelobe levels in snapshot imaging. Each of these antennas consists of two crossed broadband dipoles with an active balun/preamp, and the entire system is sky noise dominated over the range 20–80 MHz (Hicks et al., 2012). A picture of an OVRO-LWA antenna can be seen in Figure 2.2. The primary beam of each OVRO-LWA antenna subtends a solid angle of  $\sim 8000 \text{ deg}^2$ , with sensitivity to the entire visible hemisphere of the sky.

ARX boards

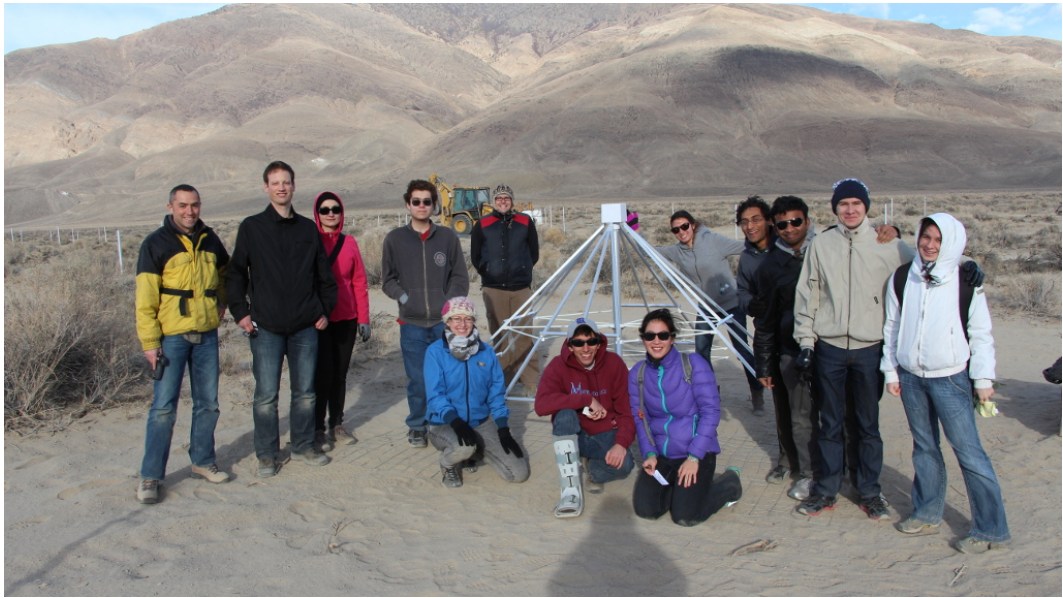


Figure 2.1: The first OVRO-LWA completed on 2013 March 8 with the class of Ay 122b (including the author of this thesis with the fractured ankle).

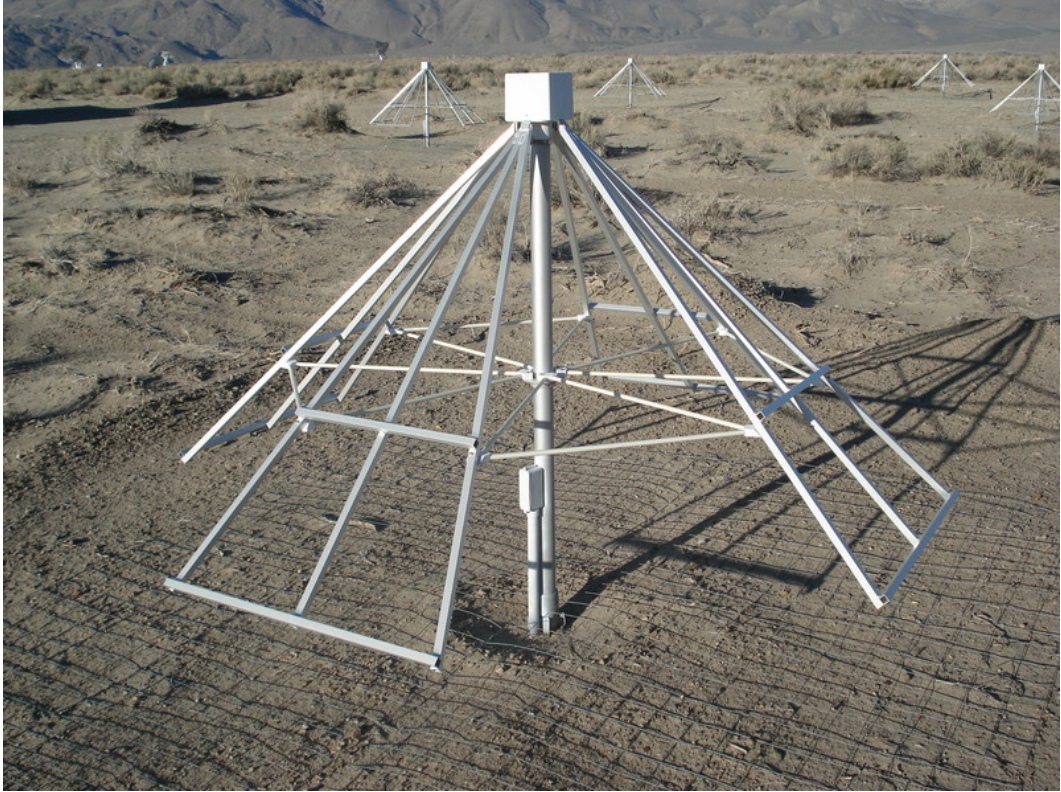


Figure 2.2: Picture of an OVRO-LWA antenna.

The remaining five antennas are isolated from the core of the OVRO-LWA and equipped with radiometric front ends as part of the LEDA experiment, which is attempting to measure the globally averaged signal of H I from the Cosmic Dawn (Price et al., 2018). The OVRO-LWA hosts the LEDA correlator as its back-end, which is an FX correlator composed of 16 ROACH2 FPGAs that compose the F stage, and 11 servers each with dual NVIDIA K20X GPUs that compose the X stage (Kocz et al., 2015). This allows the correlator to perform full cross-correlation of 512 input signals with 58 MHz instantaneous bandwidth.

During observations, data is streamed from the LEDA correlator to the All-Sky Transient Monitor (ASTM), which houses the compute nodes used for post-processing and imaging. The ASTM is composed of 10 identical nodes each with a 16-core Intel Xeon E5-2630 v3 CPU and 64 GB of memory. Five additional servers provide 565 TB of storage capacity through the Lustre high performance file system.

The initial 256 antenna interferometer was therefore capable of imaging the entire visible hemisphere in snapshot images with  $1^\circ$  angular resolution. An example snapshot image can be seen in Figure 2.3. In 2015, an additional 32 antennas were

installed that extended the maximum baseline of the interferometer to 1.5 km and improved the angular resolution to 8'. This improved angular resolution can be seen in Figure 2.4. In a final future stage of development, an additional 64 antennas will be installed that extend the maximum baseline to 2.6 km, which will see improved *uv*-coverage at long baselines and improved 5' angular resolution.

While this thesis focuses on the use of the OVRO-LWA to detect the high-redshift signature of neutral hydrogen from the Cosmic Dawn, the OVRO-LWA facilitates a diverse set of scientific motivations including the study of stellar and planetary magnetospheres, radio follow-up of gamma ray bursts (Anderson et al., 2017) and neutron star mergers, solar dynamic imaging spectroscopy, and the detection of high energy cosmic rays (Monroe, 2018).

With the exception of detecting high energy cosmic rays—which uses a custom firmware and processing pipeline that cannot operate in parallel with ordinary correlation—there are two complementary software pipelines that service the scientific goals of the OVRO-LWA:

1. A widefield snapshot imaging pipeline that images the entire visible hemisphere every 13 s using WSCLEAN (Offringa et al., 2014).
2. A novel approach specialized for drift-scanning interferometers that can image the entire sky (above a limiting declination) in a single synthesis imaging step.

This chapter will describe the calibration, source removal routines purpose built for the OVRO-LWA and used by both pipelines. Additionally, in §2.4 I will discuss some of the challenges involved with commissioning the OVRO-LWA that have been overcome to bring the OVRO-LWA into existence, to first light, and finally its first scientific results. Finally, the latter pipeline will be discussed in considerable depth in Chapters 3 and 4.

## 2.2 Calibration of a Low-Frequency Interferometer

The purpose of calibration is to remove the contribution of the antenna and receivers, including any gain, filters, and propagation effects along the signal path. At low radio frequencies, the Earth's ionosphere is additionally important due to the effects of electromagnetic waves propagating through a magnetized plasma.

Further, we will make a distinction between a “direction-independent” calibration and a “direction-dependent” calibration. The former can correct for the response



Figure 2.3: Snapshot image of the sky captured with the OVRO-LWA and using only the antennas located within the core of the array. The image covers the entire visible hemisphere in sine-projection. A similar image constructed using the newer long-baseline antennas can be seen in Figure 2.4.

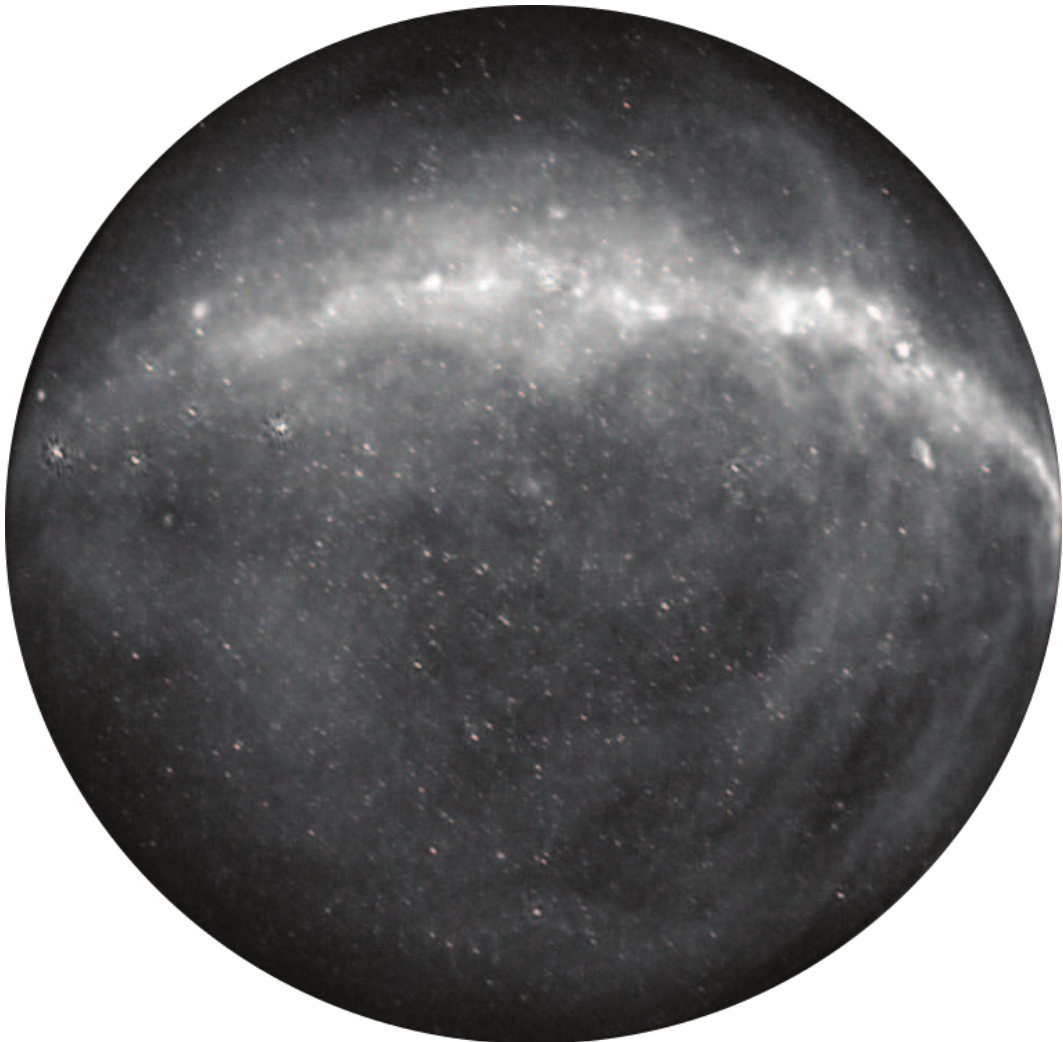


Figure 2.4: Snapshot image of the sky captured with the OVRO-LWA and using the new long-baseline antennas. The image covers the entire visible hemisphere in sine-projection. A similar image constructed using only the core of the interferometer can be seen in Figure 2.3.

of the receiver and signal path, but cannot fully account for the antenna response pattern and ionospheric effects. The latter allows for the calibration parameters to vary as a function of direction on the sky, which can account for errors due to the antenna beam and some ionospheric effects.

Neglecting complexity associated with polarized imaging for now, a direction-independent calibration amounts to determining the complex-valued gain  $g_i(\nu)$  associated with each signal path  $i$  and frequency  $\nu$ . These gains effect the measured correlation between the signal paths  $i$  and  $j$  such that

$$V_{ij}^{\text{measured}}(\nu) = g_i(\nu) g_j^*(\nu) V_{ij}^{\text{true}}(\nu) + \text{noise}, \quad (2.1)$$

where  $V_{ij}^{\text{measured}}$  is the visibility actually measured between the corresponding signal paths at the frequency  $\nu$ , and  $V_{ij}^{\text{true}}$  is the visibility that would have been measured if instead we had correlated the value of the electric field at the electrical center of each antenna without the need for any additional electronics. The true visibility can be computed from the sky brightness  $I(\nu, \hat{r})$  at the frequency  $\nu$  and direction  $\hat{r}$  such that

$$V_{ij}^{\text{true}}(\nu) = \int a_i(\nu, \hat{r}) a_j^*(\nu, \hat{r}) I(\nu, \hat{r}) \exp\left(2\pi i \hat{r} \cdot \vec{b}_{ij}/\lambda\right) d\Omega, \quad (2.2)$$

where the integral runs over solid angle  $\Omega$ ,  $a_i(\nu, \hat{r})$  is the response of the corresponding antenna at the frequency  $\nu$  to the direction  $\hat{r}$ ,  $\vec{b}_{ij}$  is the baseline separating the antennas for signal paths  $i$  and  $j$ , and  $\lambda$  is the wavelength. If the sky is assumed to be composed of point sources, then

$$V_{ij}^{\text{true}}(\nu) = \sum_k a_i(\nu, \hat{r}_k) a_j^*(\nu, \hat{r}_k) F_k(\nu) \exp\left(2\pi i \hat{r}_k \cdot \vec{b}_{ij}/\lambda\right), \quad (2.3)$$

where  $F_k$  is the flux of the  $k$ th point source in the direction  $\hat{r}_k$ .

A typical calibration strategy using, for example, the Very Large Array (VLA) involves periodically pointing at a known compact point source. For a compact point source at the phase center, the phase of all visibilities is zero, and the amplitude is given by the known flux of the source. Periodically revisiting this source allows for the observer to establish the time variation of the calibration parameters. Each time the observer solves for the gains that minimize

$$\chi^2 \propto \sum_{i \neq j} \left\| V_{ij}^{\text{measured}}(\nu) - g_i(\nu) g_j^*(\nu) F \right\|^2, \quad (2.4)$$

where  $F$  is the flux of the isolated point source.

This optimization can be performed with rapid convergence using a variant of alternating least-squares developed by Mitchell et al. (2008) and Salvini & Wijnholds (2014). At each iteration this algorithm applies linear least-squares to minimize  $\chi^2$  while holding one set of gains constant:

$$g_i \leftarrow \frac{\sum_{i \neq j} g_j^* V_{ij}^{\text{model},*} V_{ij}^{\text{measured}}}{\sum_{i \neq j} \|g_j V_{ij}^{\text{model}}\|^2}, \quad (2.5)$$

where we have now allowed for a more general sky model to be used during calibration by introducing the model visibilities  $V_{ij}^{\text{model}}$ , which are the true visibilities for an assumed model of the sky. Naively applying Equation 2.5 will result in poor convergence due to oscillations about the true minimum of  $\chi^2$ . These oscillations can be damped by averaging subsequent iterations, and Salvini & Wijnholds (2014) demonstrated that this simple gradient-free optimization strategy converges remarkably quickly.

The OVRO-LWA is capable of imaging the entire hemisphere in a snapshot image. This brings its own unique calibration challenges because it is currently impossible to isolate a single compact point source within the field of view of the interferometer.<sup>1</sup> Due to the wide field of view, determining an accurate gain calibration relies on a detailed sky and antenna beam model. Mistakes or omissions in the sky model can, for example, generate artificial ripples in the bandpass that will impact the interferometer’s ability to cleanly separate foreground emission from cosmological 21 cm emission (Barry et al., 2016; Ewall-Wice et al., 2017).

Furthermore, at frequencies  $\nu < 100$  MHz there are few flux calibrators. Baars et al. (1977) determined the absolute spectrum of Cyg A between 20 MHz and 2 GHz. Scaife & Heald (2012) added six additional calibrators, and Perley & Butler (2017) used the VLA 4-band system to bring the total number of available calibrators to 11. However, in Chapter 3 I will show that the latter spectra can diverge substantially from truth below 50 MHz.

Detailed sky and beam models are therefore generally an important calibration requirement for low-frequency interferometers. In Chapter 3, I will also derive an empirical beam model for the OVRO-LWA and developed a new imaging formalism that captures the entire visible sky in a single synthesis imaging step that can be used as part of a self-calibration loop (Readhead & Wilkinson, 1978).

---

<sup>1</sup> Gated pulsar observations could, in principle, achieve this isolation. This capability is a key development area for the OVRO-LWA.

As part of this thesis I developed the TTCal calibration routine for the purpose of calibrating the OVRO-LWA. It implements the alternating least-squares algorithm described above to solve for the complex-valued gain of each signal path from a model sky composed of any number of point sources, Gaussians, and shapelet components (Refregier, 2003). If desired, TTCal may instead solve for the Jones matrix associated with each antenna for a fully polarized calibration solution. TTCal is freely available under the GPLv3 license or any under later version.<sup>2</sup>

### 2.3 Source Removal and Direction-Dependent Calibration

The large field of view of the OVRO-LWA comes with additional challenges associated with the ionosphere, inhomogeneous primary beams, and mutual coupling between antennas.

The dispersion relation for electromagnetic waves propagating in a plasma is

$$\omega^2 = \omega_{\text{plasma}}^2 + c^2 k^2, \quad (2.6)$$

where  $\omega$  is the angular frequency of the oscillations,  $k$  is the wavenumber,  $c$  is the speed of light, and  $\omega_{\text{plasma}}$  is the plasma frequency—the frequency of electrostatic oscillations within the plasma. The plasma frequency (in SI units) is given by

$$\omega_{\text{plasma}} = \sqrt{\frac{n_e e^2}{m_e \epsilon_0}}, \quad (2.7)$$

where  $n_e$  is the number density of electrons,  $e$  is the charge of the electron,  $m_e$  is the mass of the electron, and  $\epsilon_0$  is the permittivity of free space. For Earth's ionosphere, the plasma frequency is typically  $\sim 2\pi \times 10$  MHz. The index of refraction is

$$n = \sqrt{1 - \frac{\omega_{\text{plasma}}^2}{\omega^2}} \approx 1 - \frac{1}{2} \frac{\omega_{\text{plasma}}^2}{\omega^2}, \quad (2.8)$$

where the approximation holds if  $\omega^2 \gg \omega_{\text{plasma}}^2$ . In this regime, the arrival time of a burst of radio emission is  $\propto \nu^{-2}$  as is commonly seen in pulsar astronomy. The additional phase imparted is, however,  $\propto \nu^{-1}$  such that along a given line of sight the phase can be parameterized as

$$\phi \approx \phi_0 + \overbrace{2\pi\tau\nu}^{\text{delay}} + \underbrace{\frac{e^2}{4\pi m_e c \epsilon_0} \frac{1}{\nu} \int n_e dl}_{\text{ionospheric dispersion}}, \quad (2.9)$$

---

<sup>2</sup> <https://github.com/mweastwood/TTCal.jl>

where  $\phi_0$  sets the overall phase,  $\tau$  is the delay, and the integral of the electron number density along the line of sight is called the Total Electron Content (TEC).

The diffractive scale  $r_{\text{diff}}$  of the ionosphere is the length scale over which the phase variance is  $1 \text{ rad}^2$ . The Fresnel scale is  $r_f = \sqrt{\lambda D / 2\pi}$  where  $D$  is the height of the ionosphere (typically  $\sim 300 \text{ km}$ ). In the weak scattering regime ( $r_{\text{diff}} \gg r_f$ ), the ionosphere can contribute amplitude and phase scintillation, which may be folded into the antenna gain calibration. However, in the strong scattering regime ( $r_{\text{diff}} \lesssim r_f$ ), point sources may become multiply imaged, which cannot be described as a perturbation to the antenna response (Vedantham & Koopmans, 2015).

The antenna response is also generally expected to be inhomogeneous. Within the core of the OVRO-LWA antennas are separated by as little as 5 m. Ellingson (2011) studied the impact of mutual coupling on the antenna primary beam within the first Long Wavelength Array station in New Mexico (LWA1), which uses the same antennas and same 5 m minimum spacing as the OVRO-LWA, but the antennas are packed within a 100 m diameter (as opposed to a 200 m diameter for the OVRO-LWA). The authors found that, between 20–74 MHz, when pointing more than  $10^\circ$ – $20^\circ$  from zenith, mutual coupling and correlated galactic noise led to a 2–6 dB increase in the system equivalent flux density (SEFD), and 1–2 dB deviations in the primary beam pattern between antennas. We expect comparable effects for the OVRO-LWA.

Direction-dependent calibration therefore attempts to account for ionospheric scintillation and refraction, and inhomogeneous antenna beams by allowing the antenna response in Equation 2.3 to be a free parameter.

## TTCal

### 2.4 Commissioning Challenges

#### Computing Antenna Positions

Early images produced by the OVRO-LWA (prior to 2015 October 16) were afflicted by an apparent rotation in the World Coordinate System (WCS).

#### RFI Localization

An ongoing challenge faced by the OVRO-LWA is the presence of broadband sources of RFI in the vicinity of the observatory. Due to the entire-hemisphere field of view of the OVRO-LWA, these sources appear as points on the horizon that limit the sensitivity of snapshot images through additional sidelobe noise.

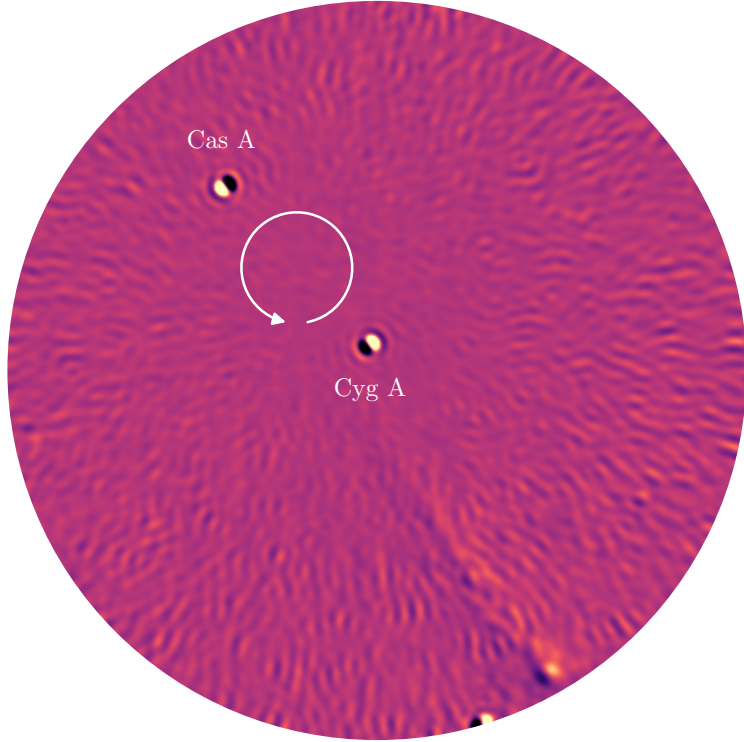


Figure 2.5: Illustration of the error in the WCS prior to a correction to the antenna positions. The image is a difference between an image constructed with the incorrect antenna positions and the corrected antenna positions. The arrow denotes the direction and approximate center of the rotation.

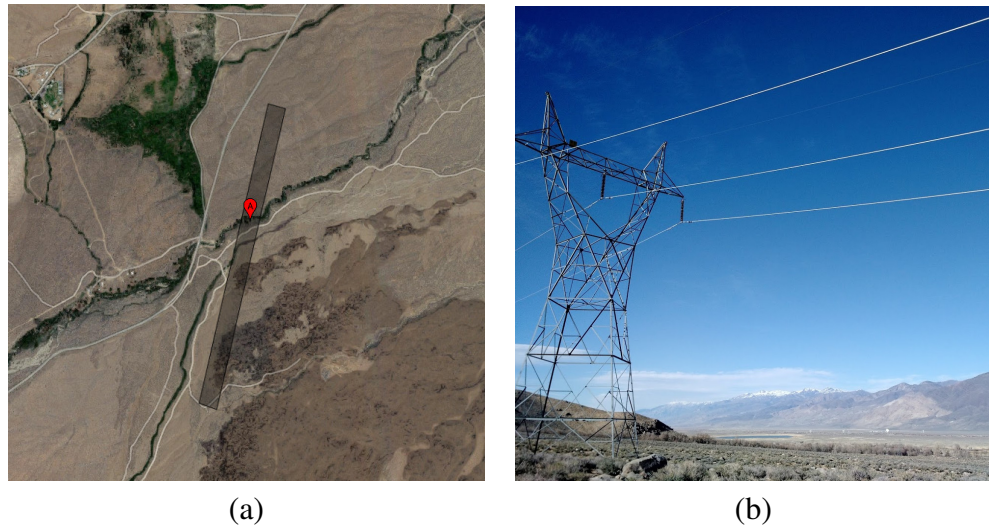


Figure 2.6: (a) The localization region for a source of RFI south of the OVRO-LWA and near the town of Big Pine. Satellite imagery ©2018 Google. Map data ©2018 Google. (b) Image of a high-voltage power line overlooking OVRO near the localization region.

Fortunately, because these sources are typically in the near-field of the interferometer, the curvature of the incoming wavefront can be used to infer the distance to each source of RFI.

The path difference from a source in the near-field of an interferometer located at the position  $(\xi, \eta, \zeta)$  to two antennas located respectively at  $(x_i, y_i, z_i)$  and  $(x_j, y_j, z_j)$  is

$$\Delta l_{ij}^{\text{near-field}} = \sqrt{(x_j - \xi)^2 + (y_j - \eta)^2 + (z_j - \zeta)^2} - \sqrt{(x_i - \xi)^2 + (y_i - \eta)^2 + (z_i - \zeta)^2}. \quad (2.10)$$

In the limit that the distance of the source goes to infinity, we recover the familiar expression

$$\Delta l_{ij}^{\text{far-field}} = \frac{1}{D} \left( (x_i - x_j) \xi + (y_i - y_j) \eta + (z_i - z_j) \zeta \right), \quad (2.11)$$

where  $D$  is the distance to the source. The correlation measured between two antennas for a source in the near-field of the interferometer is therefore

$$V_{ij} = F \exp \left( 2\pi i \frac{\Delta l_{ij}^{\text{near-field}}}{\lambda} \right), \quad (2.12)$$

where  $V_{ij}$  is the visibility measured between antennas  $i$  and  $j$ ,  $F$  is the apparent brightness of the source, and  $\lambda$  is the wavelength. Equation 2.12 can then be used to fit for the position of a source including its distance.

In order to improve sensitivity to these RFI sources,

## Bibliography

- Anderson, M. M., Hallinan, G., Eastwood, M. W., et al. 2017, ArXiv e-prints, arXiv:1711.06665
- Baars, J. W. M., Genzel, R., Pauliny-Toth, I. I. K., & Witzel, A. 1977, A&A, 61, 99
- Barry, N., Hazelton, B., Sullivan, I., Morales, M. F., & Pober, J. C. 2016, MNRAS, 461, 3135
- Ellingson, S. W. 2011, IEEE Transactions on Antennas and Propagation, 59, 1855
- Ewall-Wice, A., Dillon, J. S., Liu, A., & Hewitt, J. 2017, MNRAS, 470, 1849
- Hicks, B. C., Paravastu-Dalal, N., Stewart, K. P., et al. 2012, PASP, 124, 1090
- Kocz, J., Greenhill, L. J., Barsdell, B. R., et al. 2015, Journal of Astronomical Instrumentation, 4, 1550003

- Mitchell, D. A., Greenhill, L. J., Wayth, R. B., et al. 2008, IEEE Journal of Selected Topics in Signal Processing, 2, 707
- Monroe, R. M. 2018, PhD thesis, California Institute of Technology. <http://resolver.caltech.edu/CaltechTHESIS:06042018-004220017>
- Offringa, A. R., McKinley, B., Hurley-Walker, N., et al. 2014, MNRAS, 444, 606
- Perley, R. A., & Butler, B. J. 2017, ApJS, 230, 7
- Price, D. C., Greenhill, L. J., Fialkov, A., et al. 2018, MNRAS, 478, 4193
- Readhead, A. C. S., & Wilkinson, P. N. 1978, ApJ, 223, 25
- Refregier, A. 2003, MNRAS, 338, 35
- Salvini, S., & Wijnholds, S. J. 2014, A&A, 571, A97
- Scaife, A. M. M., & Heald, G. H. 2012, MNRAS, 423, L30
- Vedantham, H. K., & Koopmans, L. V. E. 2015, MNRAS, 453, 925

### Chapter 3

## THE RADIO SKY AT METER WAVELENGTHS: *M*-MODE ANALYSIS IMAGING WITH THE OVRO-LWA

Eastwood, M. W., Anderson, M. M., Monroe, R. M., et al. 2018, The Astronomical Journal, 156, 32. <http://stacks.iop.org/1538-3881/156/i=1/a=32>

### **Abstract**

A host of new low-frequency radio telescopes seek to measure the 21 cm transition of neutral hydrogen from the early universe. These telescopes have the potential to directly probe star and galaxy formation at redshifts  $20 \gtrsim z \gtrsim 7$ , but are limited by the dynamic range they can achieve against foreground sources of low-frequency radio emission. Consequently, there is a growing demand for modern, high-fidelity maps of the sky at frequencies below 200 MHz for use in foreground modeling and removal. We describe a new wide-field imaging technique for drift-scanning interferometers: Tikhonov-regularized *m*-mode analysis imaging. This technique constructs images of the entire sky in a single synthesis imaging step with exact treatment of wide-field effects. We describe how the CLEAN algorithm can be adapted to deconvolve maps generated by *m*-mode analysis imaging. We demonstrate Tikhonov-regularized *m*-mode analysis imaging using the Owens Valley Radio Observatory Long Wavelength Array (OVRO-LWA) by generating eight new maps of the sky north of  $\delta = -30^\circ$  with 15' angular resolution at frequencies evenly spaced between 36.528 and 73.152 MHz, and  $\sim 800$  mJy/beam thermal noise. These maps are a 10-fold improvement in angular resolution over existing full-sky maps at comparable frequencies, which have angular resolutions  $\geq 2^\circ$ . Each map is constructed exclusively from interferometric observations and does not represent the globally averaged sky brightness. Future improvements will incorporate total power radiometry, improved thermal noise, and improved angular resolution due to the planned expansion of the OVRO-LWA to 2.6 km baselines. These maps serve as a first step on the path to the use of more sophisticated foreground filters in 21 cm cosmology incorporating the measured angular and frequency structure of all foreground contaminants.

### 3.1 Introduction

At redshifts  $20 \gtrsim z \gtrsim 7$ , the 21 cm hyperfine structure line of neutral hydrogen is expected to produce a 10 to 100 mK perturbation in the cosmic microwave background (CMB) spectrum (Furlanetto et al., 2006; Pritchard & Loeb, 2012). The amplitude of this perturbation on a given line of sight is a function of the neutral fraction of hydrogen, the baryon overdensity, the spin temperature relative to the CMB temperature at the given redshift, and the line-of-sight peculiar velocity of the gas. The spatial power spectrum of this perturbation is thought to be dominated by inhomogeneous heating of the intergalactic medium (IGM) at  $z \sim 20$  (Fialkov et al., 2014), and by growing ionized bubbles during the epoch of reionization (EoR) at  $z \sim 7$ , where a detection can constrain the ionizing efficiency of early galaxies, the UV photon mean-free path, and the minimum halo mass that can support star formation (Greig & Mesinger, 2015).

Current 21 cm cosmology experiments can be broadly separated into two classes: global signal experiments that aim to detect the spectral signature of the cosmologically redshifted 21 cm transition after averaging over the entire sky (otherwise known as the monopole) and power spectrum experiments that incorporate angular information to attempt to measure the 3D spatial power spectrum of cosmological 21 cm perturbations. Ongoing global signal experiments include EDGES (Monsalve et al., 2017), LEDA (Price et al., 2018), BIGHORNS (Sokolowski et al., 2015), SCI-HI (Voytek et al., 2014), and SARAS 2 (Singh et al., 2017). Ongoing power spectrum experiments include PAPER/HERA (Ali et al., 2015; DeBoer et al., 2017), LOFAR (Patil et al., 2017), and the MWA (Beardsley et al., 2016; Ewall-Wice et al., 2016). Recently, EDGES reported the first detection of 21 cm absorption in the globally averaged sky signal (Bowman et al., 2018).

Just as for CMB experiments, foreground removal or suppression is an essential component of both classes of 21 cm cosmology experiments. The brightness temperature of the galactic synchrotron emission at high galactic latitudes is measured by Mozdzen et al. (2017) as

$$T \sim 300 \text{ K} \times \left( \frac{\nu}{150 \text{ MHz}} \right)^{-2.6}. \quad (3.1)$$

Therefore, experiments conservatively need to achieve five orders of dynamic range against this foreground emission before the cosmological signal can be measured. Current foreground removal methods (for example, Parsons et al. 2012 and Chapman et al. 2013) rely on the assumption that the foreground emission is spectrally

smooth. The low-frequency radio sky is composed of several components: galactic synchrotron emission, supernova remnants, radio galaxies, free-free emission and absorption from H II regions, and a confusing background of radio sources. Ideally, a foreground removal strategy should be informed by the measured spatial structure and frequency spectrum of all foreground components. For instance, CMB experiments typically construct several maps at several frequencies to enable component separation. At low frequencies, this possibility is limited by the availability of suitable high-fidelity sky maps on angular scales ranging from tens of degrees to arcminutes.

Recently, a host of new low-frequency sky surveys have been conducted, including MSSS (Heald et al., 2015), GLEAM (Wayth et al., 2015), and TGSS (Intema et al., 2017). However, the primary data product generated by these surveys is a catalog of radio point sources. At 45 MHz, Guzmán et al. (2011) created a map of the sky that captures the diffuse emission with  $5^\circ$  resolution. The LWA1 Low Frequency Sky Survey (LLFSS; Dowell et al., 2017) similarly maps the sky at a range of frequencies between 35 and 80 MHz with resolution between  $4.5^\circ$  and  $2^\circ$ .

The Global Sky Model (GSM; de Oliveira-Costa et al., 2008) is currently the most commonly used foreground model. The GSM is a nonparametric interpolation of various maps between 10 MHz and 100 GHz. However, the majority of information contained in the GSM is derived at frequencies  $> 1.4$  GHz, where the majority of the modern, high-fidelity input maps are located. At 408 MHz, the venerable Haslam map (Haslam et al., 1981, 1982) covers the entire sky at  $1^\circ$  resolution. Below 408 MHz, the GSM uses three input sky maps. Zheng et al. (2017a) constructed an improved GSM with five maps below 408 MHz, and Dowell et al. (2017) used the LWA1 to improve the GSM with their own sky maps. However, the GSM generally suffers from low angular resolution ( $\sim 5^\circ$ ) and systematic errors associated with instrumental artifacts in the input maps. For instance, Dowell et al. (2017) reported errors of  $\pm 50\%$  between the GSM and their own maps at 74 MHz, which they attribute to the increasing contribution of free-free absorption and modifications to the synchrotron spectral index at low frequencies.

Wide-field interferometric synthesis imaging is a challenging computational problem, and it has been particularly difficult to capture large angular scales  $\gg 10^\circ$  and small angular scales  $\ll 1^\circ$  in a single synthesis image. We will derive a new imaging technique – Tikhonov-regularized  $m$ -mode analysis imaging – that allows a drift-scanning interferometer to image the entire visible sky in a single coherent

synthesis imaging step with no gridding and no mosaicking.

As a demonstration of this technique, we apply Tikhonov-regularized  $m$ -mode analysis imaging to the Owens Valley Radio Observatory Long Wavelength Array (OVRO-LWA) and generate a series of new low-frequency maps of the sky between 36.528 and 73.152 MHz. These maps capture the full sky visible from OVRO with an angular resolution of  $\sim 15$  arcmin. These new maps complement the existing full-sky maps at these frequencies with greatly improved angular resolution.

We aim for these maps to inform foreground removal strategies in 21 cm cosmology, and we anticipate additional ancillary science taking advantage of the combination of high fidelity and high resolution of these maps, including but not limited to studies of the cosmic-ray emissivity at low frequencies, searches for giant radio galaxies, and constraining the galactic synchrotron spectrum. The maps will be made freely available online at the Legacy Archive for Microwave Background Data Analysis (LAMBDA)<sup>1</sup>.

The structure of this paper is as follows. In §3.2, we present Tikhonov-regularized  $m$ -mode analysis imaging, a new imaging technique that allows us to image the entire visible sky in one coherent synthesis imaging step with exact wide-field corrections. In §4.2 we describe our observations with the OVRO-LWA. In §4.6 we present the sky maps and compare these maps against other low-frequency sky maps. In §3.5, we discuss some of the sources of error present in the maps, and finally, in §4.7 we present our conclusions.

### 3.2 All-sky Imaging

The goal of all imaging algorithms is to estimate the brightness of the sky  $I_\nu(\hat{r})$  in the direction  $\hat{r}$  and frequency  $\nu$ . A radio interferometer measures the visibilities  $V_\nu^{ij,pq}$  between pairs of antennas numbered  $i$  and  $j$  respectively, and between polarizations labeled  $p$  and  $q$  respectively. We will neglect subtleties associated with polarized imaging, so the Stokes  $I$  visibilities are constructed from the sum of the  $pp$  and  $qq$  correlations such that  $V_\nu^{ij} = (V_\nu^{ij,pp} + V_\nu^{ij,qq})/2$ . If the antennas are separated by the baseline  $\vec{b}_{ij}$ , and  $A_\nu(\hat{r})$  describes an antenna's response to the incident Stokes  $I$  radiation (here assumed to be the same for each antenna), then

$$V_\nu^{ij} = \int_{\text{sky}} A_\nu(\hat{r}) I_\nu(\hat{r}) \exp\left(2\pi i \hat{r} \cdot \vec{b}_{ij}/\lambda\right) d\Omega, \quad (3.2)$$

---

<sup>1</sup> [https://lambda.gsfc.nasa.gov/product/foreground/fg\\_ovrolwa\\_radio\\_maps\\_info.cfm](https://lambda.gsfc.nasa.gov/product/foreground/fg_ovrolwa_radio_maps_info.cfm)

where the integral runs over the solid angle  $\Omega$ . Constructing an image from the output of a radio interferometer consists of estimating  $I_\nu(\hat{r})$  given the available measurements  $V_\nu^{ij}$ .

For later convenience, we will define the baseline transfer function  $B_\nu^{ij}(\hat{r})$  such that

$$V_\nu^{ij} = \int_{\text{sky}} B_\nu^{ij}(\hat{r}) I_\nu(\hat{r}) d\Omega. \quad (3.3)$$

The baseline transfer function defines the response of a single baseline to the sky and is a function of the antenna primary beam, and baseline length and orientation.

Naively, one might attempt to solve Equation 3.2 by discretizing and subsequently solving the resulting matrix equation. If the interferometer is composed of  $N_{\text{base}}$  baselines and measures  $N_{\text{freq}}$  frequency channels over  $N_{\text{time}}$  integrations, then the entire data set consists of  $N_{\text{base}}N_{\text{freq}}N_{\text{time}}$  complex numbers. If the sky is discretized into  $N_{\text{pix}}$  pixels, then the relevant matrix has dimensions of  $(N_{\text{base}}N_{\text{freq}}N_{\text{time}}) \times (N_{\text{pix}})$ . For making single-channel maps with the OVRO-LWA, this becomes a 5 PB array (assuming each matrix element is a 64 bit complex floating point number). This matrix equation is therefore prohibitively large, and solving Equation 3.2 by means of discretization is usually intractable, although Zheng et al. (2017b) demonstrated this technique with the MITEOR telescope.

Instead, it is common to make mild assumptions that simplify Equation 3.2 and ease the computational burden in solving for  $I_\nu(\hat{r})$ . For example, when all of the baselines  $\vec{b}_{ij}$  lie in a plane and the field of view is small, Equation 3.2 can be well approximated by a two-dimensional Fourier transform (Thompson et al., 2001). The restriction on baseline coplanarity and field of view can be relaxed by using W-projection (Cornwell et al., 2008). Known primary beam effects can also be accounted for during imaging by using A-projection (Bhatnagar et al., 2013).

### ***m*-mode Analysis**

Transit telescopes can take advantage of a symmetry in Equation 3.2 that greatly reduces the amount of computer time required to image the full sky with exact incorporation of wide-field imaging effects. This technique, called *m*-mode analysis, also obviates the need for gridding and mosaicking. Instead, the entire sky is imaged in one coherent synthesis imaging step. We will briefly summarize *m*-mode analysis below, but the interested reader should consult Shaw et al. (2014, 2015) for a complete derivation.

In the context of  $m$ -mode analysis, a transit telescope is any interferometer for which the response pattern of the individual elements does not change with respect to time. This may be an interferometer like the OVRO-LWA, where the correlation elements are fixed dipoles, but it may also be an interferometer like LOFAR or the MWA if the steerable beams are held in a fixed position (not necessarily at zenith). The interferometer also does not necessarily have to be homogeneous. Heterogeneous arrays composed of several different types of antennas are allowed as long as care is taken to generalize Equation 3.2 for a heterogeneous array.

For a transit telescope, the visibilities  $V_v^{ij}$  are a periodic function of sidereal time.<sup>2</sup> Therefore, it is a natural operation to compute the Fourier transform of the visibilities with respect to sidereal time  $\phi \in [0, 2\pi)$ .

$$V_{m,v}^{ij} = \int_0^{2\pi} V_v^{ij}(\phi) \exp(-im\phi) d\phi \quad (3.4)$$

The output of this Fourier transform is the set of  $m$ -modes  $V_{m,v}^{ij}$  where  $m = 0, \pm 1, \pm 2, \dots$  is the Fourier conjugate variable to the sidereal time. The  $m$ -mode corresponding to  $m = 0$  is a simple average of the visibilities over sidereal time. Similarly,  $m = 1$  corresponds to the component of the visibilities that varies over half-day timescales. Larger values of  $m$  correspond to components that vary on quicker timescales.

Shaw et al. (2014, 2015) showed that there is a discrete linear relationship between the measured  $m$ -modes  $V_{m,v}^{ij}$  and the spherical harmonic coefficients of the sky brightness  $a_{lm,v}$ .

$$V_{m,v}^{ij} = \sum_l B_{lm,v}^{ij} a_{lm,v}, \quad (3.5)$$

where the transfer coefficients  $B_{lm,v}^{ij}$  are computed from the spherical harmonic transform of the baseline transfer function defined by Equation 3.3. These transfer coefficients define the interferometer's response to the corresponding spherical harmonic coefficients.

Equation 3.5 can be recognized as a matrix equation, where the transfer matrix  $\mathbf{B}$  is

---

<sup>2</sup> This is not strictly true. Ionospheric fluctuations and non-sidereal sources (such as the Sun) will violate this assumption. This paper will, however, demonstrate that the impact on the final maps is mild.

block-diagonal:

$$\underbrace{\begin{pmatrix} \nu \\ \vdots \\ m\text{-modes} \\ \vdots \end{pmatrix}}_{\mathbf{v}} = \underbrace{\begin{pmatrix} & & \mathbf{B} \\ & \ddots & \\ & \text{transfer matrix} & \\ & & \ddots \end{pmatrix}}_{\mathbf{B}} \underbrace{\begin{pmatrix} a \\ \vdots \\ a_{lm} \\ \vdots \end{pmatrix}}_{\mathbf{a}} \quad (3.6)$$

$$\mathbf{B} = \begin{pmatrix} m=0 & & & \\ & m=\pm 1 & & \\ & & m=\pm 2 & \\ & & & \ddots \end{pmatrix} \quad (3.7)$$

The vector  $\mathbf{v}$  contains the list of  $m$ -modes and the vector  $\mathbf{a}$  contains the list of spherical harmonic coefficients representing the sky brightness. In order to take advantage of the block-diagonal structure in  $\mathbf{B}$ ,  $\mathbf{v}$  and  $\mathbf{a}$  must be sorted by the absolute value of  $m$ . Positive and negative values of  $m$  are grouped together because the brightness of the sky is real-valued, and the spherical harmonic transform of a real-valued function has  $a_{l(-m)} = (-1)^m a_{lm}^*$ .

In practice, we now need to pick the set of spherical harmonics we will use to represent the sky. For an interferometer like the OVRO-LWA with many short baselines, a sensible choice is to use all spherical harmonics with  $l \leq l_{\max}$  for some  $l_{\max}$ . The parameter  $l_{\max}$  is determined by the maximum baseline length of the interferometer. For an interferometer without short spacings, a minimum value for  $l$  might also be used. This  $l_{\min}$  parameter should be determined by the minimum baseline length. A rough estimate of  $l$  for a baseline of length  $b$  at frequency  $\nu$  is  $l \sim \pi b \nu / c$ . Based on this estimate for the OVRO-LWA and other computational considerations, we therefore adapt  $l_{\min} = 1$  and  $l_{\max} = 1000$  across all frequencies. However, this choice of  $l_{\max}$  actually limits the angular resolution above 55 MHz, and therefore future work will increase  $l_{\max}$  to obtain better angular resolution.

The interferometer's sensitivity to the monopole ( $a_{00}$ ) deserves special consideration. Venumadhav et al. (2016) proveed – under fairly general assumptions – that a baseline with nonzero sensitivity to  $a_{00}$  must also have some amount of cross-talk or common-mode noise. In fact, the sensitivity to  $a_{00}$  is proportional to a sum of these effects. For example, one way a baseline can have nonzero sensitivity to  $a_{00}$  is if the baseline is extremely short. In this case, the antennas are so close together that voltage fluctuations in one antenna can couple into the other antenna. In order to make an interferometric measurement of  $a_{00}$ , this coupling must be measured

and calibrated. Consequently, we set  $a_{00} = 0$  in our analysis. In the future, this limitation will be addressed with the inclusion of calibrated total power radiometry.

The size of a typical block in the transfer matrix is  $(2N_{\text{base}}N_{\text{freq}}) \times (l_{\max})$ . If each element of the matrix is stored as a 64 bit complex floating point number, a single block is 500 MB for the case of single-channel imaging with the OVRO-LWA, which a modern computer can easily store and manipulate in memory. However, with additional bandwidth, these blocks quickly become unwieldy; thus, as a first pass, the analysis in this paper is restricted to single-channel imaging. Note also that for the OVRO-LWA,  $N_{\text{base}} \gg l_{\max}$ , so there are more measurements than unknowns in Equation 3.6.

The key advantage of  $m$ -mode analysis is the block-diagonal structure of Equation 3.6. The computational complexity of many common matrix operations (e.g., solving a linear system of equations) is  $\mathcal{O}(N^3)$ , where  $N$  is the linear size of the matrix. By splitting the equation into  $M$  independent blocks, the number of floating point operations required to solve the linear system of equations is now  $\mathcal{O}(N^3 M^{-2})$ , because each block can be manipulated independently of the other blocks. This computational savings is what makes this matrix algebra approach to interferometric imaging feasible. For the data set presented in this paper, computing the elements of the transfer matrix takes  $\sim 10$  hours per frequency channel on a 10-node cluster, but once the matrix has been computed, the imaging process described in §3.2 takes  $\sim 10$  minutes, and the deconvolution process described in §3.2 was allowed to run for  $\sim 10$  hours.

### ***m*-mode Analysis Imaging**

Imaging in  $m$ -mode analysis essentially amounts to inverting Equation 3.6 to solve for the spherical harmonic coefficients  $\mathbf{a}$ . The linear least-squares solution, which minimizes  $\|\mathbf{v} - \mathbf{B}\mathbf{a}\|^2$ , is given by

$$\hat{\mathbf{a}}_{\text{LLS}} = (\mathbf{B}^* \mathbf{B})^{-1} \mathbf{B}^* \mathbf{v}, \quad (3.8)$$

where  $*$  indicates the conjugate-transpose.

However, usually one will find that  $\mathbf{B}$  is not full rank, and hence  $\mathbf{B}^* \mathbf{B}$  is not an invertible matrix. For example, an interferometer located in the northern hemisphere will never see a region of the southern sky centered on the southern celestial pole. The  $m$ -modes contained in the vector  $\mathbf{v}$  must contain no information about the sky around the southern celestial pole, and therefore the act of multiplying by  $\mathbf{B}$  must

destroy some information about the sky. The consequence of this fact is that  $\mathbf{B}$  must have at least one singular value that is equal to zero. It then follows that  $\mathbf{B}^*\mathbf{B}$  must have at least one eigenvalue that is equal to zero, which means it is not an invertible matrix.

Another way of looking at the problem is that because the interferometer is not sensitive to part of the southern hemisphere, there are infinitely many possible solutions to Equation 3.6 that will fit the measured data equally well. We will therefore regularize the problem and apply an additional constraint that prefers a unique yet physically reasonable solution.

### Tikhonov Regularization

The process of Tikhonov regularization minimizes  $\|\mathbf{v} - \mathbf{B}\mathbf{a}\|^2 + \varepsilon\|\mathbf{a}\|^2$  for some arbitrary value of  $\varepsilon > 0$  chosen by the observer. The solution that minimizes this expression is given by

$$\hat{\mathbf{a}}_{\text{Tikhonov}} = (\mathbf{B}^*\mathbf{B} + \varepsilon\mathbf{I})^{-1}\mathbf{B}^*\mathbf{v}. \quad (3.9)$$

Tikhonov regularization adds a small value  $\varepsilon$  to the diagonal of  $\mathbf{B}^*\mathbf{B}$ , fixing the matrix's singularity. By using the singular value decomposition (SVD) of the matrix  $\mathbf{B} = \mathbf{U}\Sigma\mathbf{V}^*$ , Equation 3.9 becomes

$$\hat{\mathbf{a}}_{\text{Tikhonov}} = \mathbf{V}(\Sigma^2 + \varepsilon\mathbf{I})^{-1}\Sigma\mathbf{U}^*\mathbf{v}, \quad (3.10)$$

where

$$\Sigma = \begin{pmatrix} \sigma_1 & & \\ & \sigma_2 & \\ & & \ddots \end{pmatrix}.$$

The diagonal elements of  $\Sigma$  are the singular values of  $\mathbf{B}$ . The contribution of each singular component to the Tikhonov-regularized solution is scaled by  $\sigma_i/(\sigma_i^2 + \varepsilon)$ , where  $\sigma_i$  is the singular value for the  $i$ th singular component. Tikhonov regularization therefore acts to suppress any component for which  $\sigma_i \lesssim \sqrt{\varepsilon}$ . If  $\sigma_i = 0$ , the component is set to zero.

In practice, the measurement  $\mathbf{v}$  is corrupted by noise with covariance  $\mathbf{N}$ . For illustrative purposes, we will assume that  $\mathbf{N} = n\mathbf{I}$  for some  $n > 0$ . In this case, the covariance of the Tikhonov-regularized spherical harmonic coefficients is

$$\mathbf{C} = n\mathbf{V}(\Sigma^2 + \varepsilon\mathbf{I})^{-2}\Sigma^2\mathbf{V}^*. \quad (3.11)$$

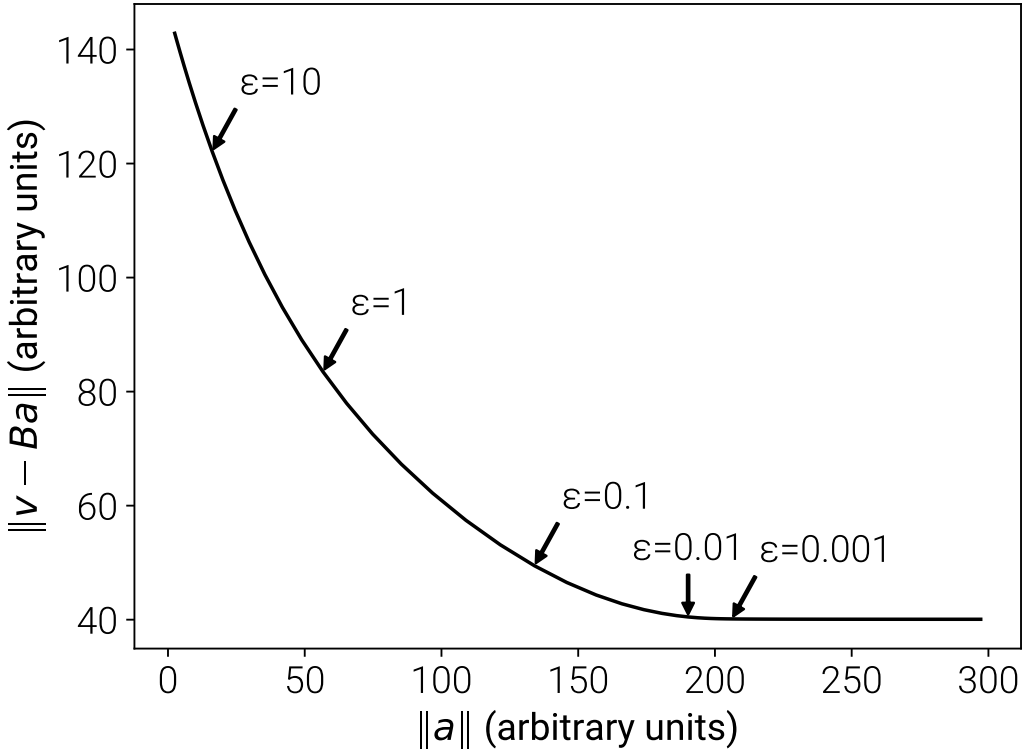


Figure 3.1: Example L curve computed from OVRO-LWA data at 36.528 MHz by trialing 200 different values of the regularization parameter  $\epsilon$ . The  $x$ -axis is the norm of the solution (in this case, the spherical harmonic coefficients) given in arbitrary units, and the  $y$ -axis is the least-squares norm given in arbitrary units. Where the regularization parameter is small, the norm of the solution grows rapidly. Where the regularization parameter is large, the least-squares norm grows rapidly.

Each singular component is scaled by a factor of  $\sigma_i^2 / (\sigma_i^2 + \epsilon)^2$ . In the absence of Tikhonov regularization ( $\epsilon = 0$ ), singular components with the smallest singular values – the ones that the interferometer is the least sensitive to – actually come to dominate the covariance of the measured spherical harmonic coefficients. Tikhonov regularization improves this situation by down-weighting these components.

## L Curves

Tikhonov regularization requires the observer to pick the value of  $\epsilon$ . If  $\epsilon$  is too large, then too much importance is placed on minimizing the norm of the solution and the least-squares residuals will suffer. Conversely, if  $\epsilon$  is too small, then the problem will be poorly regularized and the resulting sky map may not represent the true sky. Picking the value of  $\epsilon$  therefore requires understanding the trade-off between the

two norms.

This trade-off can be analyzed quantitatively by trialing several values of  $\varepsilon$ , and computing  $\|\mathbf{v} - \mathbf{B}\mathbf{a}\|^2$  and  $\|\mathbf{a}\|^2$  for each trial. An example is shown in Figure 3.1. The shape of this curve has a characteristic L shape, and as a result, this type of plot is called an L curve. The ideal value of  $\varepsilon$  lies near the turning point, of the plot. At this point a small decrease in  $\varepsilon$  will lead to an undesired rapid increase in  $\|\mathbf{a}\|^2$ , and a small increase in  $\varepsilon$  will lead to an undesired rapid increase in  $\|\mathbf{v} - \mathbf{B}\mathbf{a}\|^2$ .

In practice, the L curve should be used as a guide to estimate a reasonable value of  $\varepsilon$ . However, better results can often be obtained by tuning the value of  $\varepsilon$ . For instance, increasing the value of  $\varepsilon$  can improve the noise properties of the map by down-weighting noisy modes. Decreasing the value of  $\varepsilon$  can improve the resolution of the map by up-weighting the contribution of longer baselines, which are likely fewer in number. In this respect, choosing the value of  $\varepsilon$  is analogous to picking the weighting scheme in traditional imaging where robust weighting schemes can be tuned to similar effect (Briggs, 1995). For the OVRO-LWA, we selected  $\varepsilon = 0.01$  across all frequency channels. The distribution of singular values of the transfer matrix with respect to  $\sqrt{\varepsilon}$  is summarized in Table 3.1.

### Other Regularization Schemes

The choice of applying Tikhonov regularization to  $m$ -mode analysis imaging is not unique. There exists a plethora of alternative regularization schemes that could also be applied. Each regularization scheme has its own advantages and disadvantages. For instance, Tikhonov regularization is simple, independent of prior information, and sets unmeasured modes to zero (a sensible expectation). We will now briefly discuss a few other alternatives.

The Moore–Penrose pseudo-inverse (denoted with a superscript  $\dagger$ ) is commonly applied to find the minimum-norm linear least-squares solution to a set of linear equations. This can be used in place of Tikhonov regularization as

$$\hat{\mathbf{a}}_{\text{Moore-Penrose}} = \mathbf{B}^\dagger \mathbf{v}. \quad (3.12)$$

Much like Tikhonov regularization, the Moore–Penrose pseudo-inverse sets components with small singular values (below some user-defined threshold) to zero. Components with large singular values (above the user-defined threshold) are included in the calculation at their full amplitude with no down-weighting of modes near the threshold. The essential difference between using the Moore–Penrose

pseudo-inverse and Tikhonov regularization is that the pseudo-inverse defines a hard transition from “on” to “off.” Modes are either set to zero or included in the map at their full amplitude. On the other hand, Tikhonov regularization smoothly interpolates between these behaviors. Because of this, Tikhonov regularization tends to produce better results in practical applications.

If the measured  $m$ -modes have a noise covariance matrix  $\mathbf{N} \neq n\mathbf{I}$  for some scalar  $n$  (e.g., the interferometer is inhomogeneous), then the observer should minimize  $(\mathbf{v} - \mathbf{B}\mathbf{a})^*\mathbf{N}^{-1}(\mathbf{v} - \mathbf{B}\mathbf{a}) + \varepsilon\|\mathbf{a}\|^2$ . The noise covariance matrix  $\mathbf{N}$  is used to weight the measurements such that

$$\hat{\mathbf{a}}_{\text{min variance}} = (\mathbf{B}^*\mathbf{N}^{-1}\mathbf{B} + \varepsilon\mathbf{I})^{-1}\mathbf{B}\mathbf{N}^{-1}\mathbf{v}. \quad (3.13)$$

In the event that the observer has a prior map of the sky,  $\|\mathbf{a} - \mathbf{a}_{\text{prior}}\|^2$  can be used as the regularizing norm. This will use the prior map to fill in missing information instead of setting these modes to zero. In this case, the minimum is at

$$\hat{\mathbf{a}}_{\text{with prior}} = (\mathbf{B}^*\mathbf{B} + \varepsilon\mathbf{I})^{-1}(\mathbf{B}^*(\mathbf{v} - \mathbf{B}\mathbf{a}_{\text{prior}})) + \mathbf{a}_{\text{prior}}. \quad (3.14)$$

If instead the observer has a prior expectation on the covariance of the spherical harmonic coefficients, Wiener filtering can also be used. This technique is demonstrated for simulated measurements by Berger et al. (2016).

Alternatively, we could opt to regularize the problem by enforcing smoothness in the sky maps. In this case, the regularizing norm should be of the form  $\|\nabla I(\hat{r})\|^2$ , where  $\nabla I$  is the gradient of the sky brightness in the direction  $\hat{r}$ . This is actually a generalization of Tikhonov regularization, where the objective function is  $\|\mathbf{v} - \mathbf{B}\mathbf{a}\|^2 + \varepsilon\|\mathbf{A}\mathbf{a}\|^2$  for some matrix  $\mathbf{A}$ . The minimum is at

$$\hat{\mathbf{a}}_{\text{generalized}} = (\mathbf{B}^*\mathbf{B} + \varepsilon\mathbf{A}^*\mathbf{A})^{-1}\mathbf{B}^*\mathbf{v}. \quad (3.15)$$

Finally, in many machine-learning applications the  $L_1$ -norm<sup>3</sup> is used in place of the usual  $L_2$ -norm in order to encourage sparsity in the reconstructed signal. Applying this to  $m$ -mode analysis imaging would amount to minimizing  $\|\mathbf{v} - \mathbf{B}\mathbf{a}\|_2^2 + \varepsilon\|\mathbf{a}\|_1$ . However, because we have decomposed the sky in terms of spherical harmonics, the vector  $\mathbf{a}$  is not expected to be sparse. Consequently, the  $L_1$ -norm is generally inappropriate for  $m$ -mode analysis imaging without an additional change of variables designed to introduce sparsity.

---

<sup>3</sup>  $\|\mathbf{a}\|_1 = \sum_i |a_i|$

## CLEAN

In traditional radio astronomy imaging, CLEAN (Högbom, 1974) is a physically motivated algorithm that interpolates between measured visibilities on the  $uv$  plane. In the absence of this interpolation, gaps in the interferometer's  $uv$  coverage are assumed to be zero, and – in the image plane – sources are convolved with a point spread function (PSF) that is characteristic of the  $uv$  coverage. Fundamentally, the interferometer's PSF is determined by which modes were assumed to be zero in the initial imaging process.

In  $m$ -mode analysis imaging, we assumed modes were zero in two separate ways.

1. We selected a set of spherical harmonic coefficients  $a_{lm}$  to describe the sky-brightness distribution. All modes with  $l > l_{\max}$  are neglected and assumed to be zero.
2. Tikhonov regularization forces linear combinations of spherical harmonic coefficients with  $\sigma_i \lesssim \sqrt{\varepsilon}$  toward zero.

As a consequence, the final map of the sky is not assembled from a complete set of spherical harmonics. Therefore, just as in traditional imaging,  $m$ -mode analysis imaging produces dirty maps in which sources are convolved with a PSF. This PSF can be improved by increasing the number and variety of baselines, which increases the number of modes for which  $\sigma_i \gg \sqrt{\varepsilon}$ . Alternatively, by collecting more data, the signal-to-noise ratio of the measured  $m$ -modes increases, which allows the observer to lower the value of  $\varepsilon$  without increasing the noise in the maps. Finally, the CLEAN algorithm can be applied to interpolate some of the missing information that was assumed to be zero.

The PSF of a dirty  $m$ -mode analysis map may be computed with

$$\mathbf{a}_{\text{PSF}}(\theta, \phi) = (\mathbf{B}^* \mathbf{B} + \varepsilon \mathbf{I})^{-1} \mathbf{B}^* \mathbf{B} \mathbf{a}_{\text{PS}}(\theta, \phi), \quad (3.16)$$

where  $\mathbf{a}_{\text{PSF}}(\theta, \phi)$  is the vector of spherical harmonic coefficients representing the PSF at the spherical coordinates  $(\theta, \phi)$ , and  $\mathbf{a}_{\text{PS}}(\theta, \phi)$  is the vector of spherical harmonic coefficients for a point source at  $(\theta, \phi)$  given by

$$\mathbf{a}_{\text{PS}}(\theta, \phi) = \begin{pmatrix} \vdots \\ Y_{lm}^*(\theta, \phi) \\ \vdots \end{pmatrix} = \begin{pmatrix} \vdots \\ Y_{lm}^*(\theta, 0) \times e^{im\phi} \\ \vdots \end{pmatrix}. \quad (3.17)$$

In general, the PSF can be a function of the right ascension and declination. However, point sources at the same declination take the same track through the sky and (barring any ionospheric effects) will have the same PSF. The PSF is therefore only a function of the declination. For example, sources at low elevations will tend to have an extended PSF along the north–south axis due to baseline foreshortening. For the OVRO-LWA antenna configuration (Figure 3.2), example PSFs at three separate frequencies are shown in Figure 3.3. Adapting CLEAN for  $m$ -mode analysis requires either precomputing Equation 3.16 at a grid of declinations, or a method for rapidly evaluating Equation 3.16 on the fly.

For an interferometer with more baselines than spherical harmonics used in the maps (e.g., the OVRO-LWA),  $\mathbf{B}^* \mathbf{B}$  can be a much smaller matrix than the full transfer matrix  $\mathbf{B}$ . Therefore, precomputing  $\mathbf{B}^* \mathbf{B}$  can allow the entire matrix to fit into memory on a single machine. This greatly reduces the amount of disk I/O necessary for solving Equation 3.16.

Additionally, we can precompute the Cholesky decomposition of  $\mathbf{B}^*\mathbf{B} + \varepsilon\mathbf{I} = \mathbf{U}^*\mathbf{U}$ , where  $\mathbf{U}$  is an upper triangular matrix. Inverting an upper triangular matrix is an  $O(N^2)$  operation (instead of  $O(N^3)$  for a general matrix inverse).<sup>4</sup> Equation 3.16 can then be rapidly evaluated from right to left as

$$\boldsymbol{a}_{\text{PSF}} = \boldsymbol{U}^{-1} (\boldsymbol{U}^*)^{-1} (\boldsymbol{B}^* \boldsymbol{B}) \boldsymbol{a}_{\text{PS}}. \quad (3.18)$$

Furthermore, Equation 3.18 does not need to be separately evaluated for each CLEAN component. Instead, we can identify  $N$  CLEAN components, accumulate  $\mathbf{a}_{\text{PS}}$  for each component, and evaluate Equation 3.18 on the accumulation. This can greatly reduce the number of times this equation needs to be evaluated, but care must be taken to ensure that the  $N$  components are not so close together that sidelobes from one may interact with another.

Altogether, the adaptation of CLEAN applied to the maps presented in this paper is summarized below.

**Precondition:**  $a$  is the solution to Equation 3.9

- ```

1: function CLEAN( $a$ )
2:    $M \leftarrow B^*B$ 
3:    $U \leftarrow chol(M + \varepsilon I)$                                 ▷ Cholesky decomposition
4:   while noise in map > threshold do

```

<sup>4</sup> Instead of computing  $\mathbf{A}^{-1}$ , we solve the linear equation  $\mathbf{Ax} = \mathbf{b}$  each time the matrix inverse is needed so as to avoid numerical instabilities.

```

5:    find  $N$  pixels with the largest residual flux
6:     $\mathbf{x} \leftarrow \sum_{i=1}^N$  (pixel flux)  $\times \mathbf{a}_{\text{PS}}(\theta_i, \phi_i)$ 
7:     $\mathbf{y} \leftarrow \mathbf{U}^{-1}(\mathbf{U}^*)^{-1} \mathbf{Mx}$ 
8:     $\mathbf{a} \leftarrow \mathbf{a} - (\text{loop gain}) \times \mathbf{y}$ 
9:    record subtracted components
10:    $\mathbf{a} \leftarrow \mathbf{a} + (\text{restored components})$ 
11:   return  $\mathbf{a}$ 

```

In summary, Tikhonov-regularized  $m$ -mode analysis imaging constructs a wide-field synthesis image of the sky from a complete Earth rotation, and with exact treatment of wide-field effects. This is accomplished by solving a regularized block-diagonal matrix equation (Equation 3.9). The solution to this equation generates a map where sources are convolved with a PSF characteristic of the interferometer (a function of the frequency, antenna response, and baseline distribution with a full Earth rotation). The CLEAN algorithm is adopted to deconvolve the PSF and produce the final sky maps.

### 3.3 Observations

#### The OVRO-LWA

The OVRO-LWA is a 288-element interferometer located at OVRO near Big Pine, California (Hallinan et al., in prep.). The OVRO-LWA is a low-frequency instrument with instantaneous bandwidth covering 27 to 85 MHz and with 24 kHz channelization. Each antenna stand hosts two perpendicular broadband dipoles so that there are  $288 \times 2$  signal paths in total. These signal paths feed into the 512-input LEDA correlator (Kocz et al., 2015), which allows the OVRO-LWA to capture the entire visible hemisphere in a single snapshot image.

The 288 antennas are arranged in a pseudo-random configuration optimized to minimize sidelobes in snapshot imaging (see Figure 3.2). Of these 288 antennas, 251 are contained within a 200 m diameter core, 32 are placed outside of the core in order to extend the maximum baseline length to  $\sim 1.5$  km, and five are equipped with noise-switched front ends for calibrated total power measurements of the global sky brightness. These antennas are used as part of the LEDA experiment (Price et al., 2018) to measure the global signal of 21 cm absorption from the cosmic dawn. In the current configuration, 32 antennas (64 signal paths) from the core are disconnected from the correlator in order to accommodate the 32 antennas on longer baselines. A final stage of construction will involve 64 additional antennas installed on long

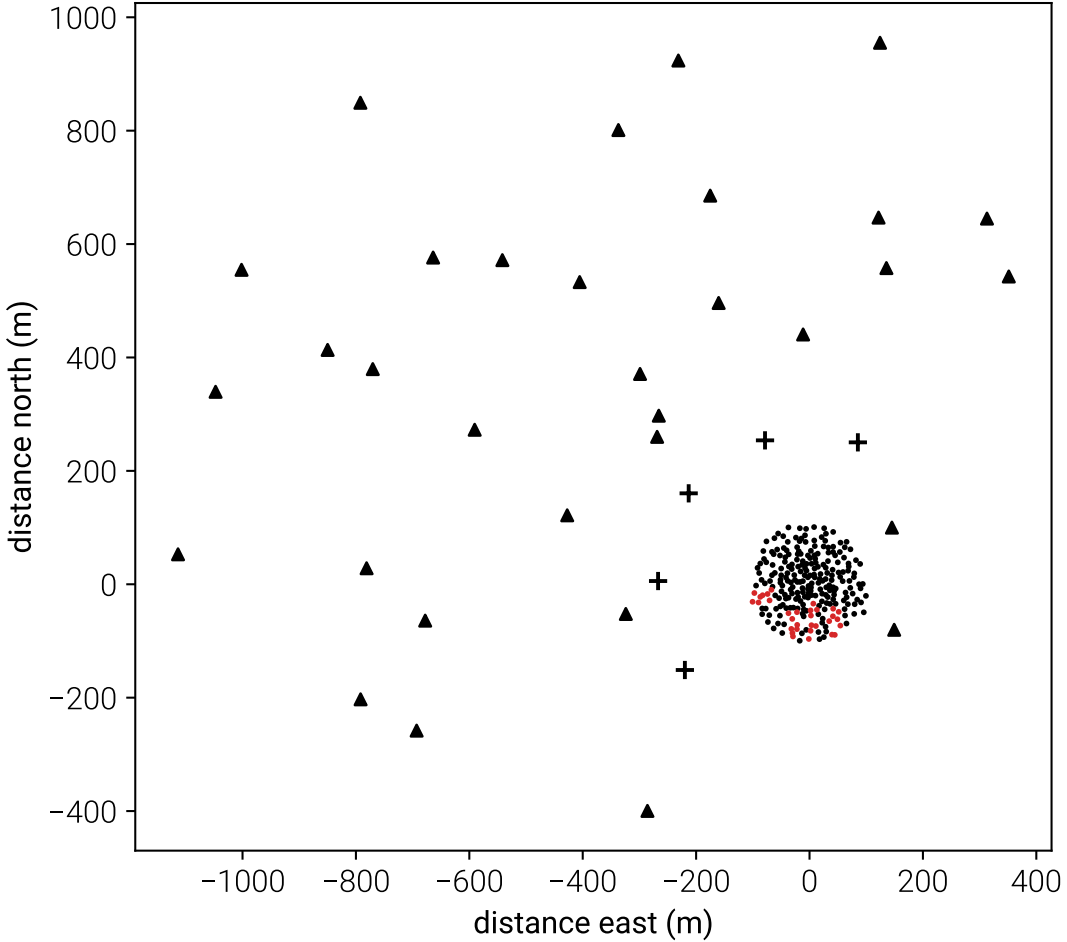


Figure 3.2: Antenna layout for the OVRO-LWA. Black dots correspond to antennas within the 200 m diameter core of the array. The 32 triangles are the expansion antennas built in early 2016 in order to increase the longest baseline to  $\sim 1.5$  km. The red dots are core antennas that are disconnected from the correlator in order to accommodate these antennas. The five crosses are antennas equipped with noise-switched front ends.

baselines out to a maximum length of 2.6 km.

The data set used in this paper spans 28 consecutive hours beginning at 2017 February 17 12:00:00 UTC time. During this time, the OVRO-LWA operated as a zenith-pointing drift-scanning interferometer. The correlator dump time was selected to be 13 s such that the correlator output evenly divides a sidereal day. Due to the computational considerations presented in §3.2, eight 24 kHz channels are selected for imaging from this data set: 36.528, 41.760, 46.992, 52.224, 57.456, 62.688, 67.920, and 73.152 MHz. These particular channels are chosen due to their location at the exact center of instrumental subbands.

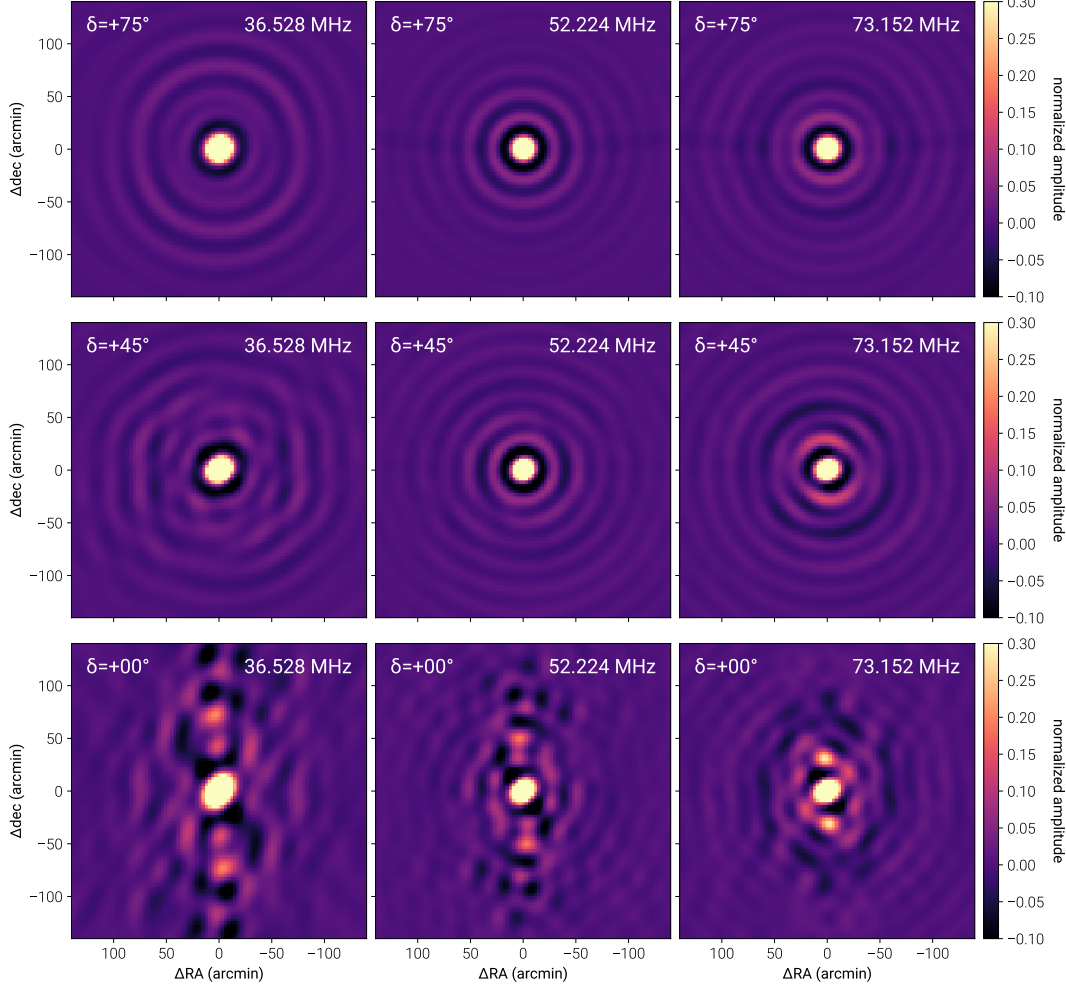


Figure 3.3: The  $m$ -mode analysis imaging PSF at three declinations (top row:  $\delta = +75^\circ$ , middle row:  $\delta = +45^\circ$ , bottom row:  $\delta = +0^\circ$ ) and three frequencies (left column: 36.528 MHz, middle column: 52.224 MHz, right column: 73.152 MHz). The PSF is computed by evaluating Equation 3.16. Above 55 MHz, the angular extent of the PSF does not follow the expected scaling with frequency because the angular resolution is limited by the selection of  $l_{\max} = 1000$ . The FWHM at  $\delta = +45^\circ$  is listed in Table 3.1.

### Complex Gain Calibration

The complex gain calibration is responsible for correcting per-antenna amplitude and phase errors. This is accomplished using a sky model and a variant of alternating least-squares colloquially known as “Stefcal” (Mitchell et al., 2008; Salvini & Wijnholds, 2014)<sup>5</sup>.

---

<sup>5</sup> The calibration routine is written in the Julia programming language (Bezanson et al., 2017), and is publicly available online (<https://github.com/mweastwood/TTCal.jl>) under an open source license (GPLv3 or any later version).

Cyg A and Cas A are – by an order of magnitude – the brightest point-like radio sources in the northern hemisphere at resolutions lower than  $0.25^\circ$ . Therefore, the optimal time to solve for the interferometer’s gain calibration is when these sources are at high elevations. The antenna complex gains are measured from a 22 minute track of data when Cyg A and Cas A are at high elevations. The gains measured in this way are then used to calibrate the entire 28 hour data set. The calibration sky model consists only of Cyg A and Cas A. The model flux of Cyg A is set to the Baars et al. (1977) spectrum, while the flux of Cas A is measured from the data itself (using a preliminary calibration solved for with a fiducial Cas A spectrum).

Calibrating in this manner generates approximately arcminute errors in the astrometry of the final sky maps due to ionospheric refractive offsets during the time of calibration. These residual errors in the astrometry are corrected post-imaging by registering the images with respect to all Very Large Array Low-frequency Sky Survey Redux (VLSSr) (Lane et al., 2014) sources that are bright ( $> 30$  Jy with a consistent flux density measured with the OVRO-LWA) and not too close to other bright sources (at least  $1^\circ$  separation).

Temperature fluctuations of the analog electronics generate 0.1 dB sawtooth oscillations in the analog gain. These oscillations occur with a variable 15 to 17 minute period associated with HVAC cooling cycles within the electronics shelter that houses these electronics. The amplitude of these gain fluctuations is calibrated by smoothing the autocorrelation amplitudes on 45 minute timescales. The ratio of the measured autocorrelation power to the smoothed autocorrelation power defines a per-antenna amplitude correction that is then applied to the cross-correlations. Additionally, the ambient temperature at the front-end electronics (located in a box at the top of each dipole) fluctuates diurnally, which will generate diurnal gain fluctuations. At this time, no correction is made for these diurnal gain fluctuations.

### **Primary Beam Measurements**

In order to generate wide-field images of the sky, the response of the antenna to the sky must be known. Drift-scanning interferometers like the OVRO-LWA can empirically measure their primary beam under a mild set of symmetry assumptions (Pober et al., 2012). The symmetry assumptions are necessary to break the degeneracy between source flux and beam amplitude when the flux of the source is unknown. In this work, we assume symmetries that are apparent in the antenna design, but real-world defects and coupling with nearby antennas will contribute

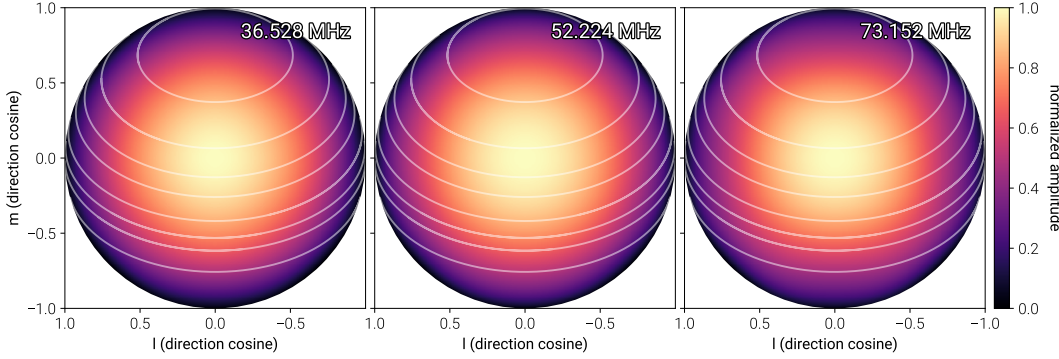


Figure 3.4: Empirical fits to the OVRO-LWA Stokes  $I$  primary beam (the response of the  $x$  and  $y$  dipoles has been summed) at three frequencies: 36.528 MHz (left panel), 52.224 MHz (middle panel), and 73.152 MHz (right panel). The source tracks used to measure the beam model are overlaid. From north to south, these tracks correspond to Cas A, Cyg A, 3C 123, Tau A, Vir A, Her A, 3C 353, and Hya A. The fitting process is described in §3.3, and residuals for Cyg A and Cas A are in Figure 3.5.

toward breaking these symmetries at some level. In particular, we assume that the  $x$  and  $y$  dipoles have the same response to the sky after rotating one by  $90^\circ$ , and that the beam is invariant under north–south and east–west flips.

We measure the flux of several bright sources (Cyg A, Cas A, Tau A, Vir A, Her A, Hya A, 3C 123, and 3C 353) as they pass through the sky and then fit a beam model composed of Zernike polynomials to those flux measurements. We select the basis functions to have the desired symmetry ( $Z_0^0, Z_2^0, Z_4^0, Z_4^4, Z_6^0, Z_6^4, Z_8^0, Z_8^4$ , and  $Z_8^8$ ), and the beam amplitude at zenith is constrained to be unity. See Figure 3.4 for an illustration of a fitted beam model at several frequencies. This process is repeated for each frequency channel. Residuals for Cyg A and Cas A can be seen in Figure 3.5.

### **Ionospheric Conditions**

The geomagnetic conditions during this time were mild. The Disturbance storm time (Dst) index, which measures the  $z$ -component of the interplanetary magnetic field, was  $> -30$  nT during the entirety of the observing period.<sup>6</sup> Following the classification scheme of Kintner et al. (2008), a weak geomagnetic storm has  $\text{Dst} < -30$  nT. Stronger geomagnetic storms have  $\text{Dst} < -50$  nT.

Despite the mild conditions, low-frequency interferometric observations are still affected by the index of refraction in the ionosphere. Figure 3.6 shows the median

---

<sup>6</sup> The Dst index was obtained from the World Data Center for Geomagnetism, Kyoto University (<http://swdcwww.kugi.kyoto-u.ac.jp/>). Accessed 2017 July 25.

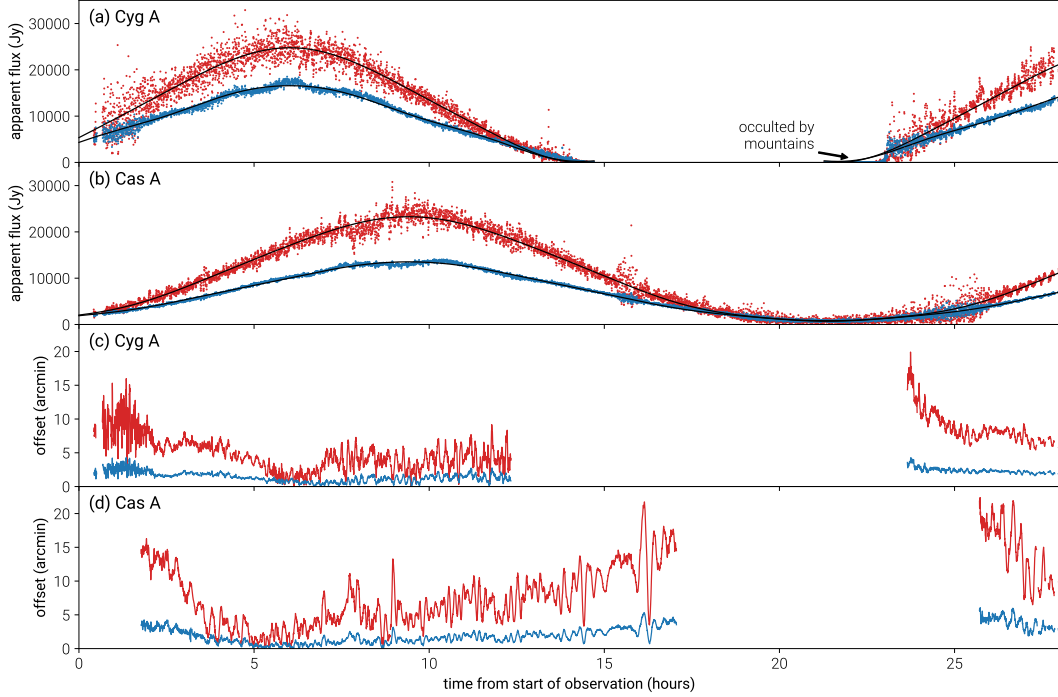


Figure 3.5: Panels (a) and (b) show the measured apparent flux of Cyg A and Cas A at 36.528 MHz (red points) and 73.152 MHz (blue points) as a function of time over the observing period. The solid black curves show the expected flux computed using the empirical beam model fits. The thermal noise contribution to each point is about 50 Jy. Cyg A is occulted by the White Mountains when it is low on the horizon to the east. Panels (c) and (d) show the measured position offset of Cyg A and Cas A relative to their true astronomical positions at 36.528 MHz (red line) and 73.152 MHz (blue line).

vertical total electron content (TEC) above OVRO measured from GPS (Iijima et al., 1999). The median is computed over all GPS measurements within 200 km of the observatory. Over the observing period, the TEC smoothly varies from 20 TECU at midday to 5 TECU during the night. However, this measurement is only sensitive to large-scale fluctuations in the ionosphere and does not capture small-scale fluctuations.

Small-scale fluctuations are best characterized by source scintillation and refractive offsets. Figure 3.5 shows the apparent flux and position offset of Cyg A and Cas A as a function of time over the entire observing period. Both sources exhibit rapid scintillation on the timescale of a single integration (13 s). For example, at 36.528 MHz, it is not unusual for Cyg A to have measured flux variations of 50% between adjacent 13 second integrations. The variance at 36.528 MHz compared with the variance at 73.152 MHz is consistent with an ionospheric  $v^{-2}$  origin. The

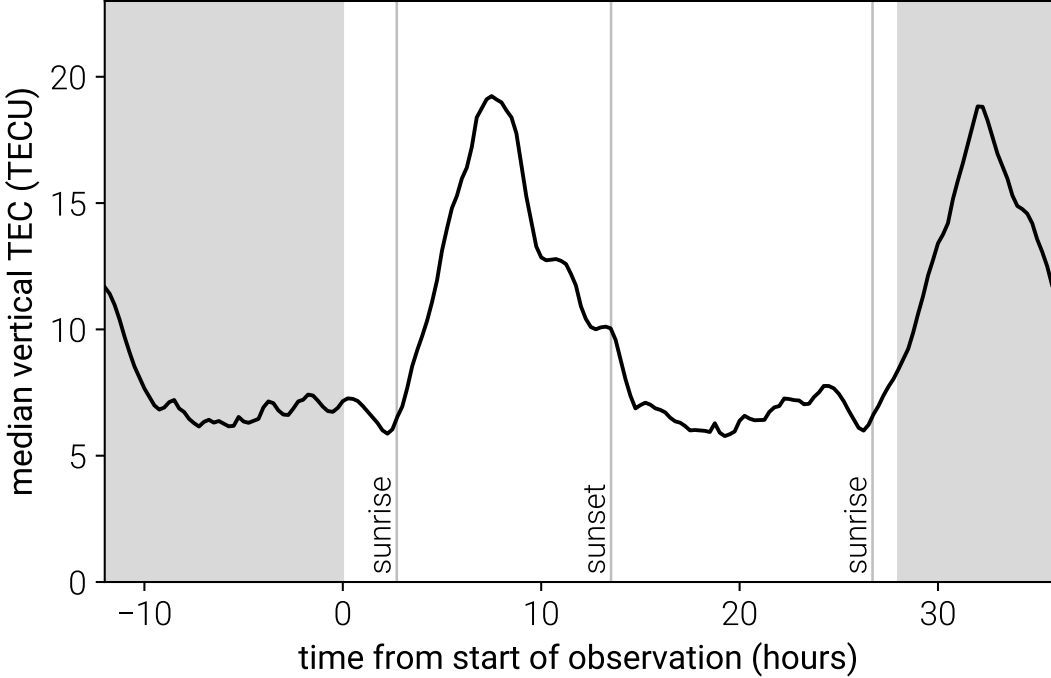


Figure 3.6: Median vertical TEC within 200 km of OVRO during the time of the observation. The gray shaded regions indicate times outside of the observing period. The gray vertical lines indicate sunrise and sunset (as labeled).

measured position offset of each source is a measurement of the ionospheric phase gradient across the array. This varies on slower 10 minute timescales, with each source refracting by as much as 20' (at 36.528 MHz) from its true astronomical position as waves in the ionosphere pass through the line of sight. At 74 MHz on the VLA, Kassim et al. (2007) observed  $\sim 1'$  refractive offsets during the night, and  $\sim 4'$  offsets during the day on similar  $\sim 10$  minute timescales, which is consistent with what is seen here. The impact of these effects on the sky maps is simulated in §3.5.

## Source Removal

### Cyg A and Cas A

Due to the rapid and large ionospheric fluctuations seen in Figure 3.5, CLEAN cannot be relied on to accurately deconvolve bright sources. However, without removing bright sources from the data, sidelobes from these sources will dominate the variance in the sky maps. At 74 MHz, Cyg A is a 15,000 Jy source (Baars et al., 1977). A conservative estimate for the confusion limit at 74 MHz with a 15' beam is 1000 mJy (Lane et al., 2014). Therefore, we require that Cyg A's sidelobes be at

least  $-45$  dB down from the main lobe to prevent Cyg A’s sidelobes from dominating the variance in the image.

To achieve this dynamic range at low frequencies, it is important to account for propagation effects through the ionosphere. In the weak scattering regime ( $r_{\text{diff}} \gg r_f$ , where  $r_{\text{diff}}$  is the diffractive scale of the ionosphere,  $r_f = \sqrt{\lambda D / 2\pi}$  is the Fresnel scale,  $\lambda$  is the wavelength, and  $D$  is the distance to the ionosphere), fluctuations within the ionosphere contribute amplitude and phase scintillations that can be described by a direction-dependent complex gain calibration. This justifies the use of “peeling,” which incorporates a direction-dependent calibration to subtract sources in the presence of ionospheric scintillation (e.g., Mitchell et al., 2008; Smirnov & Tasse, 2015).

In the strong scattering regime ( $r_{\text{diff}} \lesssim r_f$ ), the image of a point source can “break apart” into multiple images or speckles (Vedantham & Koopmans, 2015). Attempting to peel a source in the strong scattering regime will lead to source-subtraction artifacts in the final sky map. Mevius et al. (2016) measured that from the location of LOFAR at 150 MHz, the diffractive scale of the ionosphere is  $> 5$  km 90% of the time. This implies that at 73 MHz, the diffractive scale is typically  $> 2$  km, and at 36 MHz, the diffractive scale is typically  $> 1$  km. These limits are comparable to the Fresnel scale for the OVRO-LWA (i.e.,  $r_{\text{diff}} > r_f$ ), and therefore we do not generally expect to see strong scattering from the ionosphere. Ionospheric conditions during the observing period were mild (see §3.3). However, we do observe scintillation and refractive-offset events on the timescale of a single integration (13 s; see Figure 3.5). Consequently, we peeled Cyg A and Cas A from the data set using a new solution for each integration.

In addition, the largest angular scale of Cas A is  $\sim 8'$ , and the largest angular scale of Cyg A is  $\sim 2'$ . With an  $\sim 10'$  resolution on its longest baselines at 73 MHz, the OVRO-LWA marginally resolves both sources. A resolved source model is needed for both sources. We fit a self-consistent resolved source model to each source. This is performed by minimizing the variance within an aperture located on each source after peeling. By phasing up a large number of integrations before imaging (at least 1 hour), it is possible to smear out the contribution of the rest of the sky. We then use a nonlinear optimization routine (NLopt Sbplx; Rowan, 1990; Johnson, 2008) to vary the parameters in a source model until the variance within the aperture is minimized. Cyg A is modeled with two Gaussian components, while Cas A is modeled with three Gaussian components. Ultimately, these multicomponent models are used to

peel Cyg A and Cas A, but residual errors from this model and from the ionosphere (particularly while these sources are at low elevations) contribute residual artifacts that are largely localized to within  $1^\circ$  of each source.

### Other Bright Sources

Other bright sources – namely Vir A, Tau A, Her A, Hya A, 3C 123, and 3C 353 – are also removed from the visibilities prior to imaging. Because these sources are much fainter than Cyg A and Cas A, we do not need resolved source models to be able to remove these sources from the visibilities without residual sidelobes contaminating the image.

However, the ionosphere will cause these sources to scintillate and refract. The position and flux of each source is measured separately in each channel and integration. The sources are then subtracted from the visibilities using the updated position and flux of the source. The brightest of these sources (Vir A and Tau A) are peeled using a direction-dependent calibration when they are at high elevations.

### The Sun

The Sun can be trivially removed from any map of the sky by constructing the map using only data collected at night. A map of the entire sky can be obtained by using observations spaced 6 months apart. However, the data set used in this paper consists of 28 consecutive hours. Fortunately, the Sun was not active during this period, which could have greatly increased the difficulty involved in subtracting the Sun.

We attempt to subtract the Sun from the data set with the goal of suppressing its sidelobes. The Sun is well-resolved by the OVRO-LWA, and hence a detailed source model is needed. In fact, the optical depth  $\tau = 1$  surface of the Sun changes with frequency, and as a consequence, a new model is needed at each frequency. While we could fit a limited number of Gaussian components to Cyg A and Cas A, this is insufficient for the Sun. Additionally, while most astronomical sources at these frequencies have negative spectral indices, the Sun has a positive spectral index. Therefore, more care will need to be taken in subtracting the Sun at higher frequencies than at lower frequencies.

The strategy used for removing the Sun below 55 MHz involves fitting a shapelet (Refregier, 2003) model to the Sun and subtracting without the use of direction-

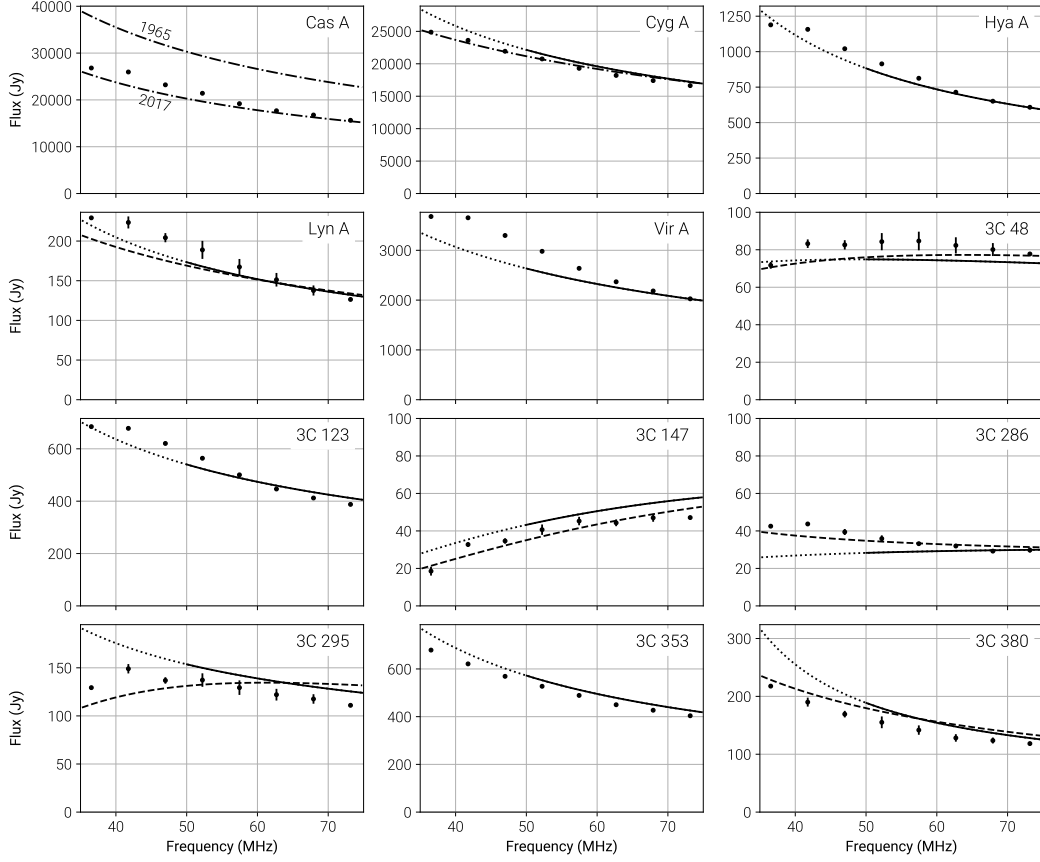


Figure 3.7: Measured fluxes (black points) of 11 sources plotted against the published spectra from Perley & Butler (2017) (solid line above 50 MHz, dotted line below 50 MHz), Scaife & Heald (2012) (dashed line), and Baars et al. (1977) (dot-dashed line). Cas A is compared against a spectrum assuming a secular decrease of 0.77% per year (Helmboldt & Kassim, 2009).

dependent gains. The shapelet fitting is performed in the visibility space. Above 55 MHz, a model is fit to the Sun by minimizing the residuals after peeling (in the same way that models are obtained for Cyg A and Cas A). The Sun is then peeled from each integration using direction-dependent gains.

### Flux Scale

The flux scale of the data was tied to the Baars et al. (1977) spectrum of Cyg A during gain calibration. However, gain calibration is also a function of the beam model and the spectrum used for Cas A. Recent work by Scaife & Heald (2012) (hereafter SH12) using archival data from the literature and Perley & Butler (2017) (hereafter PB17) using the VLA has expanded the number of low-frequency radio sources with calibrated flux measurements from one (Cyg A) to 11 in total. While

the SH12 flux scale is valid between 30 and 300 MHz, the PB17 flux scale is somewhat more limited because the lowest-frequency observations come from the VLA 4-band system. As a consequence, the PB17 flux scale is not valid below 50 MHz.

Figure 3.7 shows a comparison between flux measurements made using the all-sky maps from this work and spectra from the aforementioned flux scales. Generally, the OVRO-LWA flux measurements agree to between 5% and 10% of the SH12 spectra. Below 50 MHz, there can be substantial departures with respect to the extrapolated PB17 spectra (e.g., 3C 286, 3C 295, and 3C 380), but it is usually the case that we have much better agreement with the SH12 spectra. This indicates that the PB17 spectra cannot be extrapolated below 50 MHz.

### 3.4 Results

We constructed eight sky maps using Tikhonov-regularized  $m$ -mode analysis imaging and CLEANing with observations from the OVRO-LWA. Each map is individually shown in Figure 3.8, Figure 3.9 is a three-color image constructed from the maps at 36.528, 52.224, and 73.152 MHz, and Figure 3.10 is a cutout of the galactic plane. The maps cover the sky north of  $\delta = -30^\circ$  with  $\sim 15'$  angular resolution. The eight brightest northern hemisphere point sources are removed from each map (Cyg A, Cas A, Vir A, Tau A, Her A, Hya A, 3C 123, and 3C 353), as described in §3.3, and there is a small blank region near  $l = +45.7^\circ$ ,  $b = -47.9^\circ$  corresponding to the position of the Sun during the observing window. The properties of each map – including frequency, bandwidth, angular resolution, and thermal noise – are presented in Table 3.1.

Each map from Figure 3.8 will be made freely available online in Healpix format (Górski et al., 2005) on LAMBDA.

Due to the considerations presented by Venumadhav et al. (2016) and discussed in §3.2, each of these maps is monopole-subtracted ( $a_{00} = 0$ ). Furthermore, in order to suppress sources of terrestrial interference, all spherical harmonics with  $m = 0$ , or  $m = 1$  and  $l > 100$  are filtered from the map (where the spherical harmonics are defined in the J2017 coordinate system). As will be discussed in §3.5, these spherical harmonics are particularly susceptible to contamination by radio-frequency interference (RFI) and common-mode pickup. As a consequence, astronomical emission that circles the J2017 north celestial pole (NCP) is filtered from the maps. This filtering creates negative rings around the NCP at the declination

| # | $\nu$<br>MHz | $\Delta\nu^a$ | FWHM <sup>b</sup>    |                      | Noise <sup>c</sup>   |               | Fraction of Modes <sup>d</sup><br>with $\sigma > \sqrt{\varepsilon}$ |
|---|--------------|---------------|----------------------|----------------------|----------------------|---------------|----------------------------------------------------------------------|
|   |              |               | $\delta = 0^\circ$   | $\delta = +45^\circ$ | $\delta = +75^\circ$ | K<br>mJy/beam |                                                                      |
| 1 | 36.528       | 0.024         | 26.0' $\times$ 19.1' | 20.2' $\times$ 16.9' | 19.8' $\times$ 18.7' | 595.          | 799.                                                                 |
| 2 | 41.760       | 0.024         | 23.3' $\times$ 17.5' | 18.5' $\times$ 16.0' | 18.3' $\times$ 17.4' | 541.          | 824.                                                                 |
| 3 | 46.992       | 0.024         | 20.9' $\times$ 16.3' | 17.4' $\times$ 15.2' | 17.6' $\times$ 16.9' | 417.          | 717.                                                                 |
| 4 | 52.224       | 0.024         | 18.7' $\times$ 15.2' | 16.2' $\times$ 15.0' | 16.0' $\times$ 15.8' | 418.          | 814.                                                                 |
| 5 | 57.456       | 0.024         | 18.0' $\times$ 14.9' | 15.9' $\times$ 15.0' | 15.7' $\times$ 15.4' | 354.          | 819.                                                                 |
| 6 | 62.688       | 0.024         | 17.8' $\times$ 15.0' | 15.8' $\times$ 14.9' | 15.7' $\times$ 15.4' | 309.          | 843.                                                                 |
| 7 | 67.920       | 0.024         | 17.6' $\times$ 15.0' | 15.9' $\times$ 14.7' | 15.8' $\times$ 15.6' | 281.          | 894.                                                                 |
| 8 | 73.152       | 0.024         | 18.6' $\times$ 15.1' | 16.8' $\times$ 14.6' | 16.6' $\times$ 16.1' | 154.          | 598.                                                                 |
|   |              |               |                      |                      |                      |               | 0.512                                                                |

Table 3.1: A summary of the generated all-sky maps.

<sup>a</sup> Bandwidth used to construct the map. As described in the text, each map is constructed from a single frequency channel (24 kHz).

<sup>b</sup> The full width at half maximum (FWHM) of the synthesized beam at the specified declination (major axis  $\times$  minor axis).

<sup>c</sup> Measured with a jackknife and splitting the data set into even- and odd-numbered integrations. This estimate therefore includes all noise sources that act on the timescale of a single 13 s integration (e.g., thermal, ionospheric, etc.).

<sup>d</sup> Singular values of the transfer matrix compared with the value of the regularization parameter  $\varepsilon$  used while solving Equation 3.9. As discussed in the text, singular vectors with corresponding singular values  $\sigma \ll \sqrt{\varepsilon}$  are set to zero by the Tikhonov regularization procedure.

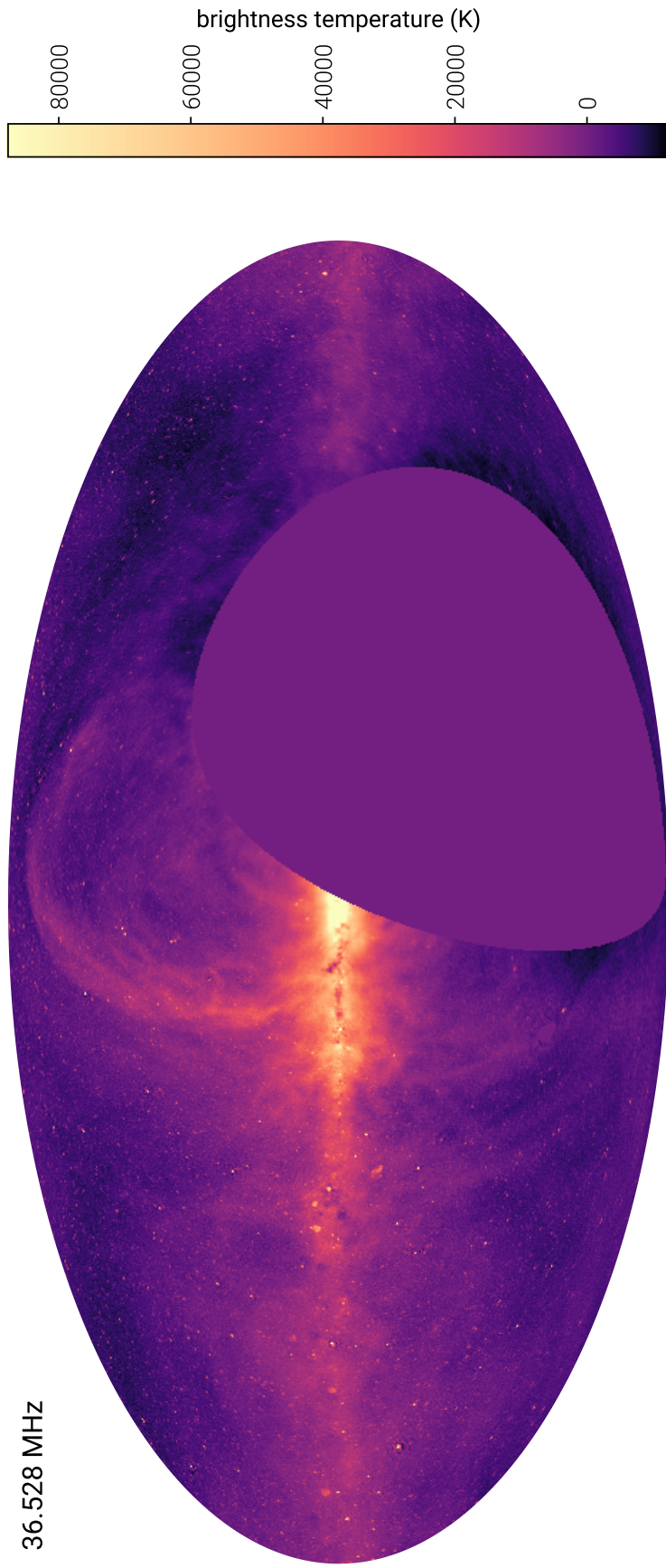


Figure 3.8: These eight panels illustrate (with a Mollweide projection and logarithmic color scale) the eight full-sky maps generated with Tikhonov-regularized  $m$ -mode analysis imaging and the OVRO-LWA. Each map covers the sky north of  $\delta = -30^\circ$  with angular resolution of  $\sim 15'$ . Eight bright sources have been removed from each map (Cyg A, Cas A, Vir A, Her A, Hya A, 3C 123, and 3C 353). The small blank region near  $l = +45.7^\circ$ ,  $b = -47.9^\circ$  corresponds to the location of the Sun during the observation period. A detailed summary of the properties of each map is given in Table 3.1.

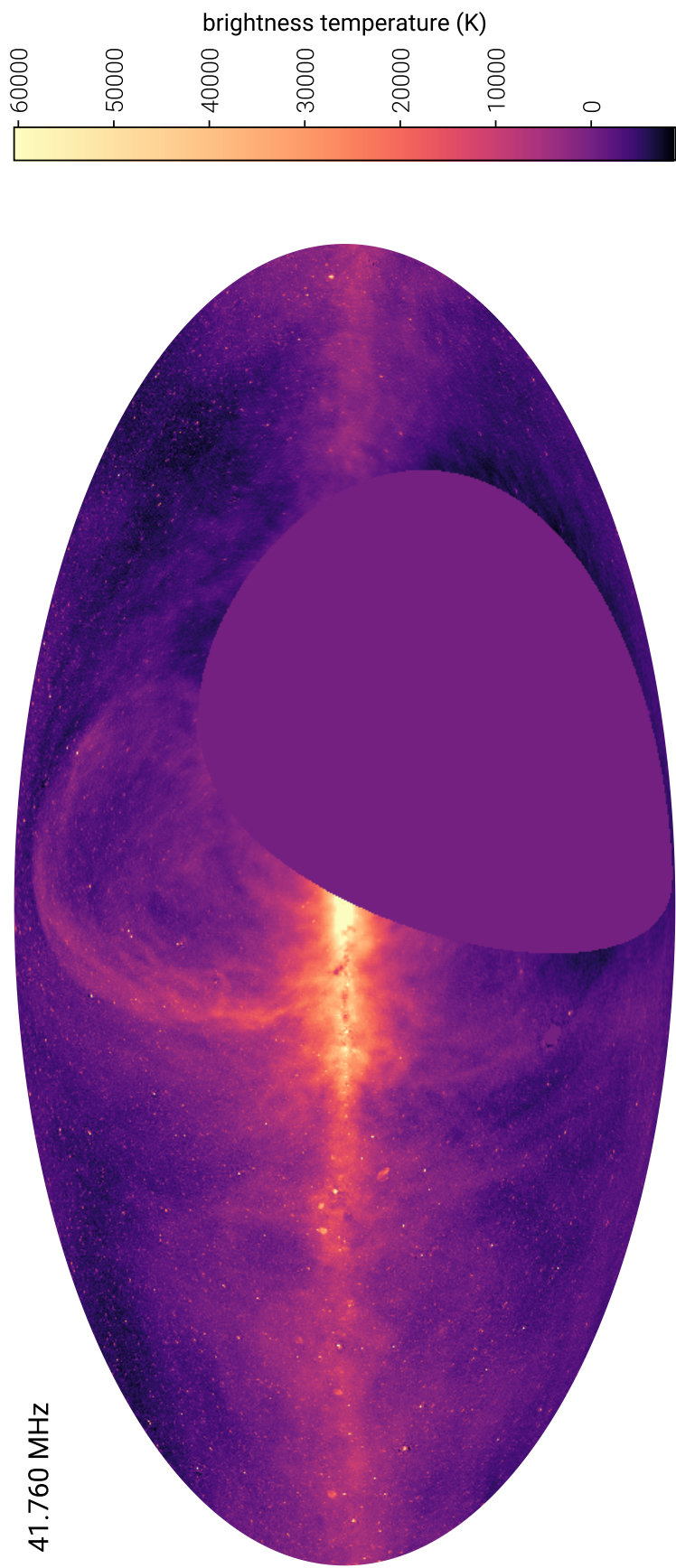


Figure 3.8: continued

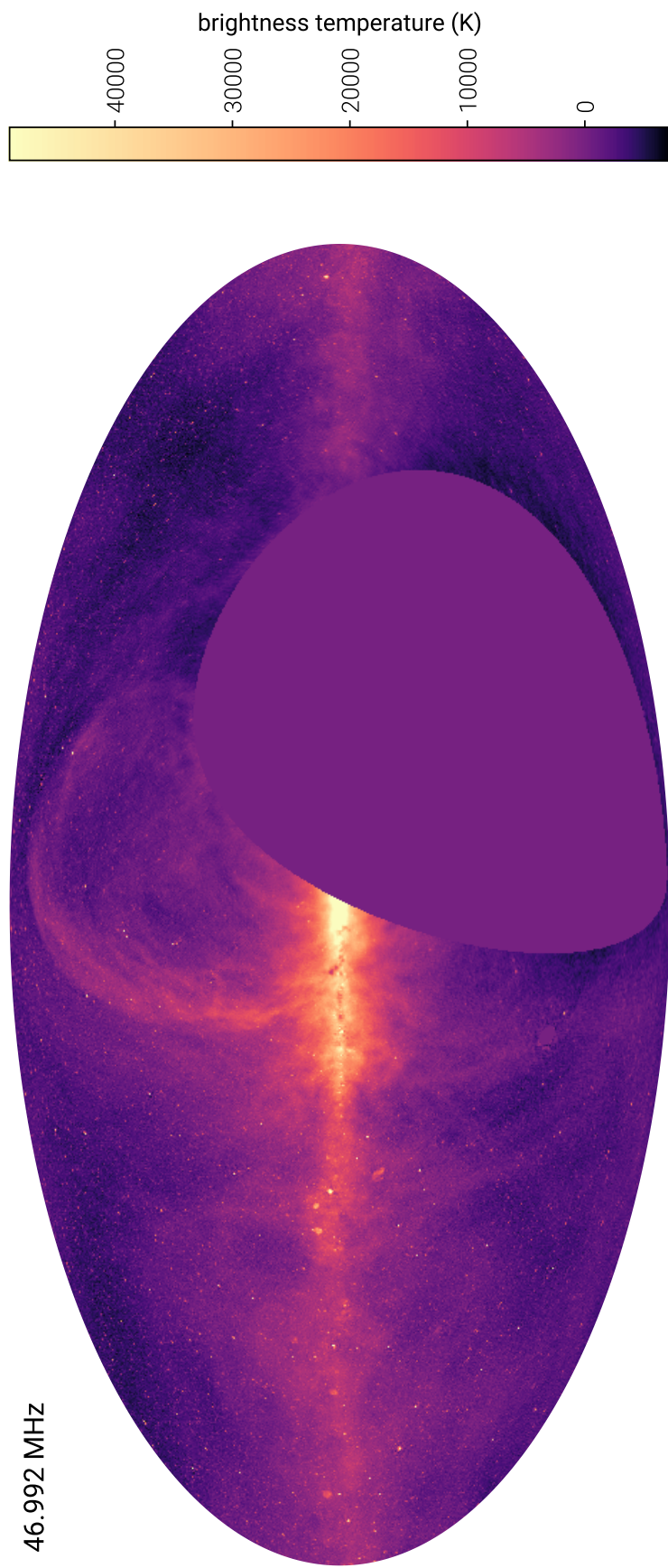


Figure 3.8: continued

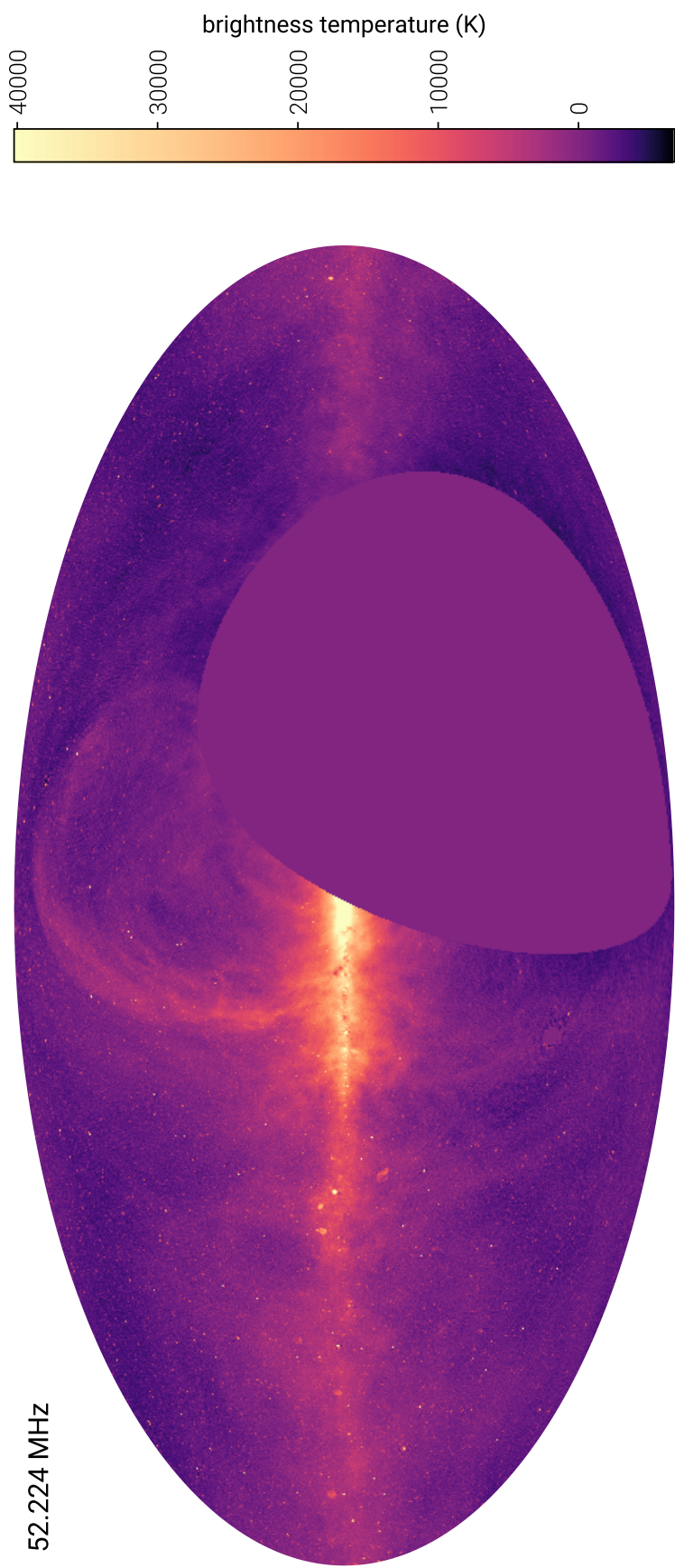


Figure 3.8: continued

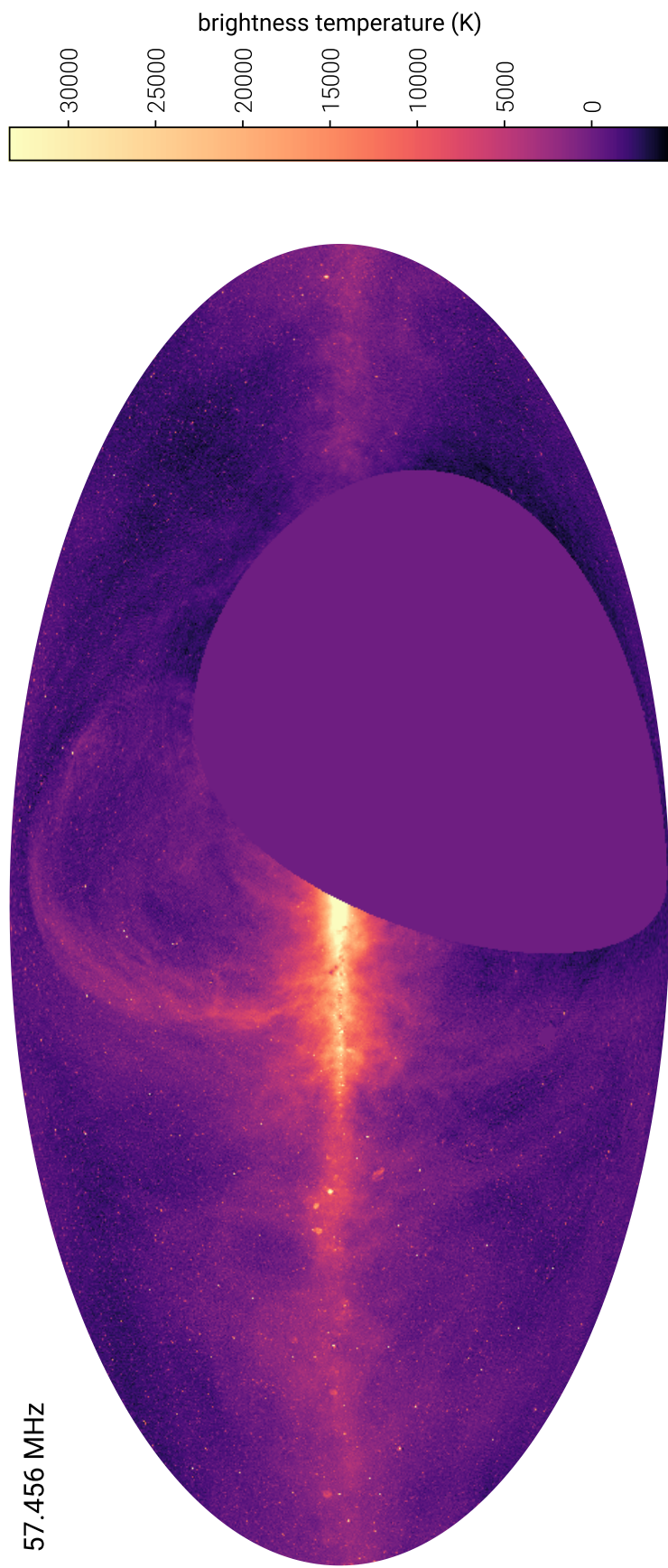


Figure 3.8: continued

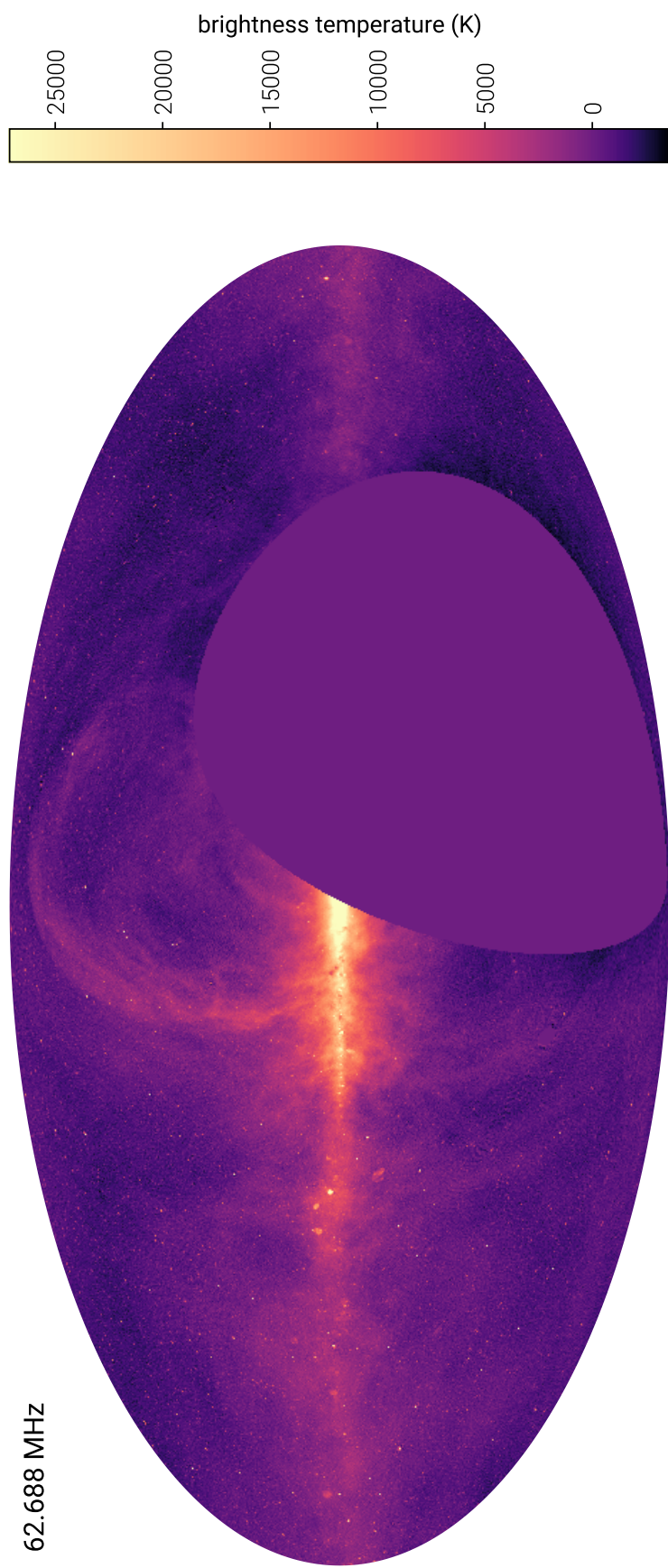


Figure 3.8: continued

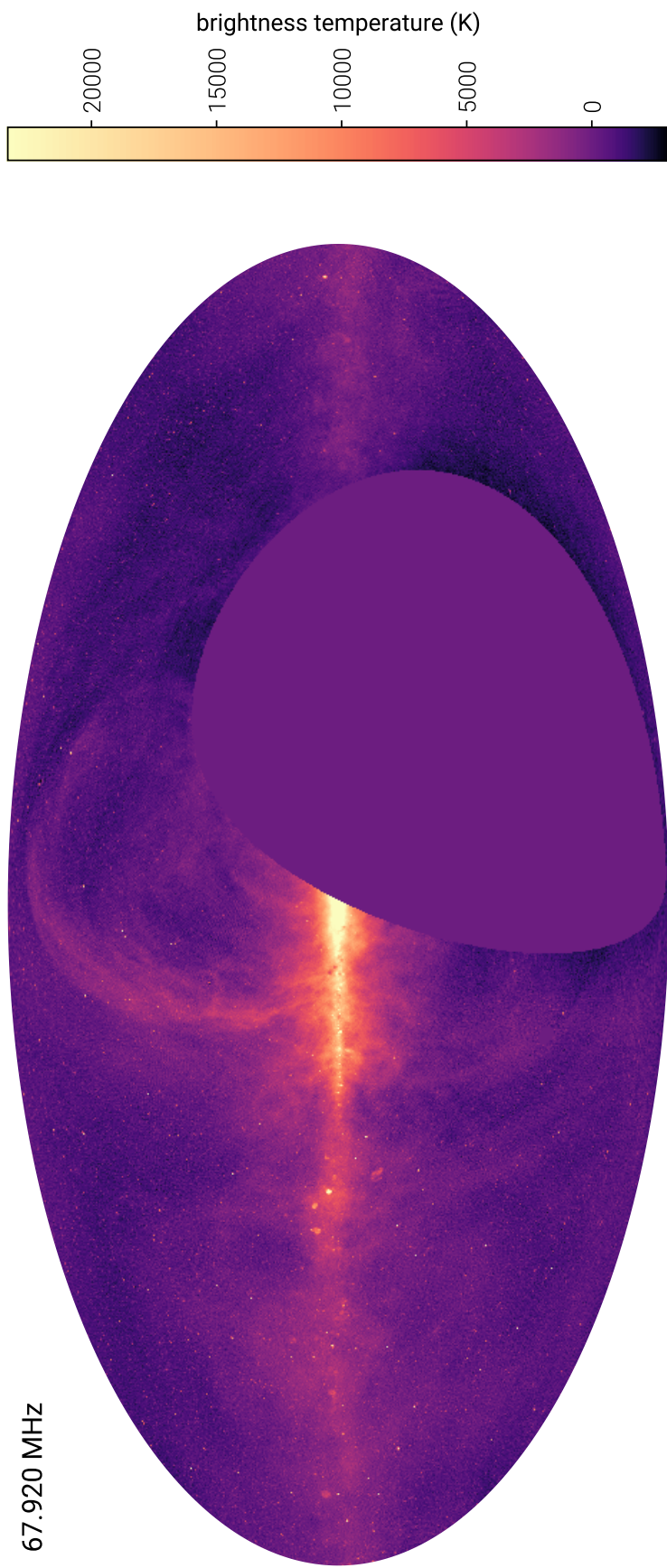


Figure 3.8: continued

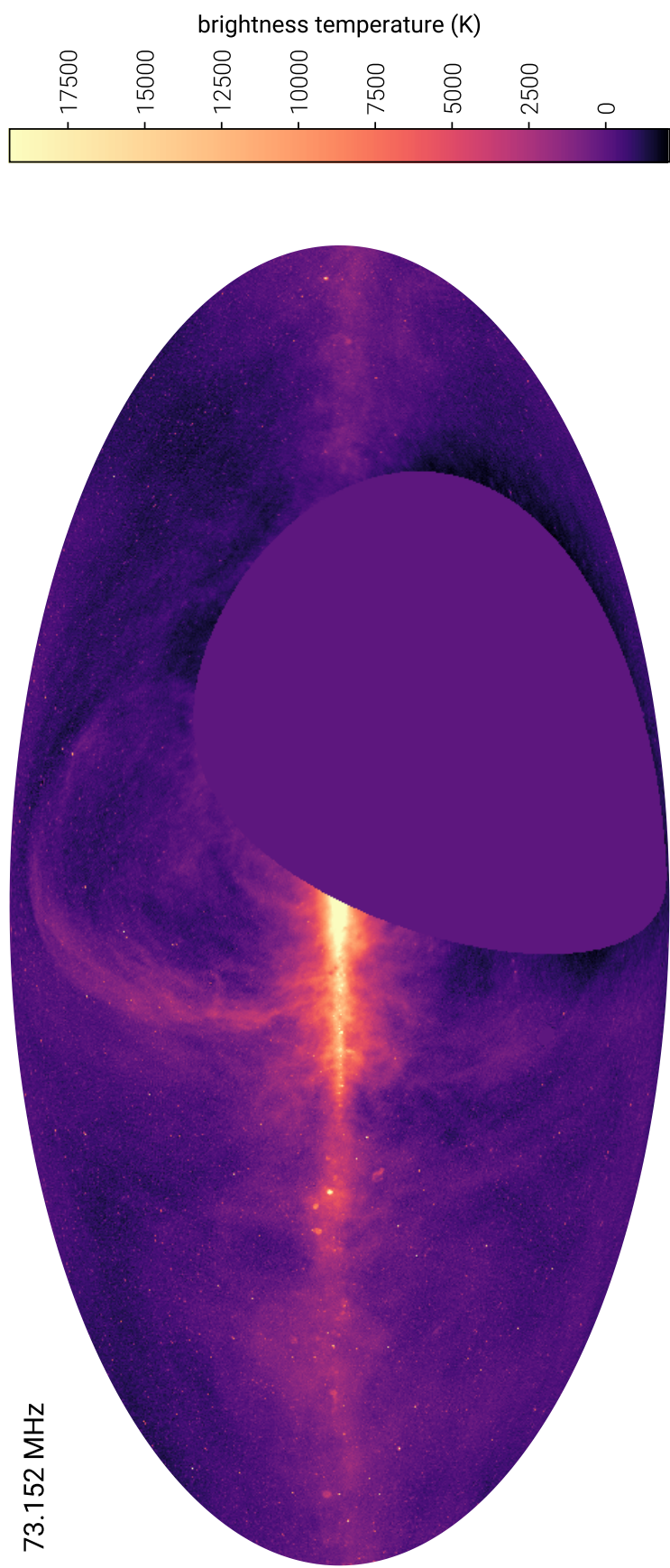


Figure 3.8: continued



Figure 3.9: This Mollweide-projected map is constructed from three maps of the sky at 36.528 MHz (red), 52.224 MHz (green), and 73.152 MHz (blue). The maps are scaled by  $\nu^{2.5}$  before combining, and the color scale is logarithmic (as in Figure 3.8). Therefore, regions with a spectral index of  $-2.5$  will tend to appear white, and regions with a flatter spectral index will tend to appear blue.

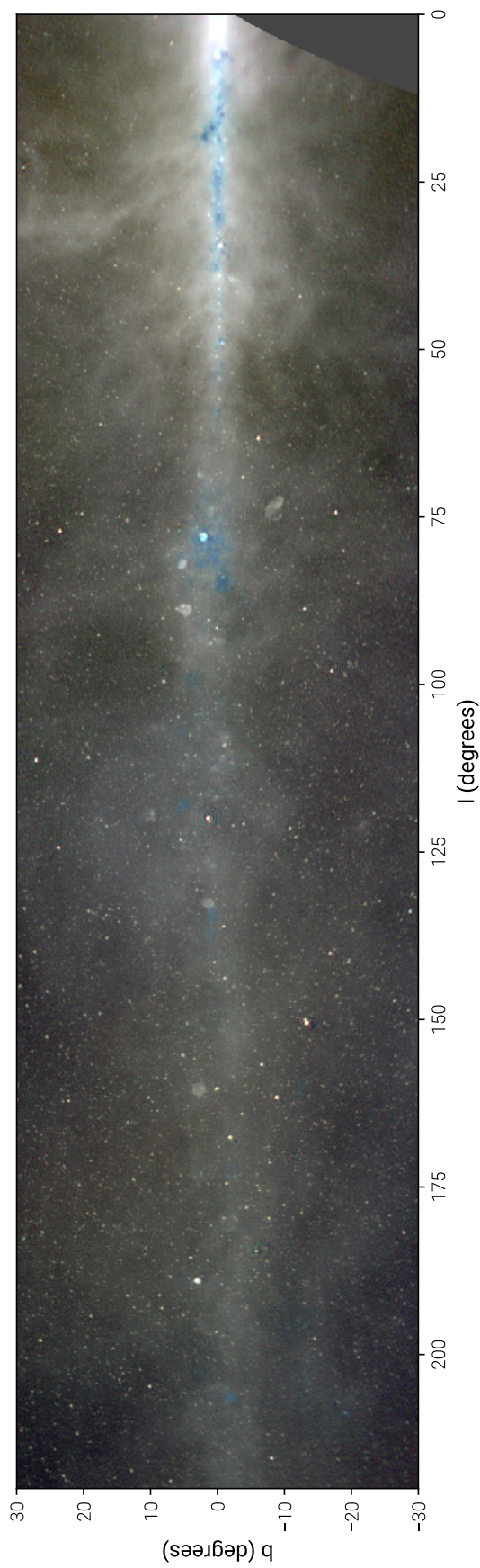


Figure 3.10: Cutout of the galactic plane from Figure 3.9.

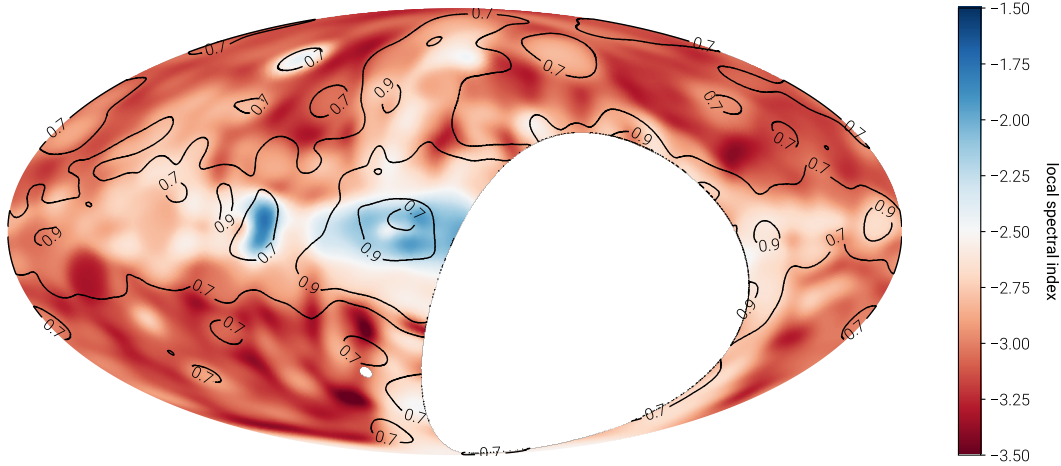


Figure 3.11: Local spectral index measured between the 36.528 MHz map and the 73.152 MHz map estimated by means of a local T–T plot. The color scale gives the spectral index, where blue is flat spectrum and red is steep spectrum. The contours give the coefficient of determination ( $R^2$ ) for the linear fit to the local T–T plot. If  $R^2$  is low, the quality of the fit is low, and the estimated spectral index is unreliable. This can be due to either insufficient dynamic range in the local T–T plot or multiple emission mechanisms operating in close proximity. Consequently,  $R^2$  tends to drop at higher galactic latitudes (due to dynamic range) and near H II regions in the galactic plane (due to multiple emission mechanisms).

of bright point sources. These rings are naturally removed from the map during CLEANing as long as this filtering step is included in the PSF calculation.

The noise in each map is empirically measured using jackknife resampling. The data set is first split into even- and odd-numbered integrations. These two groups are then imaged and CLEANed independently before being compared against the maps constructed from all of the available data using the jackknife standard error estimator. This estimate of the standard error includes all sources of error that operate on  $\sim 13$  s timescales (the integration time), such as thermal noise and rapid ionospheric fluctuations, but does not account for more slowly varying effects (for example, sidereal variation in the system temperature or day–night fluctuations in the ionosphere). These noise calculations are summarized in Table 3.1. VLSSr source counts (Lane et al., 2014) suggest that the confusion limit at 74 MHz and 15' angular resolution is  $\sim 1000 \times (\nu/74 \text{ MHz})^{-0.7}$  mJy. Each channel map achieves thermal noise  $< 900$  mJy; therefore, each map is likely at or near the confusion limit.

In the absence of a zero-level correction, a pixel-by-pixel power-law fit to the new

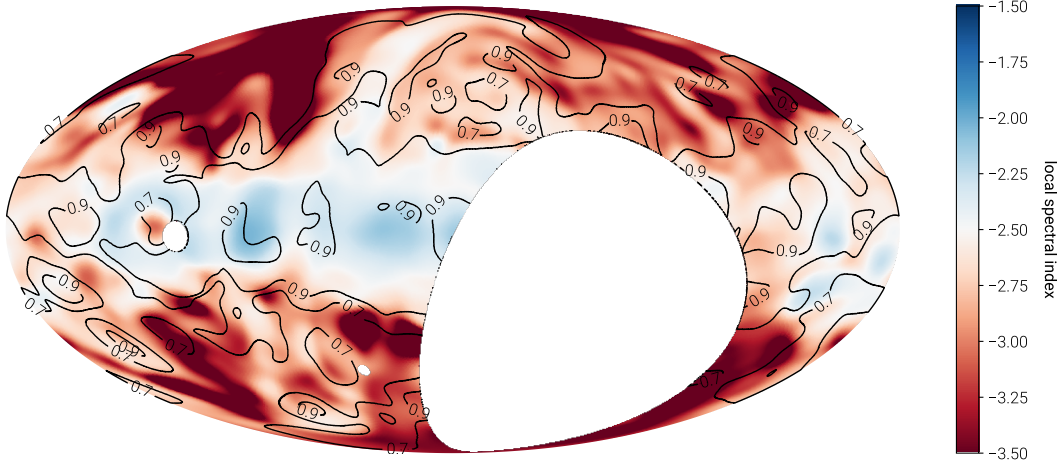


Figure 3.12: Local spectral index measured between the 73.152 MHz OVRO-LWA map and the reprocessed 408 MHz Haslam map (Remazeilles et al., 2015). The color scale gives the spectral index, where blue is flat spectrum and red is steep spectrum. The contours give the coefficient of determination ( $R^2$ ) for the linear fit to the local T-T plot. See the caption of Figure 3.11 for more details about the coefficient of determination.

maps is impossible. In general, this zero-level correction requires calibrated total power measurements that will be included in future work. Instead, temperature–temperature plots (T–T plots) can be used to measure the spectral index independently of any zero-level corrections (Turtle et al., 1962). This method relies on the assumption that all pixels in a given region are described by the same power law. In that case, there exists a linear relationship between the brightness temperature at frequency  $\nu_1$  and frequency  $\nu_2$ . The slope of this best-fit line is a measure of the spectral index between the two frequencies. The T–T plot can fail to obtain a reliable measure of the spectral index in two ways. First, if there is not enough dynamic range in the emission region, there may be only a weak correlation between the brightness temperature at  $\nu_1$  and  $\nu_2$ . Second, if two emission mechanisms operate in close proximity (i.e., synchrotron and free-free), then a single power-law interpretation of the emission in that region will be poor. Consequently, spectral indices estimated from T–T plots can require careful interpretation.

In Figure 3.11, the spectral index is locally estimated in each part of the sky within a region  $\sim 10^\circ$  across by constructing local T–T plots between 36.528 and 73.152 MHz. Contours of constant  $R^2$  (the coefficient of determination) are overlaid. If  $R^2 \sim 1$ , the spectral index is reliable because there is locally a strong linear correlation between 36.528 and 73.152 MHz. However, if  $R^2 \ll 1$ , the spectral

index calculation is unreliable.  $R^2$  tends to drop in cold patches of the sky where there is not enough dynamic range to find a strong correlation between the two frequencies. It also tends to drop in the vicinity of H II regions in the galactic plane due to multiple emission mechanisms violating the assumption of a single spectral index. Therefore, we should restrict our interpretation of Figure 3.11 to the galactic plane and north galactic spur. In the galactic plane, the synchrotron spectral index varies between  $\sim -2.5$  and  $-2.75$ . In the vicinity of H II regions, the spectral index flattens significantly. These H II regions can be seen with higher resolution in Figure 3.10. In Figure 3.10, H II regions appear as blue shadows along the galactic plane due to the increasing impact of free-free absorption at lower frequencies.

In the literature, the spectral index at low frequencies is commonly computed with respect to the Haslam 408 MHz map (Haslam et al., 1981, 1982), which was reprocessed by Remazeilles et al. (2015) to remove artifacts associated with  $1/f$  noise and bright sources. Figure 3.12 displays the spectral index computed between the 73.152 MHz map and the reprocessed Haslam map. The spectral index was estimated by degrading the 73.152 MHz map to the resolution of the Haslam map and constructing local T-T plots in every direction. The coefficient of determination is overlaid as a contour plot; however, because  $\log(408 \text{ MHz}/73.152 \text{ MHz}) > \log(73.152 \text{ MHz}/36.528 \text{ MHz})$ , the spectral indices presented in Figure 3.12 tend to be more robust than those presented in Figure 3.11. This is reflected by the fact that  $R^2$  is larger, but the interpretation must still generally be restricted to the galactic plane.

## Comparisons with Other Sky Maps

### LWA1 Low Frequency Sky Survey

The LWA1 Low Frequency Sky Survey (LLFSS; Dowell et al., 2017) produced nine maps of the sky between 35 and 80 MHz. Six of these maps are interior to the frequency range spanned by this work. Initial comparisons with the LLFSS helped characterize a systematic rotation in the LWA1's antenna positions. After phase calibration, this manifested itself as a systematic rotation and translation in the snapshot images that were mosaicked to form the final sky map. This systematic error has been corrected in the comparisons presented here and in the latest version of the LLFSS.<sup>7</sup>

---

<sup>7</sup> Available for download at <http://lwa10g.alliance.unm.edu/LWA1LowFrequencySkySurvey/>

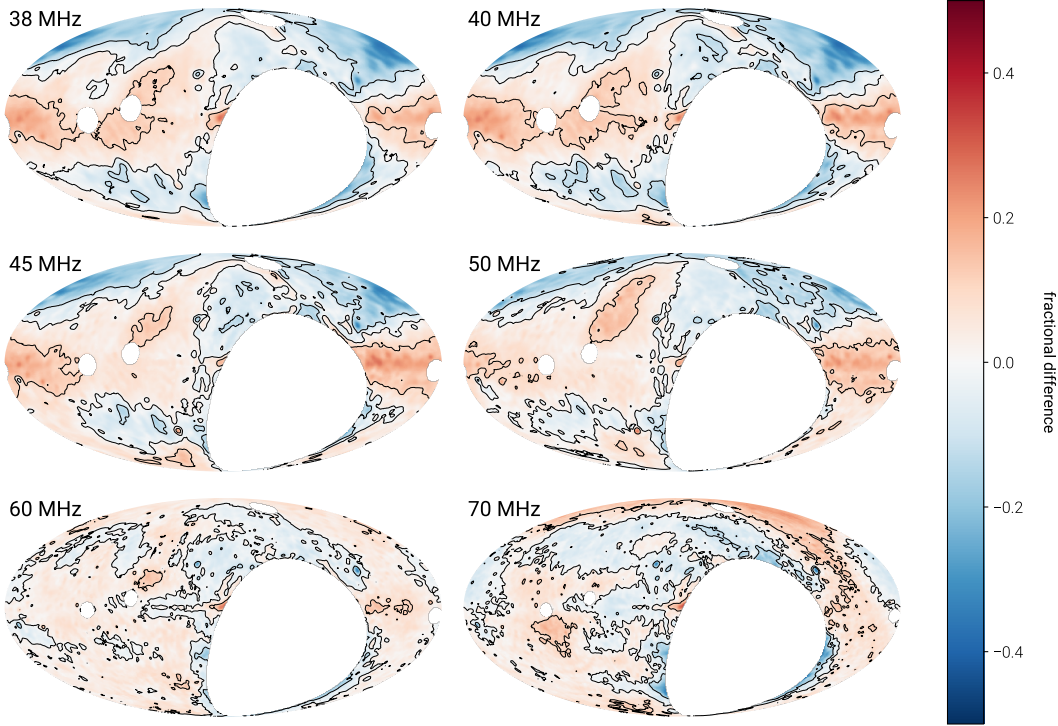


Figure 3.13: Fractional difference between maps from the LLFSS and the OVRO-LWA maps (Figure 3.8) after interpolating to the corresponding frequency and smoothing to the corresponding resolution. A positive value indicates regions where the OVRO-LWA map has more emission than the corresponding LLFSS map. Cas A, Cyg A, Vir A, and Tau A are masked due to the fact that they are subtracted from the OVRO-LWA maps.

A direct comparison with these updated LLFSS maps can be seen in Figure 3.13. In this figure, the LLFSS maps are filtered to remove the monopole and all modes with  $m = 0$ . The OVRO-LWA maps are interpolated in frequency and blurred to match the angular resolution of the corresponding LLFSS map. At 60 MHz, the agreement is generally better than 10%. However, at lower frequencies the agreement deteriorates to about 20%. Typically, the OVRO-LWA maps have excess emission in the galactic plane and a deficit of emission off the galactic plane relative to the LLFSS.

The LLFSS incorporates calibrated total power radiometry to estimate the missing flux from short spacings. As a result, Dowell et al. (2017) reported per-pixel spectral indices from combining all nine sky maps. Care must be taken in comparing these spectral indices with Figure 3.11 because they are susceptible to different systematic errors. Both calculations are sensitive to mistakes in the antenna primary beam,

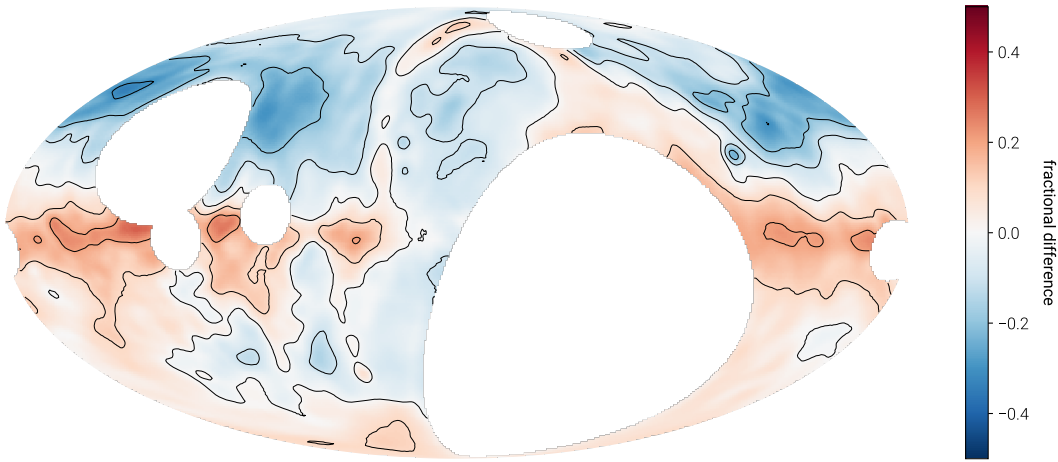


Figure 3.14: This Mollweide-projected map compares the fractional difference between the Guzmán 45 MHz map and the OVRO-LWA maps (Figure 3.8) interpolated to 45 MHz (degraded to  $5^\circ$  resolution). A positive value indicates regions where the OVRO-LWA map has more emission than the Guzmán map, and a negative value indicates regions where the Guzmán map has more emission than the OVRO-LWA map. Cas A, Cyg A, Vir A, and Tau A are masked due to the fact that they are subtracted from the OVRO-LWA maps but not the Guzmán map.

but the LLFSS spectral indices are additionally sensitive to errors in the zero level. We will restrict the comparison to the galactic plane where the spectral indices are likely to be the most reliable. Toward the galactic center, both surveys agree that the spectral index is very flat ( $> -2.2$ ) due to the influence of free-free absorption. However, at galactic latitudes  $\sim 180^\circ$  this work suggests that the spectral index varies between -2.5 and -2.75, while the LLFSS reports substantially flatter indices in the range -2.3 to -2.2. In this region,  $0.7 < R^2 < 0.9$  for the OVRO-LWA, so this could be an artifact of the comparatively weak correlation between the brightness at 36.528 and 73.152 MHz, which tends to bias the spectral index toward  $-\infty$ .

The LLFSS also computes spectral indices with respect to the Haslam 408 MHz map. These spectral indices are subject to the same caveats and systematic errors as before. However, in general, the qualitative agreement with Figure 3.12 is better, potentially due to the increased robustness associated with estimating spectral indices with a larger fractional bandwidth.

### Guzmán 45 MHz Map

The Guzmán 45 MHz map (Guzmán et al., 2011) is compiled from a southern hemisphere survey (Alvarez et al., 1997) and a northern hemisphere survey (Maeda

et al., 1999), with a small gap around the NCP. In this work, the zero level is set by comparing against published low-frequency measurements in six different directions.

A direct comparison between the OVRO-LWA maps interpolated to 45 MHz and the Guzmán 45 MHz map can be seen in Figure 3.14. In order to make this comparison, the OVRO-LWA map was degraded to a  $5^\circ$  resolution by convolving with a Gaussian kernel, and the Guzmán map has had spherical harmonics with  $m = 0$  discarded in order to make it consistent with the maps presented in this paper. This figure shows an  $\sim 20\%$  excess of emission in the galactic plane that is consistent with the discrepancy observed between the LLFSS and the Guzmán map. However, while the LLFSS has an excess of emission near the north galactic pole, no such excess is observed in this work. Instead, there is a 10% excess of emission near the south galactic pole. Elsewhere off the plane of the galaxy, the discrepancy can be as much as  $-20\%$ .

Guzmán et al. (2011) computed the spectral index between their 45 MHz map and the 408 MHz Haslam map. Along the galactic plane, the spectral index varies between -2.2 (in the vicinity of H II regions) and -2.5 (at galactic longitudes  $\sim 180^\circ$ ). The north galactic spur has a spectral index of -2.5. This is generally consistent with the results presented in Figure 3.12.

### 3.5 Error Analysis

#### The Ionosphere

One of the key assumptions made by  $m$ -mode analysis is that the sky is static. We assume that the only time-dependent behavior is the rotation of the Earth, which slowly rotates the sky through the fringe pattern of the interferometer. At low frequencies, the ionosphere violates this assumption. In particular, ionospheric scintillation and refractive offsets will cause even static sources to exhibit significant variability (Figure 3.5).

The correlation observed on a given baseline for a single point source is

$$V_\nu(t_{\text{sidereal}}) = I_\nu B_\nu(t_{\text{sidereal}}), \quad (3.19)$$

where  $I_\nu$  is the flux of the source at the frequency  $\nu$ , and  $B_\nu$  is the baseline transfer function defined by Equation 3.3. The transfer function is a function of the direction to the source, which is in turn a function of the sidereal time  $t_{\text{sidereal}}$ . If the source is varying, from intrinsic variability or due to scintillation, then the source flux is also

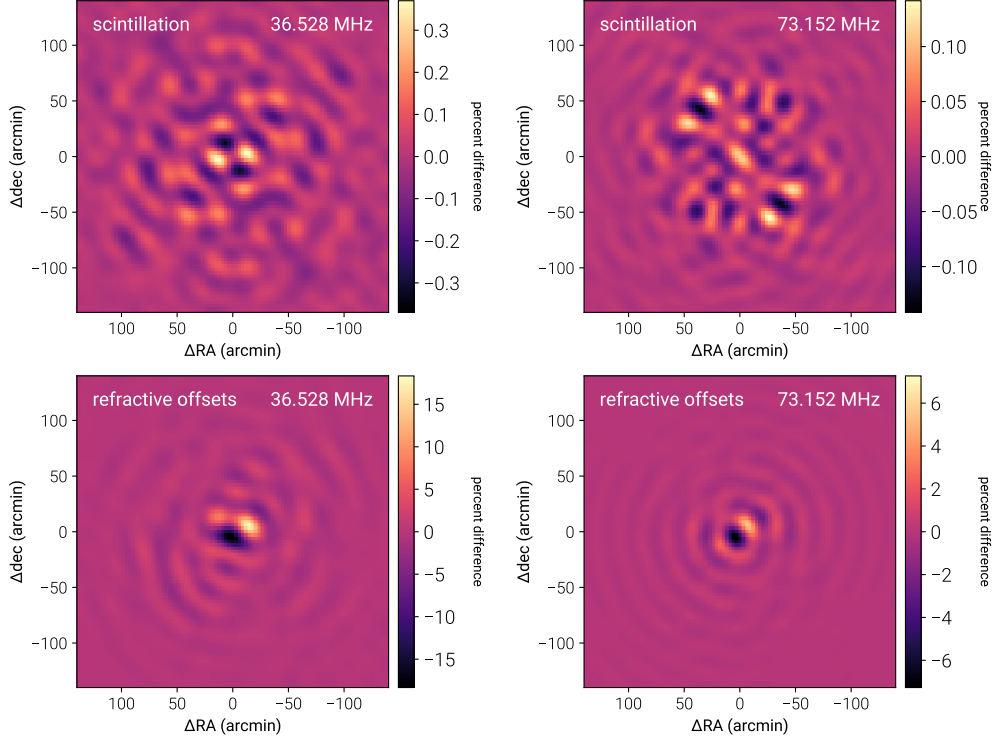


Figure 3.15: Illustration of the corrupting influence of the ionosphere at 36.528 MHz (left column) compared with 73.152 MHz (right column). Each panel shows the simulated PSF for a source at the location of Cas A and illustrates the percent difference (relative to the peak flux of the uncorrupted PSF) due to including an ionospheric effect. In the top row, the simulated source scintillates using the measured light curve for Cas A in Figure 3.5. In the bottom row, the simulated source is refracted from its true position using the measured refractive offsets for Cas A in Figure 3.5.

a function of the time coordinate  $t$  such that

$$V_\nu(t_{\text{sidereal}}) = I_\nu(t)B_\nu(t_{\text{sidereal}}), \quad (3.20)$$

where  $t_{\text{sidereal}} = (t \bmod 23^h 56^m)$ .

In order to compute the  $m$ -modes, we must take the Fourier transform with respect to the sidereal time. As a consequence of the Fourier convolution theorem, we find

$$V_{\nu,m} \sim \sum_{m'} V_{m'}^{\text{static}} I_{\nu,m-m'}, \quad (3.21)$$

where  $V_{\nu,m}^{\text{static}}$  is the set of observed  $m$ -modes if the source was actually static, and  $I_{\nu,m-m'}$  is the Fourier transform of the light curve  $I_\nu(t)$ . Equation 3.21 indicates that power is scattered between different values of  $m$ . As a consequence, the true transfer

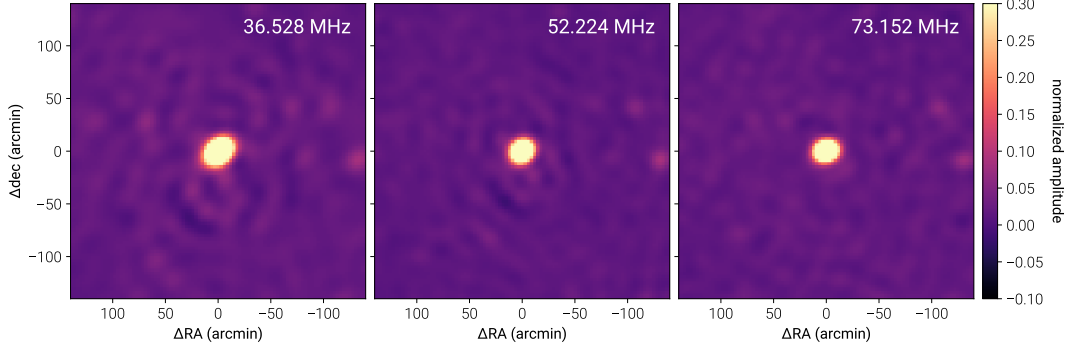


Figure 3.16: Zoom-in of 3C 134 at 36.528 MHz (left panel), 52.224 MHz (middle panel), and 73.152 MHz (right panel). At 36.528 MHz there are  $\sim 10\%$  artifacts around 3C 134 that persist after CLEANing due to ionospheric effects. As expected for an ionospheric origin, these artifacts decrease in amplitude as frequency increases. Figure 3.15 shows the typically expected amplitude of these effects for ionospheric scintillation and refractive offsets.

matrix, which is exactly block diagonal in the ideal case, is no longer truly block diagonal (Shaw, 2016).

The maps presented in Figure 3.8 do not account for any off-diagonal terms arising from ionospheric fluctuations. The effect of this can be seen in Figure 3.15. In this simulation, a point source is placed at the location of Cas A. In one case, the source is allowed to scintillate in the same way Cas A does in Figure 3.5, but the source is always located exactly at the location of Cas A. In the second case, the source position is allowed to vary in the same way Cas A does in Figure 3.5, but the flux of the source exactly traces the beam model. The scintillation, although large, introduces only  $< 0.3\%$  errors in the vicinity of bright point sources. Refractive offsets, however, can introduce  $\sim 15\%$  errors at 36.528 MHz and  $\sim 5\%$  errors at 73.152 MHz. Because the sidelobes of the PSF are altered from that of the ideal PSF, refractive offsets will restrict the dynamic range it is possible to obtain with the CLEAN algorithm described in §3.2. This effect can be clearly seen in Figure 3.16, where 10% errors within  $1^\circ$  of 3C 134 are seen at 36.528 MHz. As expected for an ionospheric effect, these errors decrease to a few percent at 52.224 MHz, and less at 73.152 MHz. We therefore conclude that ionospheric effects directly limit the dynamic range in the vicinity of bright point sources.

## Beam Errors

A model of the antenna beam is essential for wide-field imaging. Because  $m$ -mode analysis imaging operates on a full sidereal day of data, images are constructed after

watching each point in the sky move through a large slice of the beam (excepting the celestial poles). The beam model therefore serves two purposes:

1. setting the flux scale as a function of declination and
2. reconciling observations from two separate sidereal times.

In the first case, all sources at a given declination take the same path through the antenna primary beam. If the antenna response is overestimated along this track, then all sources at this declination will have underestimated fluxes. Similarly, if the antenna response is underestimated, then all the sources will have overestimated fluxes. The errors in Figure 3.7 do not show a clear pattern with declination. Two sources have a clear systematic offset at all frequencies: 3C 353 and 3C 380. Source 3C 353 is the second southernmost source, but Hya A – the first southernmost source – does not exhibit this systematic error. Similarly, 3C 380 is at a comparable declination to Lyn A, which appears, if anything, to have its flux systematically offset in the other direction. The absence of a coherent pattern does not eliminate the possibility of beam errors affecting the flux scale, but it does mean that these errors are at least comparable to the errors inherent to the flux scale itself.

The second case is more subtle. Sources are observed at a wide range of locations in the primary beam of the antenna. The imaging process must reconcile all of these observations together, and the beam model provides the instructions for how to do this. In the event of an error in the beam model, it can be expected that the beam will introduce errors into the sky maps that will limit the dynamic range in the vicinity of bright point sources. Shaw et al. (2015) simulated the effect of beam errors on a cosmological analysis, concluding that the beam must be known to one part in  $10^4$ . Our requirements are significantly less stringent because we are estimating the sky brightness instead of estimating the amplitude of a faint cosmological signal in the presence of foreground emission that dominates the signal by five orders of magnitude. In fact, in §3.5 we found that ionospheric effects likely dominate over other sources of error that affect the PSF shape. Therefore, we conclude that the beam models generated in §3.3 are sufficient to limit the effect of beam errors on the PSF to at least less than those introduced by the ionosphere.

### Polarization Leakage

Shaw et al. (2015) described how to generalize  $m$ -mode analysis to account for a polarized sky observed with a polarized antenna beam. Heretofore, this general-

ization has been neglected in the discussion of  $m$ -mode analysis imaging. At low frequencies, increasingly rapid Faraday rotation leads to depolarization. Therefore, polarization fractions are generally expected to decrease at low frequencies (varying with ionospheric conditions). Lenc et al. (2016) detected the presence of diffuse polarized emission on degree angular scales with the MWA, also finding typical depolarization ratios of  $\sim 0.3$  for pulsars at 154 MHz relative to 1.4 GHz, although there was a large variance between pulsars. Even more depolarization is expected at frequencies  $\leq 73.152$  MHz, but crossed-dipole antennas with extremely large primary beams will naturally introduce large polarization leakage terms at low elevations. It is instructive to compute what impact this will have on the unpolarized imaging process.

In order to understand the effect of polarization leakage, we simulated a point source with 10% polarization in Stokes  $Q$  at the location of Cas A. The simulated visibilities were computed using the measured beams for the  $x$  and  $y$  dipoles. Because the amplitudes of the two beams are not equal in every direction on the sky, this introduces a direction-dependent leakage of Stokes  $Q$  into Stokes  $I$ . At 73.152 MHz, this leakage is  $\lesssim 5\%$  above  $15^\circ$  elevation but rapidly rises to  $\gtrsim 50\%$  at lower elevations. Obenberger et al. (2015) reported similar polarization leakage measurements with the LWA1. Cas A is a circumpolar source and spends about 7 hours every day skirting the horizon where the polarization leakage is large, so by placing the simulated source at the location of Cas A, we are engineering a situation where the polarization leakage from Stokes  $Q$  into Stokes  $I$  will be large. However, the impact on the unpolarized  $m$ -mode analysis maps is mild, amounting to a 0.5% error in the flux of the source.

### **Terrestrial Interference and Pickup**

When writing Equation 3.2, it is implicitly assumed that the correlated voltage fluctuations measured between pairs of antennas are exclusively generated by astronomical sources of radio emission. In practice, this assumption can be violated. For instance, a low-frequency interferometer located in the vicinity of an arcing power line will see an additional contribution from the RFI generated by the arcing process. Similarly, common-mode pickup along the analog signal path of the interferometer may generate an additional spurious contribution to the measured visibilities. While the amplitude and phase of these contaminating signals may fluctuate with time, they do not sweep across the sky at the sidereal rate characteristic of astronomical sources.

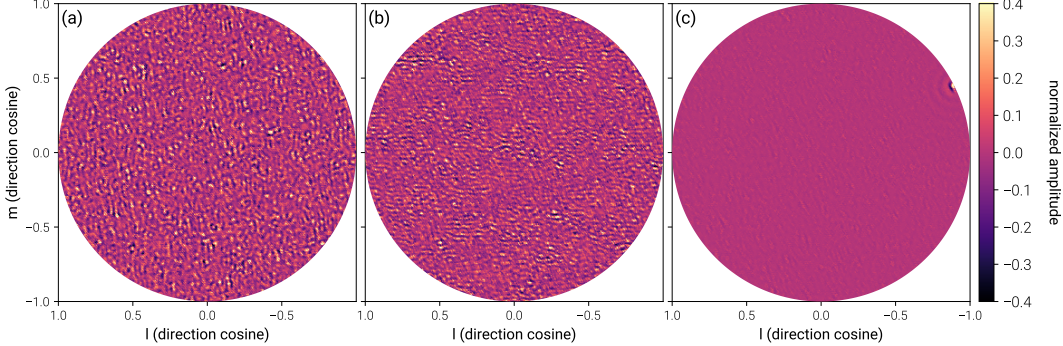


Figure 3.17: Terrestrial sources of correlated noise that are apparent after averaging the visibilities at 62.688 MHz over the entire 28 hour observing period (keeping the phase center at zenith such that astronomical sources of radio emission are smeared along tracks of constant declination). Each panel represents a different component that is removed from the visibilities. The images are generated using WSClean (Offringa et al., 2014), uniform weighting, and only baselines longer than 15 wavelengths. Panels (a) and (b) illustrate components that appear noise-like in image space, but are in fact a constant offset to the measured visibilities likely associated with cross-talk or common-mode pickup. Panel (c) illustrates a component that is clearly associated with an RFI source on the horizon to the west–northwest of the OVRO-LWA. This RFI source is likely an arcing power line. Figure 3.18 illustrates the characteristic ringlike artifacts introduced into the maps if these three components are not removed prior to  $m$ -mode analysis imaging. The component shown in panel (a) has about twice the amplitude ( $\|\mathbf{v}_{\text{terrestrial}}\|$ ) of those in panels (b) and (c), and for all three components,  $\|\mathbf{B}^*\mathbf{v}_{\text{terrestrial}}\| / (\|\mathbf{B}\| \|\mathbf{v}_{\text{terrestrial}}\|) \sim 0.035$ .

The Owens Valley is an important source of water and power for the city of Los Angeles. Unfortunately, this means that high-voltage power lines run along the valley  $\gtrsim 10$  km to the west of the OVRO-LWA. Some of these power-line poles have faulty insulators that arc and produce pulsed, broadband RFI. Because these poles exist in the near-field of the array, we have been able to localize some of them by using the curvature of the incoming wavefront to infer a distance. Efforts are currently underway to work with the utility pole owners to have these insulators replaced.

In the meantime, it is possible to suppress their contamination in the data set. The contribution of these RFI sources to the visibilities can be plainly seen by averaging  $> 24$  hours of data with the phase center set to zenith. In this way, true sky components are smeared along tracks of constant declination while terrestrial sources (i.e., the arcing power lines or any contribution due to common-mode pickup) are not smeared. Obtaining a model for the RFI is complicated by the fact that the

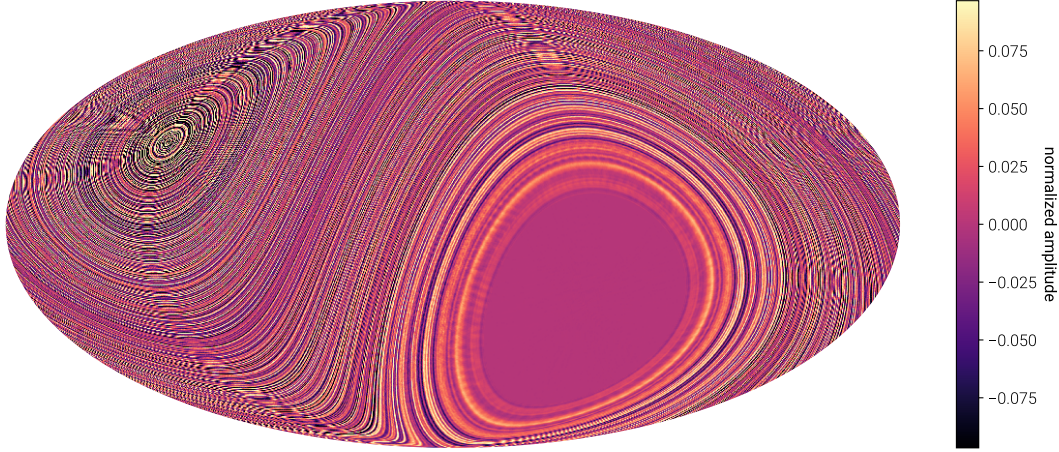


Figure 3.18: A Mollweide-projected image of the artifacts introduced to the  $m$ -mode analysis maps by the three terrestrial sources shown in Figure 3.17. Because these sources are not moving through the sky sidereally, they tend to be smeared along rings of constant declination. The spurs seemingly radiating from the NCP are a Moiré pattern (i.e., an artifact of the pixelization).

contaminating sources are at extremely low elevations, where the antenna response is essentially unknown (and inhomogeneous due to antenna shadowing effects). It is not enough to know the physical location of the faulty insulator generating the RFI. In addition, we must know the response of each antenna (amplitude and phase) in the appropriate direction. This motivates the use of peeling, which allows the antenna response to be a free parameter. Therefore, model visibilities for the RFI can be obtained by peeling the sources after smearing the visibilities over  $> 24$  hours. Figure 3.17 shows an illustration of some of the removed components at 62.688 MHz.

While attempting to peel RFI sources from the averaged visibilities, it was discovered that frequently peeling would remove components from the visibilities that are not obviously associated with any source on the horizon or elsewhere in the sky (see panels (a) and (b) in Figure 3.17). These components appear noise-like in the images, but they are actually a constant offset to the measured visibilities and are therefore likely associated with cross-talk or some form of common-mode pickup. If these components are not subtracted from the measured visibilities, they contribute ringlike structures to the sky maps, as seen in Figure 3.18. This figure is not a simulation but rather a difference between maps created before and after measuring and subtracting the components in Figure 3.17 from each integration.

The first step in Equation 3.9 is to compute  $\mathbf{B}^*\mathbf{v}$ . In this step, we compute the

projection of the measurement  $\mathbf{v}$  onto the space spanned by the columns of  $\mathbf{B}$ . Each column of  $\mathbf{B}$  describes the interferometer’s response to a corresponding spherical harmonic coefficient of the sky-brightness distribution. Therefore, the act of computing  $\mathbf{B}^*\mathbf{v}$  is to project the measured  $m$ -modes onto the space of  $m$ -modes that could be generated by astronomical sources. The degree to which a source of terrestrial interference will contaminate a map generated using  $m$ -mode analysis imaging is determined by its amplitude after projection.

For instance, a bright interfering source might contribute  $\mathbf{v}_{\text{terrestrial}}$  to the measured  $m$ -modes. However, if  $\mathbf{v}_{\text{terrestrial}}$  is actually perpendicular to all of the columns of  $\mathbf{B}$ , there will be no contamination in the map because  $\mathbf{B}^*\mathbf{v}_{\text{terrestrial}} = \mathbf{0}$ . In practice, this is unlikely. In general, the contamination is proportional to the overall amplitude of the interference ( $\|\mathbf{v}_{\text{terrestrial}}\|$ ) and the degree to which the interference mimics an astronomical signal ( $\|\mathbf{B}^*\mathbf{v}_{\text{terrestrial}}\| / (\|\mathbf{B}\| \|\mathbf{v}_{\text{terrestrial}}\|)$ ).

These terrestrial sources do not rotate with the sky, and hence their contamination tends to be restricted to modes with small  $m$ . In this data set the contamination is largely restricted to  $m \lesssim 1$ . Although the RFI is capable of fluctuating on short timescales, in this case, the artifacts it introduces seem to be restricted to small  $m$  (presumably because the phase is not fluctuating). As a result, if the contamination is not suppressed, it will manifest itself as rings along stripes of constant declination. This effect is plainly visible in Figure 3.17. Because of the distinctive ringlike pattern created by terrestrial sources, we additionally chose to discard spherical harmonics with either  $m = 0$  or  $m = 1$  and  $l > 100$  in order to further suppress the contamination.

### 3.6 Conclusion

In this work, we presented a new imaging technique – Tikhonov-regularized  $m$ -mode analysis imaging and CLEANing – for drift-scanning telescopes like the OVRO-LWA. This technique exactly corrects for wide-field effects in interferometric imaging with a single synthesis imaging step. We applied Tikhonov-regularized  $m$ -mode analysis imaging to a 28 hour data set and generated eight sky maps between 36.528 and 73.152 MHz. These sky maps are a substantial improvement in angular resolution over existing maps at these frequencies with  $\sim 15'$  angular resolution and  $< 600$  K thermal noise. The point-source flux scale is consistent with that defined by Scaife & Heald (2012) to about 5%, and large angular scales are consistent with the work of Dowell et al. (2017) to within 20%.

At frequencies above  $\sim 55$  MHz, the angular resolution of these maps is limited by the selection of  $l_{\max} = 1000$ . Future work will increase  $l_{\max}$  to remove this restriction, as well as include more time and bandwidth to improve the thermal noise. The usage of nighttime-only data can help mitigate dynamic range limitations from the ionosphere and also eliminate solar sidelobe residuals. Observations could also be extended to slightly higher and lower frequencies ( $\sim 27$  to  $85$  MHz) to take advantage of the full frequency range of the OVRO-LWA. The higher frequencies are particularly interesting in order to maximize the overlap with the MWA in the southern hemisphere, which could be used to fill in the hole around the southern celestial pole.

These maps and future improvements are primarily intended to be used as part of a foreground modeling and subtraction routine for 21 cm cosmology experiments. Each map will be made publicly available on LAMBDA.

### **Acknowledgments**

This work is dedicated to the memory of Professor Marjorie Corcoran, who was an influential mentor to MWE.

This material is based in part upon work supported by the National Science Foundation under grants AST-1654815 and AST-1212226. The OVRO-LWA project was initiated through the kind donation of Deborah Castleman and Harold Rosen.

Part of this research was carried out at the Jet Propulsion Laboratory, California Institute of Technology, under a contract with the National Aeronautics and Space Administration, including partial funding through the President's and Director's Fund Program.

This work has benefited from open-source technology shared by the Collaboration for Astronomy Signal Processing and Electronics Research (CASPER). We thank the Xilinx University Program for donations; NVIDIA for proprietary tools, discounts, and donations; and Digicom for collaboration on the manufacture and testing of DSP processors.

We thank the Smithsonian Astrophysical Observatory Submillimeter Receiver Lab for the collaboration of its members.

Development, adaptation, and operation of the LEDA real-time digital signal-processing systems at OVRO-LWA have been supported in part by NSF grants AST/1106059, PHY/0835713, and OIA/1125087.

GBT, JD, and FKS acknowledge support from the National Science Foundation under grant AST-1139974.

## Bibliography

- Ali, Z. S., Parsons, A. R., Zheng, H., et al. 2015, *ApJ*, 809, 61
- Alvarez, H., Aparici, J., May, J., & Olmos, F. 1997, *A&AS*, 124, 205
- Baars, J. W. M., Genzel, R., Pauliny-Toth, I. I. K., & Witzel, A. 1977, *A&A*, 61, 99
- Beardsley, A. P., Hazelton, B. J., Sullivan, I. S., et al. 2016, *ApJ*, 833, 102
- Berger, P., Oppermann, N., Pen, U.-L., & Shaw, J. R. 2016, ArXiv e-prints, arXiv:1612.03255
- Bezanson, J., Edelman, A., Karpinski, S., & Shah, V. B. 2017, *SIAM Review*, 59, 65. <http://dx.doi.org/10.1137/141000671>
- Bhatnagar, S., Rau, U., & Golap, K. 2013, *ApJ*, 770, 91
- Bowman, J. D., Rogers, A. E. E., Monsalve, R. A., Mozdzen, T. J., & Mahesh, N. 2018, *Nature*, 555, 67
- Briggs, D. S. 1995, phdthesis, The New Mexico Institute of Mining and Technology
- Chapman, E., Abdalla, F. B., Bobin, J., et al. 2013, *MNRAS*, 429, 165
- Cornwell, T. J., Golap, K., & Bhatnagar, S. 2008, *IEEE Journal of Selected Topics in Signal Processing*, 2, 647
- de Oliveira-Costa, A., Tegmark, M., Gaensler, B. M., et al. 2008, *MNRAS*, 388, 247
- DeBoer, D. R., Parsons, A. R., Aguirre, J. E., et al. 2017, *PASP*, 129, 045001
- Dowell, J., Taylor, G. B., Schinzel, F. K., Kassim, N. E., & Stovall, K. 2017, *MNRAS*, 469, 4537
- Ewall-Wice, A., Dillon, J. S., Hewitt, J. N., et al. 2016, *MNRAS*, 460, 4320
- Fialkov, A., Barkana, R., Pinhas, A., & Visbal, E. 2014, *MNRAS*, 437, L36
- Furlanetto, S. R., Oh, S. P., & Briggs, F. H. 2006, *Phys. Rep.*, 433, 181
- Greig, B., & Mesinger, A. 2015, *MNRAS*, 449, 4246
- Guzmán, A. E., May, J., Alvarez, H., & Maeda, K. 2011, *A&A*, 525, A138
- Górski, K. M., Hivon, E., Banday, A. J., et al. 2005, *ApJ*, 622, 759

- Hallinan, G., et al. in prep.
- Haslam, C. G. T., Klein, U., Salter, C. J., et al. 1981, A&A, 100, 209
- Haslam, C. G. T., Salter, C. J., Stoffel, H., & Wilson, W. E. 1982, A&AS, 47, 1
- Heald, G. H., Pizzo, R. F., Orrú, E., et al. 2015, A&A, 582, A123
- Helmboldt, J. F., & Kassim, N. E. 2009, AJ, 138, 838
- Högbom, J. A. 1974, A&AS, 15, 417
- Iijima, B. A., Harris, I. L., Ho, C. M., et al. 1999, Journal of Atmospheric and Solar-Terrestrial Physics, 61, 1205
- Intema, H. T., Jagannathan, P., Mooley, K. P., & Frail, D. A. 2017, A&A, 598, A78
- Johnson, S. G. 2008, The NLopt nonlinear-optimization package, <http://ab-initio.mit.edu/nlopt>, ,
- Kassim, N. E., Lazio, T. J. W., Erickson, W. C., et al. 2007, ApJS, 172, 686
- Kintner, Jr., P. M., Coster, A. J., Fuller-Rowell, T., et al. 2008, Washington DC American Geophysical Union Geophysical Monograph Series, 181, doi:10.1029/GM181
- Kocz, J., Greenhill, L. J., Barsdell, B. R., et al. 2015, Journal of Astronomical Instrumentation, 4, 1550003
- Lane, W. M., Cotton, W. D., van Velzen, S., et al. 2014, MNRAS, 440, 327
- Lenc, E., Gaensler, B. M., Sun, X. H., et al. 2016, ApJ, 830, 38
- Maeda, K., Alvarez, H., Aparici, J., May, J., & Reich, P. 1999, A&AS, 140, 145
- Mevius, M., van der Tol, S., Pandey, V. N., et al. 2016, Radio Science, 51, 927
- Mitchell, D. A., Greenhill, L. J., Wayth, R. B., et al. 2008, IEEE Journal of Selected Topics in Signal Processing, 2, 707
- Monsalve, R. A., Rogers, A. E. E., Bowman, J. D., & Mozdzen, T. J. 2017, ApJ, 847, 64
- Mozdzen, T. J., Bowman, J. D., Monsalve, R. A., & Rogers, A. E. E. 2017, MNRAS, 464, 4995
- Obenberger, K. S., Taylor, G. B., Hartman, J. M., et al. 2015, Journal of Astronomical Instrumentation, 4, 1550004
- Offringa, A. R., McKinley, B., Hurley-Walker, N., et al. 2014, MNRAS, 444, 606
- Parsons, A. R., Pober, J. C., Aguirre, J. E., et al. 2012, ApJ, 756, 165

- Patil, A. H., Yatawatta, S., Koopmans, L. V. E., et al. 2017, *ApJ*, 838, 65
- Perley, R. A., & Butler, B. J. 2017, *ApJS*, 230, 7
- Pober, J. C., Parsons, A. R., Jacobs, D. C., et al. 2012, *AJ*, 143, 53
- Price, D. C., Greenhill, L. J., Fialkov, A., et al. 2018, *MNRAS*, 478, 4193
- Pritchard, J. R., & Loeb, A. 2012, *Reports on Progress in Physics*, 75, 086901
- Refregier, A. 2003, *MNRAS*, 338, 35
- Remazeilles, M., Dickinson, C., Banday, A. J., Bigot-Sazy, M.-A., & Ghosh, T. 2015, *MNRAS*, 451, 4311
- Rowan, T. 1990, phdthesis, Department of Computer Sciences, University of Texas at Austin
- Salvini, S., & Wijnholds, S. J. 2014, *A&A*, 571, A97
- Scaife, A. M. M., & Heald, G. H. 2012, *MNRAS*, 423, L30
- Shaw, J. R. 2016, private communication, ,
- Shaw, J. R., Sigurdson, K., Pen, U.-L., Stebbins, A., & Sitwell, M. 2014, *ApJ*, 781, 57
- Shaw, J. R., Sigurdson, K., Sitwell, M., Stebbins, A., & Pen, U.-L. 2015, *Phys. Rev. D*, 91, 083514
- Singh, S., Subrahmanyam, R., Udaya Shankar, N., et al. 2017, *ApJ*, 845, L12
- Smirnov, O. M., & Tasse, C. 2015, *MNRAS*, 449, 2668
- Sokolowski, M., Tremblay, S. E., Wayth, R. B., et al. 2015, *PASA*, 32, e004
- Thompson, A. R., Moran, J. M., & Swenson, Jr., G. W. 2001, *Interferometry and Synthesis in Radio Astronomy*, 2nd Edition
- Turtle, A. J., Pugh, J. F., Kenderdine, S., & Pauliny-Toth, I. I. K. 1962, *MNRAS*, 124, 297
- Vedantham, H. K., & Koopmans, L. V. E. 2015, *MNRAS*, 453, 925
- Venumadhav, T., Chang, T.-C., Doré, O., & Hirata, C. M. 2016, *ApJ*, 826, 116
- Voytek, T. C., Natarajan, A., Jáuregui García, J. M., Peterson, J. B., & López-Cruz, O. 2014, *ApJ*, 782, L9
- Wayth, R. B., Lenc, E., Bell, M. E., et al. 2015, *PASA*, 32, e025
- Zheng, H., Tegmark, M., Dillon, J. S., et al. 2017a, *MNRAS*, 464, 3486
- . 2017b, *MNRAS*, 465, 2901

## Chapter 4

# THE 21 CM POWER SPECTRUM FROM THE COSMIC DAWN: FIRST RESULTS FROM THE OVRO-LWA

### **Abstract**

The 21 cm transition of neutral hydrogen is opening an observational window into the cosmic dawn of the universe—the epoch of first star formation ( $z \sim 20$ ). We use 28 hr of data from the Owens Valley Radio Observatory Long Wavelength Array (OVRO-LWA) to place upper limits on the spatial power spectrum of 21 cm emission at  $z \approx 18.4$  ( $\Delta_{21} \lesssim 10^4$  mK). In the process we demonstrate the first application of the double Karhunen-Loëve transform for foreground filtering, and diagnose the systematic errors that are currently limiting the measurement. We also provide an updated model for the angular power spectrum of low-frequency foreground emission measured from the northern hemisphere, which can be used to refine sensitivity forecasts for next-generation experiments.

### **4.1 Introduction**

The Cosmic Dawn of star formation in the universe is one of the final unexplored epochs of the universe. During this time (very roughly  $25 \gtrsim z \gtrsim 15$ ) the first generation of stars and galaxies formed and brought an end to the Dark Ages. Ly $\alpha$  emission from this early star formation couples the excitation temperature of the 21 cm hyperfine structure transition (i.e., the spin temperature) to the local gas temperature of the Intergalactic Medium (IGM; Wouthuysen, 1952; Field, 1958). This allows the highly-redshifted 21 cm transition to be used as a probe of the density, temperature, and ionization state of the IGM (e.g., Furlanetto et al., 2006; Pritchard & Loeb, 2012).

The first detection of high-redshift ( $z \sim 17$ ) atomic hydrogen in the globally averaged sky temperature was recently reported by the EDGES experiment at 78 MHz (Bowman et al., 2018). This measurement was remarkable for its extreme amplitude ( $\sim 500$  mK). A plethora of new ideas have been proposed to explain the amplitude of the absorption trough. These new theories generally fall into two categories: those that invoke new physics to cool the IGM at a rate faster than pure adiabatic cooling would otherwise allow (e.g., Barkana, 2018; Fialkov et al., 2018), and those that posit a new radio background originating from  $z \gtrsim 20$  (e.g. Ewall-Wice et al., 2018;

Dowell & Taylor, 2018). Distinguishing between these alternatives, and confirming the existing measurement now motivates a number of experiments.

The LEDA (Price et al., 2018) and SARAS 2 (Singh et al., 2018) experiments are in the process of attempting to directly confirm the EDGES detection in the global sky temperature using radiometric dipole antennas. Notably, each of these experiments employ materially different antenna designs, which will, in principle, help address concerns regarding the role of the antenna beam and its potential to introduce spectral structure into the measurement. As noted by Bowman et al. (2018), these independent measurements with independent processing pipelines will be an important verification of an exceptionally difficult measurement. The primary observing challenge faced by global-detection experiments—such as EDGES, LEDA, and SARAS 2—is controlling systematic errors introduced by foreground radio emission, instrumental effects, and the interaction between them. Although these experiments calibrate their antennas and electronics with great care, they must rely on external models of the foreground radio emission to model many types of systematic errors.

In contrast, interferometers generally have the ability to self-calibrate and build self-consistent models for the sky emission (e.g., Eastwood et al., 2018). However, interferometers are generally not used to measure the globally averaged sky brightness (Venumadhav et al., 2016), but instead measure the three dimensional spatial power spectrum of the 21 cm brightness temperature fluctuations. The global average and the spatial power spectrum are both statistics of the same field and therefore a measurement of the spatial power spectrum can also provide evidence to support or reject a putative detection in the global average. A detection of the spatial power spectrum will provide independent constraints on the temperature of the IGM and the timing of early star and galaxy formation (e.g., Greig & Mesinger, 2017). Additionally, the spatial power spectrum carries additional information about the scale of the brightness temperature fluctuations, which may be used to constrain, for example, the amplitude of Lyman–Werner feedback (Fialkov et al., 2013) and the spectral hardness of early X-ray sources (Fialkov et al., 2014) that heat the IGM.

At lower redshifts corresponding to the Epoch of Reionization (EoR), constraints on the 21 cm spatial power spectrum have been published by the PAPER experiment (Ali et al., 2015), LOFAR (Patil et al., 2017), the MWA (Beardsley et al., 2016), and the GMRT (Paciga et al., 2013). At redshifts corresponding to the cosmic dawn, this measurement has only been previously attempted by Ewall-Wice et al. (2016) using

6 hr of data from the MWA. The under-construction HERA experiment will aim to place the most sensitive limits to date on the 21 cm brightness temperature spatial power spectrum from both the EoR and Cosmic Dawn due to its large collecting area and design lessons inherited from the PAPER experiment (DeBoer et al., 2017).

In this paper we attempt to measure the spatial power spectrum of 21 cm brightness temperature fluctuations with the OVRO-LWA. In the process we model, derive, and (where appropriate) measure the contribution of thermal noise, foreground emission, and the 21 cm signal to the full covariance matrix of the data. This is possible due to the application of *m*-mode analysis (Shaw et al., 2014, 2015), which introduces sparsity into the covariance matrices without which it would not be possible to store the full covariance matrix of the data.

In §4.2 we describe the observations, the calibration strategy, and point source removal routines used in this work. In §4.3 we will describe the *m*-mode analysis formalism and a new strategy for compressing the representation of the transfer matrix. In §4.4 we derive, model, and measure the contribution of noise, foreground emission and the cosmological 21 cm signal to the full covariance matrix of the measured data. These covariance matrices are applied to filter the foreground emission in §4.5, where we also build physical intuition for the action of the foreground filters derived by (Shaw et al., 2014, 2015). These foreground filters are applied to 28 hr of data from the OVRO-LWA to estimate the 21 cm power spectrum in §4.6, where we also analyze the limiting systematic errors in our measurement. Finally, in §4.7 we present our conclusions. Unless state otherwise, we adopt the set of cosmological parameters measured by Planck Collaboration et al. (2016).

## 4.2 Observations

We collected 28 hr of continuous data using the OVRO-LWA beginning at 2017 February 17 12:00:00 UTC. The OVRO-LWA is a low-frequency radio interferometer with a bandpass covering 27–85 MHz ( $50 \gtrsim z \gtrsim 16$ ), and is currently composed of 288 dual-polarization dipole antennas. 251 of these antennas are arranged within a dense 200 m diameter core in a configuration optimized for sidelobe levels in snapshot images. 32 additional expansion antennas are placed outside of the core, expanding the maximum baseline length to 1.5 km. The remaining five antennas are equipped with radiometric front-ends for total power measurements of the sky as part of the Large-Aperture Experiment to Detect the Dark Ages (LEDA; Price et al., 2018). The LEDA correlator serves as the back-end for the OVRO-LWA, and cross-

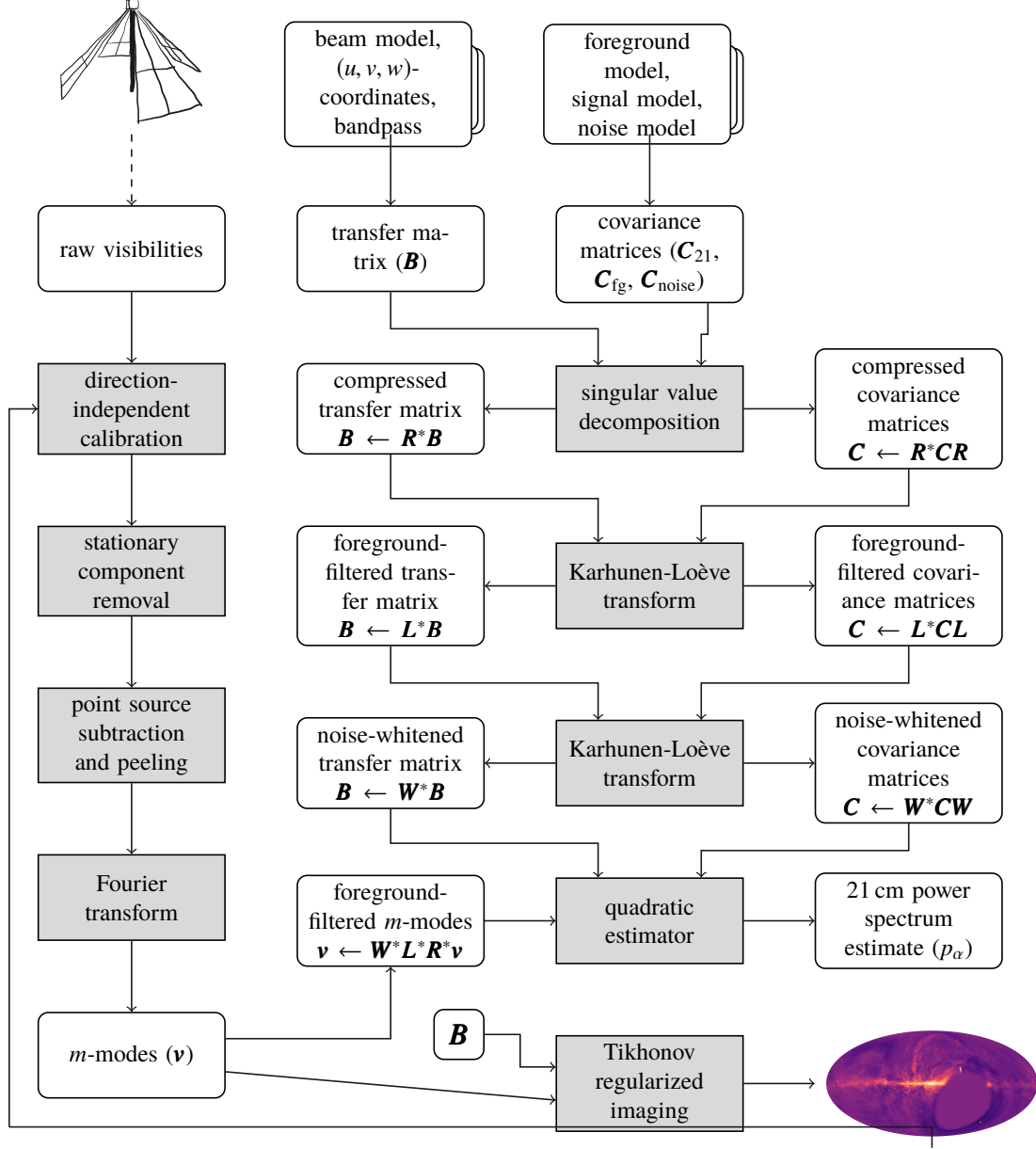


Figure 4.1: A flow chart describing the data analysis steps performed in this paper. Radio waves are received by antennas (depicted in the upper-left corner), which are correlated to produce raw visibilities. These visibilities are then flagged, calibrated, and bright point sources are removed. After a full sidereal day's worth of data has been collected, these visibilities can be Fourier transformed to compute the measured  $m$ -modes. Separately, an empirical beam model is used to calculate the transfer matrix elements that describe the interferometer's sensitivity to the sky. Full covariance matrices are computed for the foreground emission, 21 cm signal, and thermal noise. These matrices are used to compress, filter foreground emission, and whiten the noise covariance. Finally, the resulting filtered  $m$ -modes are used to estimate the spatial power spectrum of 21 cm emission. Images of the sky can be constructed through the use of Tikhonov-regularized imaging (Eastwood et al., 2018), which are useful for diagnosing errors in the analysis.

correlates 512 inputs with 58 MHz instantaneous bandwidth. In this configuration the OVRO-LWA performs full cross-correlation of 256 antennas (512 signal paths), and 32 antennas (64 signal paths) are unused. We selected the correlator’s integration time to be 13 s due to the fact that this selection evenly divides the sidereal day to within 0.1 s. In snapshot images, the OVRO-LWA can capture the entire visible hemisphere at 10' resolution (e.g., Anderson et al., 2017), and this same dataset was used to generate maps of the sky north of  $\delta = -30^\circ$  (Eastwood et al., 2018).

At low radio frequencies, propagation effects through the ionosphere are important. During this observing period, however, geomagnetic and ionospheric conditions were mild. At 73 MHz, bright point sources were observed to refract by up to 4' as waves propagated through the line of sight on. Similarly at 73 MHz, the apparent flux of point sources varied by up to 10% on 13 s timescales due to ionospheric conditions.

In this work we selected data from an instrumental subband centered at 73.152 MHz with 2.6 MHz bandwidth ( $z = 18.4$ ,  $\Delta z = 0.8$ ). This subband is contained within the absorption feature observed by Bowman et al. (2018), and contains the 73.0–74.6 MHz band allocated for radio astronomy in the United States. There is additionally a gap in television broadcasting between 72 MHz (the upper edge of channel 4) and 76 MHz (the lower edge of channel 5) that this observing band takes advantage of. Additionally, in previous work we published an updated low-frequency sky map at 73.152 MHz (Eastwood et al., 2018) that is available online at the Legacy Archive for Microwave Background Data Analysis (LAMBDA).

When measuring the power spectrum of 21 cm fluctuations, it is common to make an implicit assumption that 21 cm power spectrum is not evolving along the line-of-sight direction (see Appendix .1). Greig & Mesinger (2018) simulated this effect and found that for volumes of equal comoving radial distance, this light-cone effect is more severe during the Cosmic Dawn than during the EoR. Near  $z \sim 18$  and a volume with  $\Delta z \sim 3$ , the recovered spatial power spectrum is suppressed by a factor  $\lesssim 2$ . While the light-cone effect can limit the usable bandwidth for estimating the 21 cm spatial power spectrum, we conclude that 2.6 MHz of bandwidth is permissible for this initial analysis. Future studies of 21 cm fluctuations of the Cosmic Dawn, however, should instead consider estimating the multi-frequency angular power spectrum (Datta et al., 2007), which is a statistic that is less common in the literature, but can be measured without assuming that the statistics of the fluctuations are not evolving along the line of sight.

A summary of the analysis steps performed in this work—including the instrumental calibration and 21 cm power spectrum reduction—can be seen in Figure 4.1. In particular, a gain calibration was derived from a 45 minute track of data beginning at 2017 February 17 17:46:28 during which the two brightest point sources in the northern hemisphere (Cyg A and Cas A) are near the meridian. The sky model is initially composed of Cyg A and Cas A where the absolute spectrum of Cyg A is given by Baars et al. (1977), and the spectrum of Cas A is adjusted for its secular decrease of 0.77% per year (Helmboldt & Kassim, 2009). Because this initial sky model is incomplete on large angular scales, baselines shorter than 15 wavelengths are excluded from the calibration routine. The gains are optimized using a variant of alternating least squares independently described by Mitchell et al. (2008) and Salvini & Wijnholds (2014). The bandpass amplitude is fit with a 5th order polynomial, and the phase is fit with a term for the delay and a term for dispersion through the ionosphere. Smoothing the gain calibration in this way helps to avoid modeling errors during calibration propagating into bandpass errors that can limit the sensitivity of the interferometer to the 21 cm power spectrum (Barry et al., 2016; Ewall-Wice et al., 2017). After this initial calibration and source removal, a model of the diffuse galactic emission is constructed using Tikhonov-regularized  $m$ -mode analysis imaging. This model is then used to recalibrate the data with a more complete model of the sky.

The OVRO-LWA analog signal path is susceptible to additive common-mode radio frequency interference (RFI). A model for the common-mode RFI is constructed from the gain-calibrated visibilities after averaging over the entire 28 hr observing period with the phase center left at zenith. Averaging the visibilities in this way smears out the contribution of the sky along characteristic sidereal tracks. We then select the dominant components of the averaged visibilities to be used as templates for the RFI. The templates are manually inspected for residual sky emission by imaging each component with WSCLEAN (Offringa et al., 2014), and checking for features that are swept along sidereal tracks. These templates are scaled and subtracted from each integration to suppress the contamination of the common-mode RFI.

The top panel of Figure 4.2 is a dirty image of the sky constructed from this dataset prior to any point source removal. A handful of bright point sources occupy the northern sky—namely Cas A, Cyg A, Her A, Hya A, Tau A, Vir A, 3C 123, 3C 353, and the Sun. Each of these sources is removed from the visibilities employing a

combination of direction-dependent calibration for the brightest sources, and source fitting and subtraction for the fainter sources. This source removal strategy is described in greater detail by Eastwood et al. (2018).

Finally, in order to reduce the data volume and computational cost of further reductions, we selected only baselines representable with spherical harmonics with multipole number  $l \leq 300$ . This effectively selects only baselines from the core of the OVRO-LWA, which contains the majority of the brightness temperature sensitivity. The data was additionally averaged down to channel widths of 240 kHz. At 73 MHz, this averaging effectively smears out the spatial power spectrum on  $k_{\parallel} \approx 1 \text{ Mpc}^{-1}$  scales, but is permissible because the expected cosmological signal is small on these scales.

### 4.3 Formalism

#### *m*-Mode Analysis

In this paper we apply the *m*-mode analysis formalism developed by Shaw et al. (2014, 2015). The interested reader should consult the aforementioned citations for additional details, but *m*-mode analysis is briefly summarized below.

The measured quantity in a drift-scanning telescope is a periodic function of the sidereal time. The Fourier transform with respect to sidereal time of this measured quantity is called an *m*-mode, where the value of *m* indicates how rapidly this mode varies over the course of a sidereal day.  $m = 0$  corresponds to the mean value of the measurement over a sidereal day.  $m = \pm 1$  corresponds to the components that varies once over a sidereal day. Larger absolute values of *m* represent contributions to the measurement that vary on increasingly rapid timescales.

The primary advantage of making this transformation to *m*-modes is that it can be shown that the set of measured *m*-modes with a given value for *m*, are a linear combination of the spherical harmonic coefficients with the same value of *m*. This allows the data to be partitioned by *m*, and each partition can be manipulated independently of the remaining dataset. Typically this leads to a large reduction in the processing time, which allows for the application of otherwise infeasible data analysis techniques that make use of the full covariance matrix of the dataset.

We will adopt the convention that the measured *m*-modes are contained in a vector  $\mathbf{v}$ , and the spherical harmonic coefficients of the sky brightness are contained in a vector  $\mathbf{a}$ . The transfer matrix  $\mathbf{B}$  describes the interferometer's response to the sky and is block-diagonal when both  $\mathbf{v}$  and  $\mathbf{a}$  are sorted by the absolute value of *m*. If

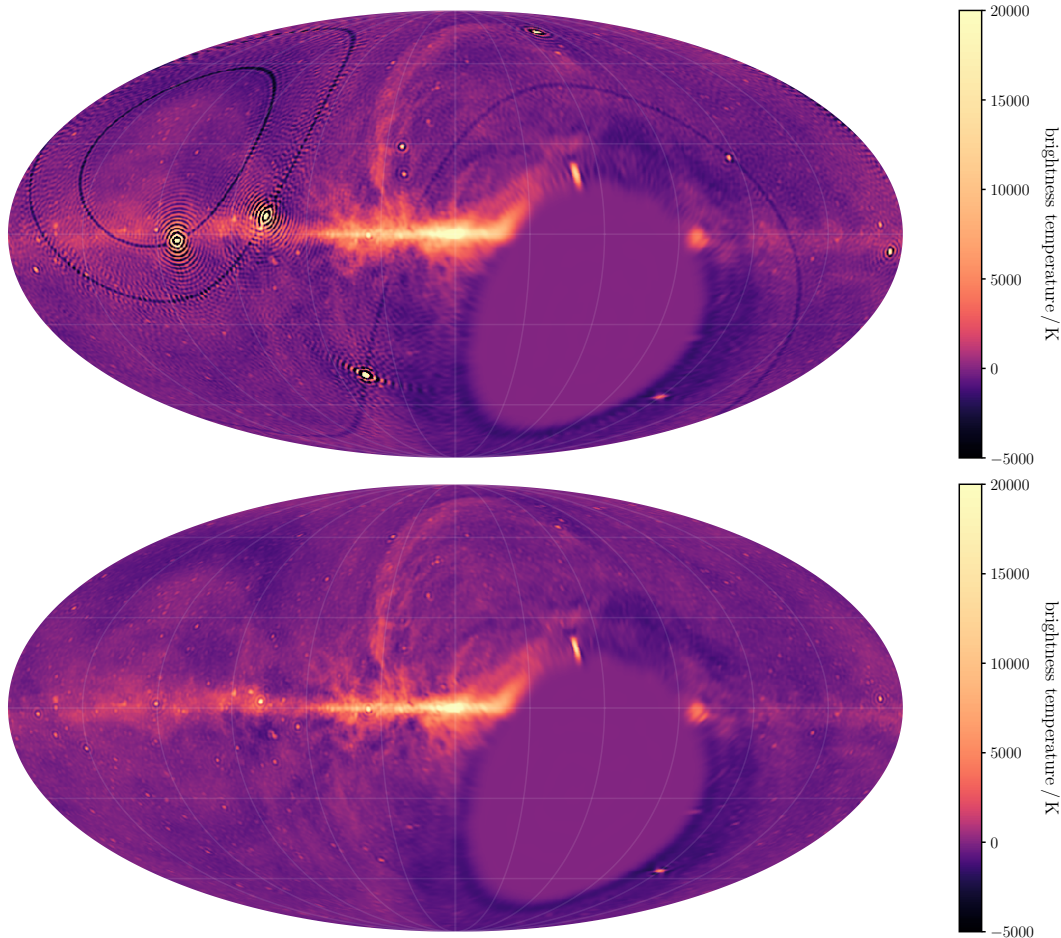


Figure 4.2: A Mollweide projection of a Tikhonov-regularized image of the sky constructed from all baselines representable with  $l_{\max} \leq 200$ , and 2.6 MHz of bandwidth centered on 73.2 MHz. The color scale is linear between  $-1000$  K and  $+1000$  K, and logarithmic outside of this range. No cleaning has been performed, so all point sources are convolved with a point spread function, and no masking of low declinations has been performed. The resolution of the maps naturally degrades at low declinations and the regularization scheme naturally encourages the map to be zero below the horizon. Negative rings at the declination of bright point sources are an artifact of the fact that  $m = 0$  modes are filtered from the dataset due to their susceptibility to RFI and common-mode pickup. (top) Before bright point sources are removed from the dataset. (bottom) After point source removal.

we explicitly decompose the sky in terms of the high-redshift 21 cm contribution  $\mathbf{a}_{21}$ , and the foreground radio emission  $\mathbf{a}_{\text{fg}}$ , then

$$\mathbf{v} = \mathbf{B}\mathbf{a}_{21} + \mathbf{B}\mathbf{a}_{\text{fg}} + \mathbf{n}, \quad (4.1)$$

where  $\mathbf{n}$  is the contribution of thermal noise to the measurement.

The rows of the transfer matrix  $\mathbf{B}$  fundamentally describe the response of each baseline to the sky represented by  $\mathbf{a}$ . The individual elements of the matrix are computed from spherical harmonic transforms of each baseline’s fringe pattern (including the response of the antenna beams and bandpass). Eastwood et al. (2018) demonstrated all-sky imaging in a single synthesis imaging step through inverting Equation 4.1. However, that demonstration was restricted to single channel imaging due to—in part—the computational and storage requirements associated with computing  $\mathbf{B}$ .

### Hierarchical Transfer Matrices

Modern interferometers are composed of large numbers of antennas ( $N \gg 10$ ) arranged in configurations that have both long and short baselines. For instance, the OVRO-LWA has over 30,000 baselines. The shortest baseline is 5 m, and the longest baseline is 1.5 km. Consequently the OVRO-LWA measures a large range of angular scales. We can exploit this fact to reduce the computer time and disk space required to compute and store the transfer matrix  $\mathbf{B}$ .

The sensitivity of a baseline of length  $b$  to spherical harmonic coefficients with multipole moment  $l$  is  $\propto j_l(2\pi b/\lambda)$ , where  $j_l$  is the spherical Bessel function of the first kind, and  $\lambda$  is the wavelength. When  $l \gtrsim 2\pi b/\lambda$ , the spherical Bessel functions rapidly drop to zero (see Appendix .1 for more details about spherical Bessel functions). Consequently, even though the transfer matrix is block-diagonal, each diagonal block of the transfer matrix can also contain a large number of zero-elements.

Therefore, when the columns and rows of each transfer matrix block  $\mathbf{B}_m$  are sorted by the multipole number  $l$  and baseline length respectively, each block has the

following structure:

$$B_m = \left( \begin{array}{c} l \\ \text{baseline length} \end{array} \right) \quad (4.2)$$

Shaded regions represent elements with nonzero value, whereas unshaded regions represent elements with approximately zero value due to the fact that  $l \gtrsim 2\pi b/\lambda$ . This structure makes it apparent that it is not necessary to store every element of each transfer matrix block. In fact, by partitioning the array into sets of baselines with similar length, one can achieve significant cost savings when computing and storing the transfer matrix elements.

Ultimately, for the OVRO-LWA we achieve a 58% compression of the transfer matrix by not storing elements that are approximately zero.

# Data Compression

Further data compression is desirable because it reduces the computational costs of all following analysis steps. We implement the singular value decomposition (SVD) compression described by (Shaw et al., 2014, 2015). The SVD factorizes a matrix into a unitary matrix  $\mathbf{U}$ , a diagonal matrix  $\Sigma$ , and another unitary matrix  $\mathbf{V}$  such that

$$B = U\Sigma V^*. \quad (4.3)$$

The diagonal elements of  $\Sigma$  are called singular values and, in this case, represent the amplitude of the response of the interferometer to the corresponding singular vectors (i.e., the columns of  $U$ ). The data can therefore be compressed by selecting all singular values above a given threshold and computing

$$R = \begin{pmatrix} & \vdots & \vdots & \\ \cdots & u_i & u_{i+1} & \cdots \\ & \vdots & \vdots & \end{pmatrix} \quad (4.4)$$

$$\mathbf{v}_{\text{compressed}} = \mathbf{R}^* \mathbf{v}, \quad (4.5)$$

where  $\mathbf{u}_i$  is a column of  $\mathbf{U}$  whose singular value passes the threshold, and  $\mathbf{v}$  is the vector of measured  $m$ -modes. The transfer matrix is similarly transformed  $\mathbf{B}_{\text{compressed}} = \mathbf{R}^* \mathbf{B}$ , and covariance matrices become  $\mathbf{C}_{\text{compressed}} = \mathbf{R}^* \mathbf{C} \mathbf{R}$ .

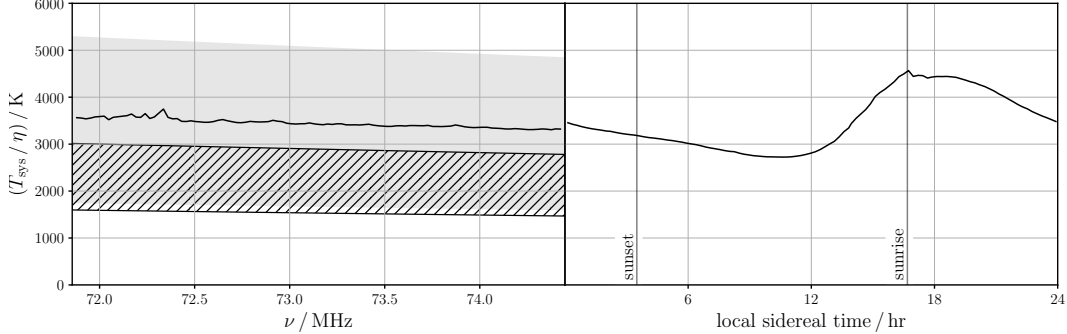


Figure 4.3: The system temperature  $T_{\text{sys}}$  (scaled by the antenna efficiency  $\eta$ ) measured as a function of frequency (left panel, solid black line), and local sidereal time (right panel, solid black line). The hatched region denotes the range of sky temperatures measured by the LEDA experiment (Price et al., 2018). The shaded region denotes the range of sky temperatures measured by the EDGES experiment in the southern hemisphere (Mozdzen et al., 2017).

This compression is especially effective for the OVRO-LWA because the compactness of the interferometer leads to many partial redundancies between similar baselines. This is simply a statement that the number of baselines used in the calculation  $N_{\text{baselines}}$  is larger than the number of unknowns in each transfer matrix block. In this paper, we adopted  $l_{\text{max}} = 300$  as the maximum value of the multipole number. For the OVRO-LWA  $N_{\text{baselines}} \gg 300$ , so there are many redundancies in the dataset even though no pair of baselines is individually redundant. In total this compression reduces the volume of data to a mere 0.6% of its original size (before discarding any singular values).

#### 4.4 Covariance Matrices

We model the covariance of the observations  $\mathbf{C} = \langle \mathbf{v} \mathbf{v}^* \rangle$  with contributions from thermal noise  $\mathbf{C}_{\text{noise}}$ , foreground emission  $\mathbf{C}_{\text{fg}}$ , and the cosmological 21 cm signal itself  $\mathbf{C}_{21}$

$$\langle \mathbf{v} \mathbf{v}^* \rangle = \mathbf{C} = \mathbf{C}_{21} + \mathbf{C}_{\text{fg}} + \mathbf{C}_{\text{noise}}, \quad (4.6)$$

where this expression implicitly assumes that the sky is an isotropic Gaussian-random field, and that the sky covariance should be understood as an average over realizations of the sky.

We will begin with a detailed description of the models, measurements, and calculations used to compute each of these covariance matrices.

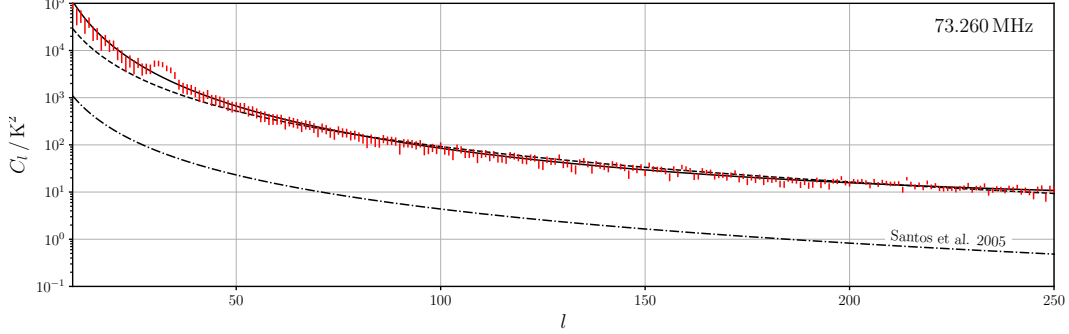


Figure 4.4: The angular power spectrum of the sky as measured by the OVRO-LWA at 73.260 MHz. Measurements (with 95% uncertainty) are indicated with red bars. The uncertainty is dominated by sample variance. The dashed black line is the best-fit power-law spectrum, and the solid black line is the best-fit solution when the power-law index is allowed to run. The dash-dot line is a model derived, in part, from the Haslam 408 MHz sky map (Haslam et al., 1981, 1982; Santos et al., 2005). The feature at  $l \sim 30$  is sensitive to the choice of covariance matrix, and is therefore likely instrumental.

### Thermal Noise Covariance

The 21 cm signal is expected to be unpolarized,<sup>1</sup> so we form Stokes-I visibilities from the mean of the  $xx$  and  $yy$  visibilities. Under this convention, the covariance of the complex-valued Stokes-I visibilities is (Taylor et al., 1999, Chapter 9):

$$\mathbf{C}_{\text{noise}} = \left( \frac{2k_B T_{\text{sys}}}{\eta A_{\text{eff}} \sqrt{2\Delta\nu\tau}} \right)^2 \mathbf{I}, \quad (4.7)$$

where  $k_B$  is the Boltzmann constant,  $T_{\text{sys}}$  is the system temperature,  $\eta$  is the antenna efficiency,  $A_{\text{eff}}$  is the effective collecting area (each assumed to be the same for all antennas),  $\Delta\nu$  is the bandwidth, and  $\tau$  is the total integration time. The effective collecting area of the antenna is related to the solid-angle of the primary beam  $\Omega$  through  $A_{\text{eff}} = \lambda^2/\Omega$ . At 73 MHz, the OVRO-LWA dipoles have primary beams with  $\Omega \sim 2.4 \text{ sr}$  or  $A_{\text{eff}} \sim 7 \text{ m}^2$ .

OVRO-LWA dipoles are designed to be sky-noise dominated ( $\geq 6 \text{ dB}$  between 20–80 MHz; Hicks et al., 2012). More precisely, the system temperature is given by

$$T_{\text{sys}} \approx \eta T_{\text{sky}} + T_{\text{pre-amp}}, \quad (4.8)$$

---

<sup>1</sup> Venumadhav et al. (2017) find that circular polarization may be used to measure primordial magnetic fields, but the amplitude of this effect is too small to consider measuring with existing low-frequency telescopes.

where  $\eta$  is the antenna efficiency,  $T_{\text{sky}}$  is the averaged brightness temperature of the sky (primarily the galactic synchrotron emission) weighted by the primary beam pattern, and  $T_{\text{pre-amp}}$  is the noise temperature of the first amplifier in the analog signal path. We expect  $T_{\text{pre-amp}} \approx 250$  K and  $\eta \lesssim 0.5$  (Hicks et al., 2012).

The LEDA experiment hosted at the OVRO-LWA measured the brightness temperature of the diffuse galactic emission in the northern hemisphere using the five radiometric antennas (Price et al., 2018). At 70 MHz, the brightness temperature varies between 1700 K and 3200 K with a relatively flat spectral index that varies between  $-2.28$  and  $-2.38$ . In the southern hemisphere, the EDGES experiment measured that the brightness temperature of the sky at 150 MHz varies between 257 K and 842 K with a spectral index that varies between  $-2.50$  and  $-2.62$  (Mozdzen et al., 2017). Extrapolating to 70 MHz, we expect the beam-weighted sky brightness temperature in the southern hemisphere to vary between 1700 K and 6200 K. The maximum brightness temperature corresponds to sidereal time when the galactic center transits.

We measured the system temperature as a function of frequency and sidereal time using a five-point stencil to suppress the contribution of the sky emission to the measured visibilities

$$\begin{aligned}\Delta(\nu, t) = & 4V(\nu, t) - V(\nu - 24 \text{ kHz}, t) - V(\nu, t - 13 \text{ s}) \\ & - V(\nu + 24 \text{ kHz}, t) - V(\nu, t + 13 \text{ s}),\end{aligned}$$

where  $\Delta(\nu, t)$  is a quantity whose variance is 20 times larger than that of the measured visibilities  $V(\nu, t)$  at the given frequency  $\nu$  and time  $t$ . Note that 24 kHz is the native frequency resolution of the OVRO-LWA and 13 s is the integration time. Therefore this stencil takes the difference between each measured visibility and the bilinear interpolation from adjacent frequency channels and time integrations. We then estimated the system temperature from the variance of  $\Delta$ . The measured system temperature is shown in Figure 4.3 compared to the sky temperature measured by LEDA and extrapolated from EDGES. As expected, the system temperature increases at lower frequencies due to the increasing sky brightness temperature, and varies sidereally reaching a maximum as the galactic center transits the meridian. These measurements suggest that the antenna efficiency  $\eta \sim 0.25$ . Although the system temperature varies with time and frequency, we adopt a constant system temperature of  $3500\eta$  K when computing the sensitivity of the OVRO-LWA. We expect this approximation to potentially introduce errors of  $\sim 10\%$  to the computed

sensitivity and error bars, which does not materially impact the results presented in this paper.

### Foreground Covariance

Under the assumption of a Gaussian random field, the covariance contributed by the sky can be computed from the multi-frequency angular power spectrum:

$$\langle a_{lm}(\nu) a_{l'm'}^*(\nu') \rangle = C_l(\nu, \nu') \delta_{ll'} \delta_{mm'}, \quad (4.9)$$

where the angled brackets denote an ensemble average over realizations of the sky,  $a_{lm}(\nu)$  is the spherical harmonic coefficient of the sky brightness at frequency  $\nu$ ,  $C_l(\nu, \nu')$  is the multi-frequency angular power spectrum at the multipole moment  $l$ , and between the frequencies  $\nu$  and  $\nu'$ . The Kronecker delta is represented by  $\delta$ . The transfer-matrix  $\mathbf{B}$  describes how to relate the covariance of the spherical harmonic coefficients to the covariance of the measurements themselves, such that

$$\mathbf{C}_{\text{sky}} = \mathbf{B} \mathbf{C}'_{\text{sky}} \mathbf{B}^*, \quad (4.10)$$

where  $\mathbf{C}_{\text{sky}}$  is a term in Equation 4.6, and  $\mathbf{C}'_{\text{sky}}$  is a matrix whose elements are specified by Equation 4.9.

A common parameterization of  $C_l(\nu_1, \nu_2)$  for foreground radio emission is (Santos et al., 2005)

$$C_l^{\text{fg}}(\nu, \nu') = \sum_i A_i \left( \frac{l}{l_0} \right)^{-\alpha_i} \left( \frac{\nu \nu'}{\nu_0^2} \right)^{-\beta_i} \times \exp \left( -\frac{(\log \nu - \log \nu')^2}{2\zeta_i^2} \right), \quad (4.11)$$

where  $A_i$  represents the overall amplitude of a foreground component.  $\alpha_i$  determines its angular spectrum, and  $\beta_i$  determines its frequency spectrum. Finally,  $\zeta_i$  controls the degree to which nearby frequency channels are correlated. The statement that foreground emission is spectrally smooth here implies  $\zeta_i \gg 1$  for each component. This parameterization allows for multiple power-law foreground components and ensures that the covariance matrix is positive definite. Because the fractional bandwidth is small, in this paper we assume  $\zeta_i^2 \gg \log^2(\nu/\nu')$  such that

$$C_l^{\text{fg}}(\nu, \nu') = \sqrt{C_l^{\text{fg}}(\nu) C_l^{\text{fg}}(\nu')}, \quad (4.12)$$

where  $C_l^{\text{fg}}(\nu) = C_l^{\text{fg}}(\nu, \nu)$  is the single-frequency angular power spectrum.

We measured the angular power spectrum of the foreground emission at each frequency channel using a quadratic estimator (Tegmark, 1997). The angular power spectrum is given by

$$C_l^{\text{fg}}(\nu) = [\mathbf{F}^{-1}(\mathbf{q} - \mathbf{b})]_l, \quad (4.13)$$

where  $\mathbf{F}$  is the Fisher information matrix,  $\mathbf{q}$  is a quadratic function of the input data, and  $\mathbf{b}$  is the bias due to thermal noise. The elements of the Fisher matrix  $\mathbf{F}$  are given by

$$F_{ll'} = \sum_m \|\mathbf{b}_{lm}^* \mathbf{C}_m^{-1} \mathbf{b}_{l'm}\|^2, \quad (4.14)$$

where  $F_{ll'}$  is the Fisher matrix element corresponding to the multipole numbers  $l$  and  $l'$ ,  $\mathbf{b}_{lm}$  is the column of the transfer matrix corresponding to  $l$  and the azimuthal quantum number  $m$ , and  $\mathbf{C}_m$  is the covariance matrix block corresponding to  $m$ . The elements of  $\mathbf{q}$  and  $\mathbf{b}$  are given by

$$q_l = \sum_m \|\mathbf{b}_{lm}^* \mathbf{C}_m^{-1} \mathbf{v}_m\|^2 \quad (4.15)$$

$$b_l = \sum_m \|\mathbf{b}_{lm}^* \mathbf{C}_m^{-1} \mathbf{C}_{\text{noise},m}^{1/2}\|^2, \quad (4.16)$$

where  $\mathbf{v}_m$  is the vector of  $m$ -modes corresponding to the given value of  $m$ , and  $\mathbf{C}_{\text{noise},m}$  is the corresponding block of the noise covariance matrix.

The result of applying this quadratic estimator to the dataset at 73.260 MHz (a representative channel) can be seen in Figure 4.4. Broadly, the data can be described with a power law in  $l$ , but the quality of the fit is somewhat poor. A single power-law fit gives

$$C_l \sim 92. \times \left( \frac{l}{100} \right)^{-2.5} \text{ K}^2. \quad (4.17)$$

In fact, while this is a reasonable fit at  $l > 75$ , a shallower power-law index is preferred  $l < 75$ . If we allow for the power-law index to run, the best-fit model becomes:

$$C_l \sim 85. \times \left( \frac{l}{100} \right)^{-3.2+l/277.} \text{ K}^2. \quad (4.18)$$

A comparison of these two models can be seen in Figure 4.4 in addition to a model of the galactic synchrotron emission derived by Santos et al. (2005), which appears to underestimate the amplitude of  $C_l$  by an order of magnitude. Because the fractional bandwidth of this measurement is small, essentially all reasonable spectral indices are permitted. We adopt a fiducial spectral index of  $-2.5$  as a compromise between the spectral indices measured by LEDA and EDGES.

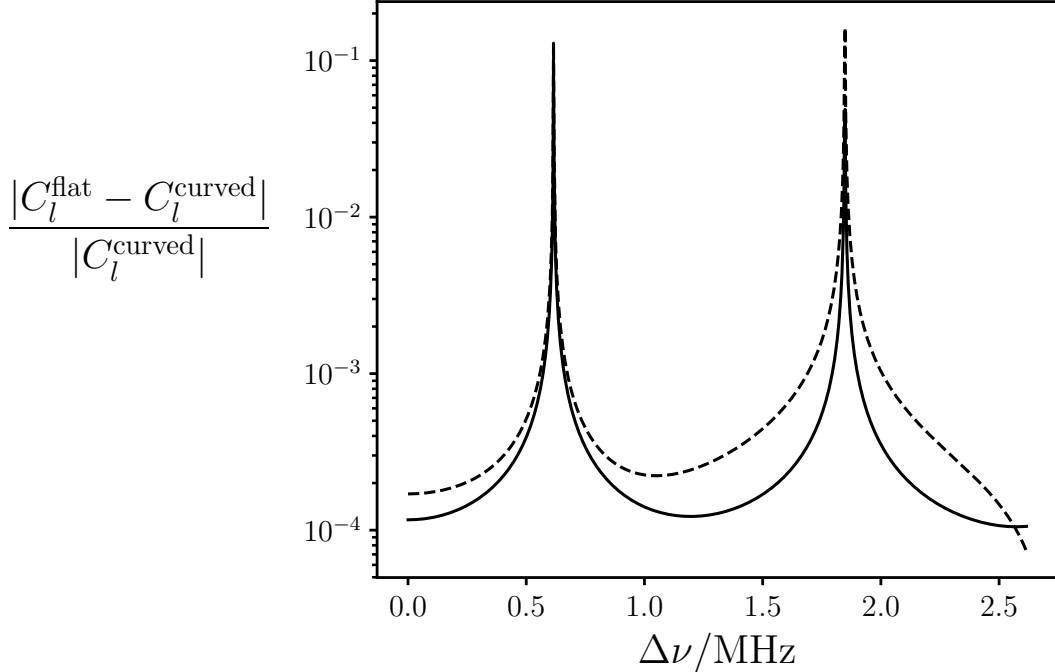


Figure 4.5: The relative error involved with making the flat-sky approximation for a hat function power spectrum (i.e., the relative difference between Equations 4.19 and 4.20) with  $l = 10$  (solid line) and  $l = 100$  (dashed line). The hat function is centered at  $k_{\parallel} = 0.1 \text{ Mpc}^{-1}$  with a domain that extends from  $0.095 \text{ Mpc}^{-1}$  to  $0.105 \text{ Mpc}^{-1}$ . The spikes in relative error correspond to when  $C_l^{\text{curved}}(\Delta\nu) \approx 0$ .

### Signal Covariance

Given the isotropic three-dimensional spatial power spectrum of the 21 cm brightness temperature  $P_z^{21}(k)$  with the wavenumber  $k$  and at the redshift  $z$ , the multi-frequency angular power spectrum  $C_l(\nu, \nu')$  is given by

$$C_l^{21}(\nu, \nu') = \frac{2}{\pi} \int P_z^{21}(k) j_l(kr_z) j_l(kr_{z'}) k^2 dk, \quad (4.19)$$

where  $r_z$  is the comoving distance to the redshift  $z$  (specified by the frequency  $\nu$ ), and  $j_l(x)$  is the spherical Bessel function of the first kind. In the flat-sky approximation, Equation 4.19 can be simplified to

$$C_l^{21}(\nu, \nu') \approx \frac{1}{\pi r_z r_{z'}} \int P_z^{21}(k_{\perp}, k_{\parallel}) \cos(k_{\parallel} \Delta r_z) dk_{\parallel}, \quad (4.20)$$

where  $k_{\perp} = l/r_z$  and  $k_{\parallel} = \sqrt{k^2 - k_{\perp}^2}$ . See Appendix .1 for a derivation of this approximation and the assumptions that must be satisfied for it to be a reasonable approximation.

If  $P_z^{21}(k_\perp, k_\parallel)$  is additionally assumed to be a piece-wise linear function, Equation 4.20 can be evaluated analytically. Under this assumption,  $P_z^{21}(k_\perp, k_\parallel)$  can be represented using linear hat functions (triangular functions in two dimensions), such that

$$P_z^{21}(k_\perp, k_\parallel) = \sum_{\alpha} p_{\alpha} \times \text{hat}_{\alpha}(k_\perp, k_\parallel) \quad (4.21)$$

$$C_l^{21}(\nu, \nu') \approx \frac{1}{\pi r_z r_{z'}} \sum_{\alpha} p_{\alpha} H_{\alpha}(\Delta r_z) \quad (4.22)$$

where  $H_{\alpha}(\Delta r_z) = \int \text{hat}_{\alpha}(k_\perp, k_\parallel) \cos(k_\parallel \Delta r_z) dk_\parallel$ .

The flat-sky approximation is valid only when the power spectrum is smooth enough for rapid oscillations in the spherical Bessel functions to cancel out. The hat functions are non-differentiable, and so we must compute the error associated with this pixelization of the power spectrum. Figure 4.5 gives the relative error on the computed angular power spectrum for a fiducial hat function power spectrum. Generally the error is  $10^{-4}$ , but can reach to  $10^{-1}$  at values where  $C_l \approx 0$ . This is an acceptable error in the context of this paper, but future experiments may wish to experiment with differentiable basis functions.

When selecting a fiducial model for the 21 cm power spectrum we prefer to remain unopinionated, and therefore adopt a flat power spectrum with a single free parameter, the overall amplitude of the dimensionless power spectrum  $\Delta_{21}$ :

$$P_{\text{fiducial}}^{21}(k) = \frac{2\pi^2}{k^3} \Delta_{21}^2. \quad (4.23)$$

Prior to the recent detection of an absorption feature centered at 78 MHz by Bowman et al. (2018), the amplitude of the power spectrum was generally predicted to be  $\Delta_{21} < 20$  mK at  $z \sim 20$  (e.g., Fialkov et al., 2014). However, more recent predictions in the context of the measured 78 MHz absorption feature predict a much brighter power spectrum (e.g. Barkana, 2018; Kaurov et al., 2018). We therefore adopt  $\Delta_{21} = 140$  mK as a fiducial power spectrum amplitude, which assumes that interactions between baryons and dark matter are important for cooling the IGM in the early universe. The amplitude of the fiducial 21 cm signal is primarily used to determine which modes should be kept by the foreground filter described in the following section. Therefore, if the reader is skeptical of this selection of the fiducial 21 cm signal, they may simply choose to interpret the results as if the foreground filter was weaker than expected.

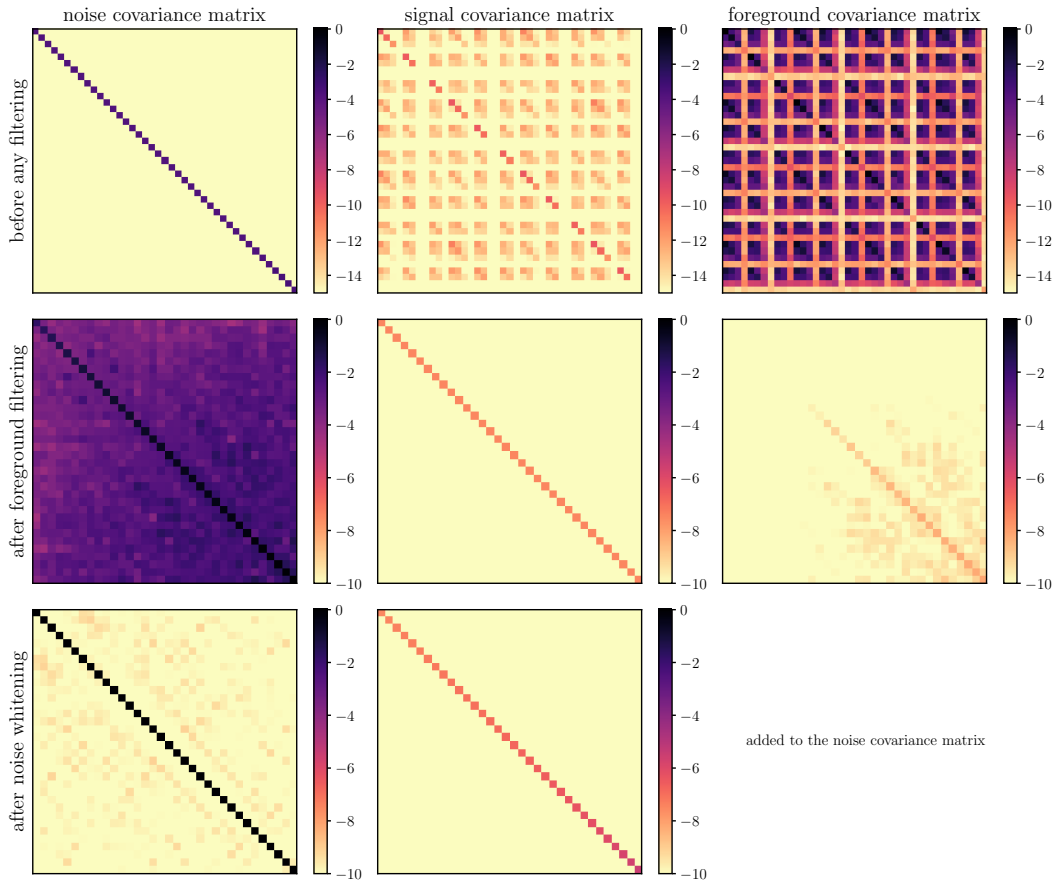


Figure 4.6: Illustration of the action of foreground filtering on each of the covariance matrices discussed in §4.4. The left column corresponds to the noise covariance matrix, the middle column corresponds to the high-redshift 21 cm contribution to the covariance, and the right column corresponds to the foreground covariance matrix. The top row is before any filtering has been applied, the middle row is after the first KL transform, and the bottom row is after the second KL transform.

## 4.5 Foreground Filtering

In the preceding sections, we have derived and—where appropriate—measured the contribution of thermal noise, foreground emission and the cosmological 21 cm emission to the complete covariance matrix of the data. This was possible because the transfer matrix  $\mathbf{B}$  is block-diagonal with respect to  $m$ , and we assumed that the sky emission is a Gaussian-random field (i.e., there are no correlations between different values of  $m$ ). Without these properties the full covariance matrix is generally too large to represent and manipulate on any existing computer. Shaw et al. (2014, 2015) were therefore able to derive a new foreground filtering technique that exploits knowledge of the full covariance matrix. This filter is called the double

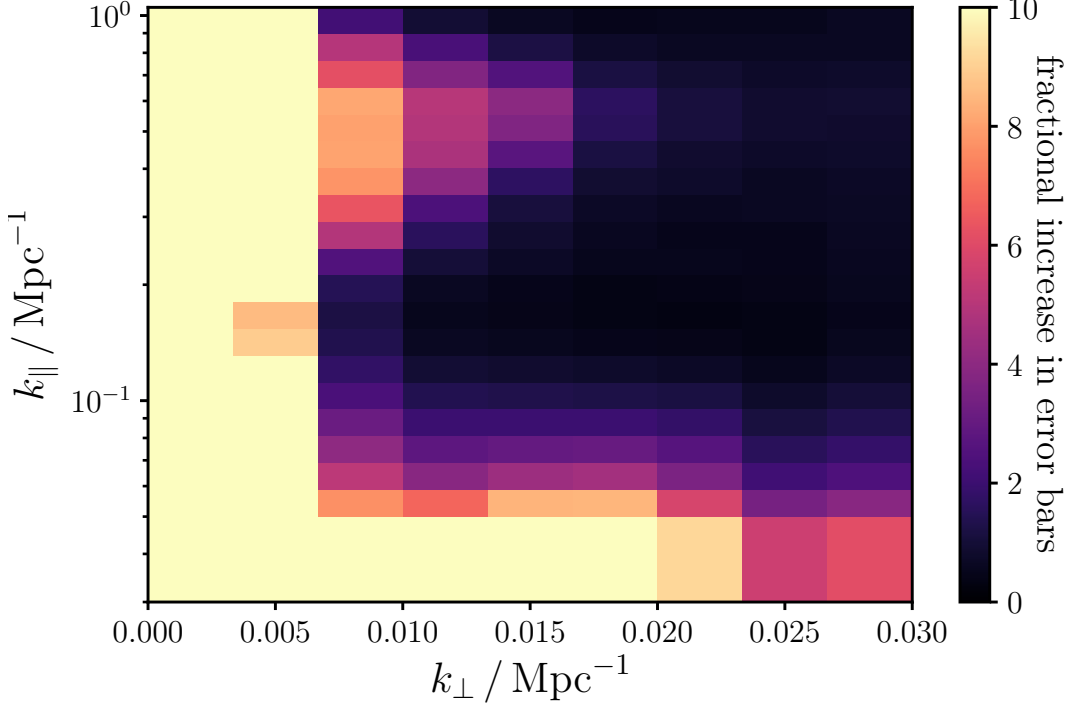


Figure 4.7: The fractional increase in the size of the error bars in each power spectrum bin due to the application of a double KL transform foreground filter (moderate strength).

Karhunen–Loëve transform (double KL transform). In this section we will briefly summarize the action of this foreground filter and demonstrate its application to the OVRO-LWA. We will finally attempt to develop an intuitive understanding by relating its behavior to the “foreground wedge” commonly seen in the literature (e.g., Vedantham et al., 2012; Parsons et al., 2012; Thyagarajan et al., 2015).

The KL transform is closely related to the generalized eigenvalue problem. For two Hermitian, positive definite matrices  $\mathbf{C}_1, \mathbf{C}_2 \in \mathbb{C}^N$ , we would like to find all pairs of eigenvalues  $\lambda_i$  and eigenvectors  $\mathbf{v}_i$  for which

$$\mathbf{C}_1 \mathbf{v}_i = \lambda_i \mathbf{C}_2 \mathbf{v}_i . \quad (4.24)$$

Because both matrices are Hermitian, it quickly follows that the eigenvalues  $\lambda_i$  must be real. Because both matrices are additionally positive definite, it follows that the eigenvalues  $\lambda_i$  must all be positive. Furthermore we can select the normalization of the eigenvectors such that

$$\mathbf{v}_i^* \mathbf{C}_1 \mathbf{v}_i = \lambda_i \quad (4.25)$$

$$\mathbf{v}_i^* \mathbf{C}_2 \mathbf{v}_i = 1 . \quad (4.26)$$

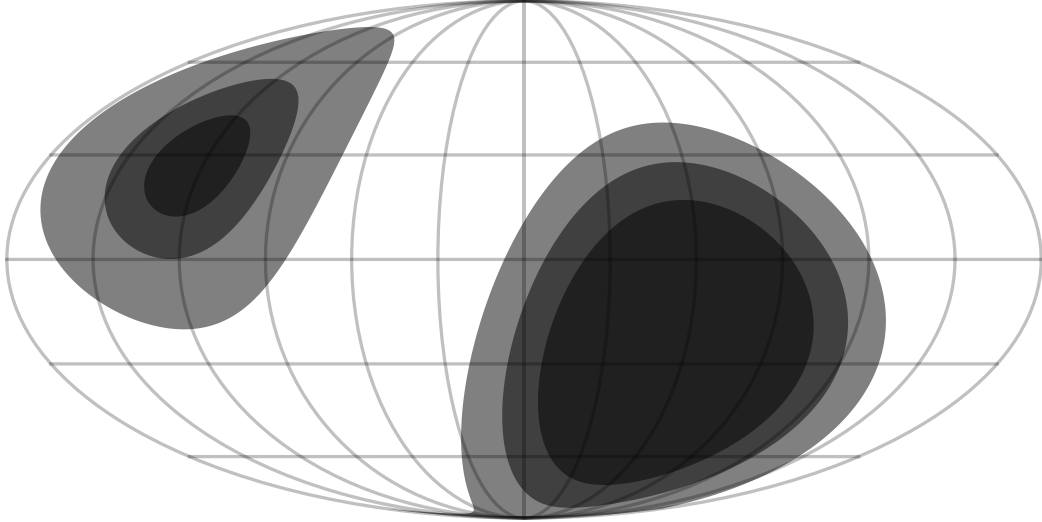


Figure 4.8: Mollweide projected illustration of the sky where shaded regions are down-weighted by the foreground filter. From darkest to lightest, these regions of the sky are filtered by the mild, moderate, and extreme foreground filters respectively.

Under this convention the eigenvalues have a simple interpretation as the ratio of the mode-power contained in  $\mathbf{C}_1$  relative to  $\mathbf{C}_2$ . All  $N$  eigenvalues and eigenvectors can be conveniently found with a single call to LAPACK (Anderson et al., 1990).

In §4.4 we derived and measured a model for the foreground contribution to the data covariance  $\mathbf{C}_{\text{fg}}$ . In §4.4 we projected a fiducial model 21 cm power spectrum to a multi-frequency angular power spectrum, and therefore derived its contribution to the data covariance  $\mathbf{C}_{21}$ . We can solve the generalized eigenvalue problem for the eigenvectors (arranged as columns within the matrix  $\mathbf{L}$ ) that simultaneously diagonalize both matrices (called the KL transform):

$$\mathbf{LC}_{\text{fg}}\mathbf{L}^* = \boldsymbol{\Lambda} \quad (4.27)$$

$$\mathbf{LC}_{21}\mathbf{L}^* = \mathbf{I}, \quad (4.28)$$

where  $\boldsymbol{\Lambda}$  is a diagonal matrix, and  $\mathbf{I}$  is the identity matrix. The foreground filter is simply constructed by selecting only the eigenvectors for which the corresponding eigenvalue (i.e., the foreground–signal power ratio) is less than some value  $\epsilon_{\text{filter}}$  selected by the observer. The application of this filter to a fiducial set of models can be seen in the second row of Figure 4.6. The signal covariance matrix has been diagonalized and the power in each remaining mode is greater than the surviving power in the foreground covariance matrix. The off-diagonal elements in the foreground covariance matrix are due to numerical errors. The possible effect of these

numerical errors on the efficacy of the foreground filter is noted here, but is out of the scope of the current work.

Much emphasis has been placed on maintaining the integrity of the “foreground wedge” in the next generation of 21 cm telescopes. In its simplest form, the existence of the foreground wedge is a statement that most foreground radio emission that observers have to contend with when trying to detect the cosmological 21 cm is spectrally smooth. A simple Fourier transform of an image cube therefore leads to most contamination occupying the space where  $k_{\parallel}$  (the line of sight wavenumber) is small. However, due to the chromatic nature of interferometers (specifically that the fringe spacing  $\propto b/\lambda$  where  $b$  is the baseline length and  $\lambda$  is the wavelength), this contamination is spread out into a wedge-like structure. Additional chromaticity in, for example, the bandpass or antenna primary beam leads to the contamination even leaking out of the wedge. In the event of too much leakage, the observer has lost their ability to measure the cosmological 21 cm transition.

In contrast, the KL transform automatically finds the optimal linear combination of the dataset for separating foregrounds using all available information built into the models. This includes information on the frequency spectrum of the foregrounds as well as their angular structure, which can lead to scenarios where the KL transform can filter foreground emission that cannot be avoided with a delay filter. There is, of course, a caveat that the KL transform requires sufficiently detailed models for the instrument and foreground emission. However, it is not necessarily optimal to remain completely apathetic to the structure of foreground emission, and most collaborations are expending significant effort to characterize their instruments.

A single KL transform, however, leads to large off-diagonal elements in the noise covariance matrix (see the second row of Figure 4.6). Therefore Shaw et al. (2014, 2015) introduced a second KL transform that diagonalizes the noise covariance matrix. This second matrix composed of eigenvectors will be denoted with  $\mathbf{W}$ . In total we therefore have

$$\mathbf{C}_{\text{filtered}} = \underbrace{\mathbf{W}^* \mathbf{L}^* \mathbf{C}_{21} \mathbf{L} \mathbf{W}}_S + \underbrace{\mathbf{W}^* \mathbf{L}^* (\mathbf{C}_{\text{fg}} + \mathbf{C}_{\text{noise}}) \mathbf{L} \mathbf{W}}_I, \quad (4.29)$$

where  $\mathbf{C}_{\text{filtered}}$  is the data covariance matrix after applying the double KL transform foreground filter,  $S$  is a real diagonal matrix, and  $I$  is the identity matrix. The diagonal elements of  $S$  give the expected signal–noise ratio in each mode. The

foreground filter is applied to the measured  $m$ -modes by simply computing

$$\mathbf{v}_{\text{filtered}} = \mathbf{W}^* \mathbf{L}^* \mathbf{v}. \quad (4.30)$$

In this paper we will repeat the analysis using three different values for the foreground filtering signal–foreground threshold  $\epsilon_{\text{filter}}$ . This will allow us to assess the performance of the foreground filter and degree to which residual foreground contamination may be affecting the measurement. We will adopt the terminology “strong,” “moderate,” and “mild” to mean:

|                                  |                                   |
|----------------------------------|-----------------------------------|
| $\epsilon_{\text{filter}} = 0.1$ | (“strong” foreground filtering)   |
| $\epsilon_{\text{filter}} = 1$   | (“moderate” foreground filtering) |
| $\epsilon_{\text{filter}} = 10$  | (“mild” foreground filtering).    |

Now we will build a physical intuition for understanding the operation of the double KL transform foreground filter.

Figure 4.7 illustrates the fractional increase in error bars associated with applying the moderate foreground filter. In the space of a cylindrically binned power spectrum, the action of the filter is to discard linear combinations of the dataset with low  $k_{\parallel}$  and low  $k_{\perp}$ . This manifests itself as a decrease in sensitivity—equivalently an increase in the error bars—in this region of parameter space. High  $k_{\parallel}$  modes are computed from rapid frequency differences, whereas low  $k_{\parallel}$  modes are slowly varying in frequency. Because the foreground emission is spectrally smooth, it tends to corrupt modes with low  $k_{\parallel}$ . The pattern of this contamination is known as the foreground wedge. However, the foreground filter additionally removes emission on large angular scales (low  $k_{\perp}$ ). This arises because the foreground filter is aware that the foreground emission is brighter on larger angular scales (see Figure 4.4 and Equation 4.18).

As illustrated in Figure 4.8, the foreground filter also tends to remove emission in two separate parts of the sky: low declinations that are never seen at high elevations from the OVRO-LWA, and high declinations around the North Celestial Pole (NCP). This filtering of high and low declinations can be seen in Figure 4.9, which is a Tikhonov-regularized image of the sky constructed from the post-filtered data.

The OVRO-LWA is a zenith pointing drift-scanning instrument. Therefore foreground emission located far from zenith has a large path difference between antennas. This large path difference leads to additional frequency structure that allows

the foreground emission to contaminate higher values of  $k_{\parallel}$  (Morales et al., 2012). Similarly, Thyagarajan et al. (2015) derived the impact of widefield effects on the foreground contamination and found that baseline foreshortening can lead to additional galactic synchrotron emission on large angular scales contaminating the measurement. This foreground emission from low-elevations is problematic. The double KL transform suppresses the contribution of these low elevations to the measurement.

Emission from the vicinity of the NCP is characterized by its low fringe-rate. As the Earth rotates, emission located here moves slowly through the fringes of the interferometer. Therefore this emission is predominantly characterized by low values of  $m$ . The foreground emission, however, is brightest relative to the cosmological 21 cm emission at low values of  $l$  (large angular scales). Because  $m \leq l$  for a given value of  $l$ , low values of  $m$  are disproportionately contaminated by the brightest diffuse components of the foreground emission. In fact, for the fiducial foreground and signal models presented in §4.4 and §4.4 respectively, the foreground–signal ratio of the most favorable mode is  $\propto m^{-3.5}$ . This is a reflection of the fact that emission with a higher fringe rate tends to be smaller in angular extent. Consequently, the foreground filter aggressively discards information from small values of  $m$  and the emission located at the NCP is collateral damage because it can be difficult to separate from the diffuse foreground emission. This can be seen in Figure 4.8 where increasing the strength of the foreground filter increases the area around the NCP that is down-weighted.

## 4.6 Results and Error Analysis

We will use a quadratic estimator to measure the spatial power spectrum of 21 cm fluctuations (Tegmark, 1997). In particular we estimate the coefficients  $p_{\alpha}$ , which are defined in Equation 4.21. As described by Padmanabhan et al. (2003), the observer may tune the estimator by selecting a windowing function that produces desired properties. For example, given the measured data  $\mathbf{v}$ , the full covariance matrix  $\mathbf{C}$ , and the Fisher information matrix  $\mathbf{F}$ , the unwindowed and minimum variance estimates of the power spectrum amplitude are

$$\hat{p}_{\alpha}^{\text{unwindowed}} = \sum_{\beta} [\mathbf{F}^{-1}]_{\alpha\beta} (q_{\beta} - b_{\beta}) \quad (4.31)$$

$$\hat{p}_{\alpha}^{\text{min. variance}} = \left( \sum_{\beta} F_{\alpha\beta} \right)^{-1} (q_{\beta} - b_{\beta}), \quad (4.32)$$

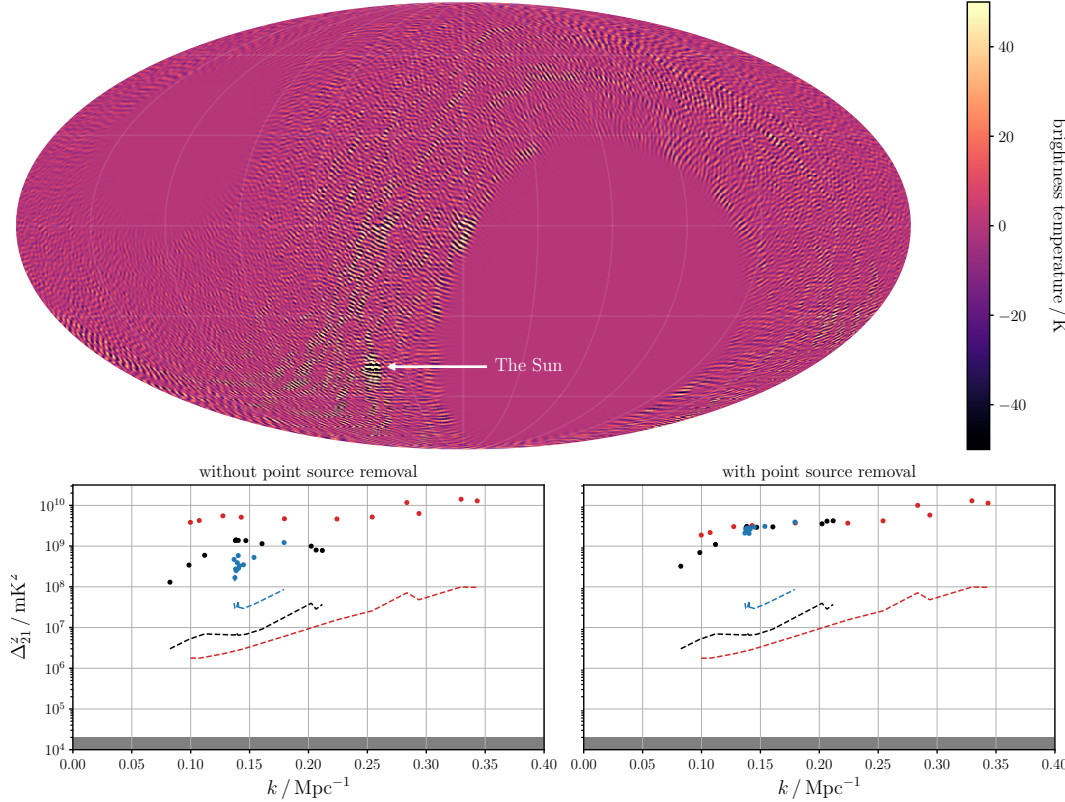


Figure 4.9: (top) Mollweide projected image of the sky after point source removal and moderate foreground filtering. The dominant residual feature in the residuals is associated with the Sun. (bottom) The power spectrum estimated without point source removal (left) and with point source removal (right) at a range of filter strengths. Points correspond to the estimated power spectrum amplitude and the dashed lines correspond to the computed thermal noise. Mild foreground filtering is red, moderate foreground filtering is black, and extreme foreground filtering is blue.

where

$$q_\alpha = \mathbf{v}^* \mathbf{C}^{-1} \frac{\partial \mathbf{C}}{\partial p_\alpha} \mathbf{C}^{-1} \mathbf{v} \quad (4.33)$$

$$b_\alpha = \text{tr} \left( \mathbf{C}^{-1} \frac{\partial \mathbf{C}}{\partial p_\alpha} \mathbf{C}^{-1} \mathbf{C}_{\text{noise}} \right) \quad (4.34)$$

$$F_{\alpha\beta} = \text{tr} \left( \mathbf{C}^{-1} \frac{\partial \mathbf{C}}{\partial p_\alpha} \mathbf{C}^{-1} \frac{\partial \mathbf{C}}{\partial p_\beta} \right). \quad (4.35)$$

Directly computing  $F_{\alpha\beta}$  from its definition is computationally expensive, and so we compute an approximation of the Fisher information matrix using the iterative Monte Carlo scheme described by Dillon et al. (2013).

We will make exclusive use of the minimum variance estimator in this paper because

it is relatively insensitive to errors in the Fisher information matrix, which are inevitable due to the Monte Carlo computation. Additionally, the unwindowed estimator can compound numerical errors when the condition number of  $\mathbf{F}$  is large.<sup>2</sup>

In Figure 4.9 we present the results of the quadratic estimator with and without point source removal, and across the range of foreground filter strengths. These estimates are, across the board, severely limited by systematic errors. This is readily apparent due to the extreme amplitude of the estimated power. We therefore interpret these measurements as upper limits  $\Delta_{21}^2 \lesssim (10^4 \text{ mK})^2$  at  $k \approx 0.10 \text{ Mpc}^{-1}$ .

As the strength of the foreground filter is increased more information is lost by the filter. This is seen in the window functions of the quadratic estimator. With mild foreground filtering, the window functions are roughly evenly spaced between  $k = 0.10 \text{ Mpc}^{-1}$  and  $0.35 \text{ Mpc}^{-1}$ . With extreme foreground filtering, all of the measurements are instead concentrated around  $k = 0.15 \text{ Mpc}^{-1}$ , which reflects the loss of information at other values of the wavenumber  $k$ .

After initial calibration and stationary component removal, we attempted to subtract the eight brightest point sources in the northern hemisphere in addition to the Sun. The brightest of these sources were removed with direction-dependent calibrations. The fainter sources were simply subtracted after fitting for their flux and position (attempting to account for ionospheric scintillation and refraction). The Sun was removed using a resolved source model. With mild foreground filtering, this point source removal leads to a  $\sim 2\times$  reduction in the power spectrum amplitude.

However, the efficacy of the foreground filter materially differs between the datasets where bright point sources have and have not been removed. Without point source removal, increasing the strength of the foreground filter leads to a reduction of the estimated power. This reflects the fact that the foreground filter is removing increasing amounts of foreground contamination. In contrast, if point sources have been subtracted, the power spectrum amplitude is insensitive to the strength of the foreground filter. While the point source removal routine leads to less foreground contamination in the absence of foreground filtering, it also restricts the effectiveness of the foreground filter. This suggests that the point source removal routine introduces additional errors into the dataset that inhibit the action of the foreground filter.

---

<sup>2</sup> The condition number of a matrix  $\mathbf{A}$  is  $\kappa(\mathbf{A}) = \|\mathbf{A}\| \|\mathbf{A}^{-1}\|$  and describes the error introduced when solving the linear equation  $\mathbf{Ax} = \mathbf{b}$  for the vector  $\mathbf{x}$ . As a general rule of thumb, if  $\log_{10} \kappa(\mathbf{A}) = N$ , one can expect to lose  $N$  digits of precision after computing  $\mathbf{A}^{-1}\mathbf{b}$ .

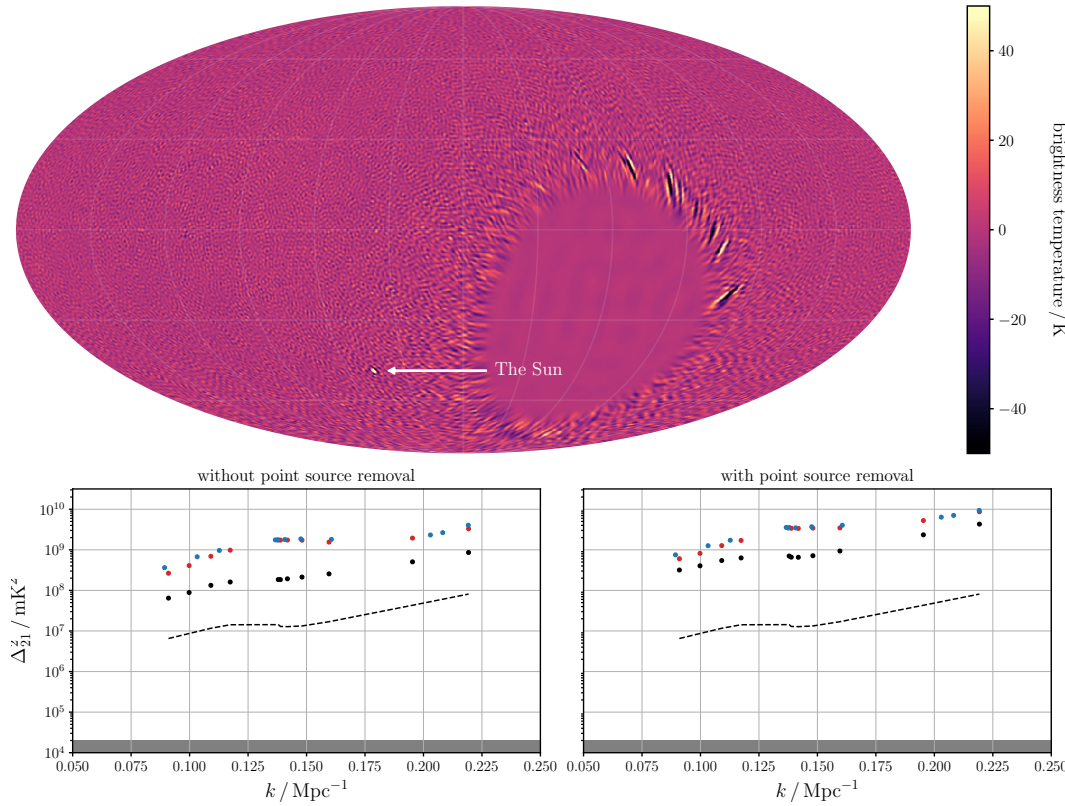


Figure 4.10: (top) Mollweide projection of the sky in galactic coordinates after differencing even and odd-numbered integrations. The Sun is the dominant artifact in this image due to the sporadic failure of source subtraction. Large residuals are also present at low declinations that do not rise above  $10^\circ$  elevation. These low-elevation artifacts are generated by RFI. (bottom) The power spectrum estimated without point source removal (left) and with point source removal (right). Point correspond to the estimated power spectrum amplitude and the dashed line corresponds to the computed thermal noise. Red and blue points are estimates from the even and odd numbered integrations respectively. Black points are estimates after computing the difference between the two halves of data.

We will now attempt to diagnose the source of these residual systematic errors that limit this measurement. While doing this, we will adopt the moderate foreground filter as the fiducial foreground filter due to its action as a compromise between the amount of foreground emission removed and resolution in the wavenumber  $k$ .

### Even–Odd Jackknife

Errors arising from variations on rapid timescales—the timescale of a single correlator dump—can be revealed through the comparison of results obtained data using only even-numbered integrations and the interleaving odd-numbered integrations.

These two halves of the dataset have independent thermal noise with additional errors due to ionospheric scintillation, RFI and source subtraction errors.

In prior work we observed that ionospheric scintillation generates  $\sim 10\%$  fluctuations in the flux of a point source on 13 s timescales at 73 MHz (Eastwood et al., 2018). The position of a source varies more slowly by up to  $4'$  on 10 min timescales. Therefore comparing even and odd-numbered integrations will reveal errors arising from ionospheric scintillation, but not necessarily from variable ionospheric refraction.

Figure 4.10 contains a map of the sky constructed from differencing the even and odd datasets (after point source removal). This map is almost featureless. If ionospheric scintillation was contributing a substantial amount of additional noise to the measurement, we would expect to see enhanced residuals in the vicinity of bright point sources. Instead, the dominant features are a  $\sim 50$  K residual at the location of the Sun, and some artifacts that manifest at low declinations that do not rise above  $10^\circ$  elevation (likely generated by RFI). We therefore conclude that over a long 28 hr integration, the ionospheric scintillation has averaged down and is not the dominant source of error.

The bottom panel of Figure 4.10 compares the amplitude of the estimated power spectrum after differencing the even and odd-numbered integrations. Differencing the two halves of the dataset cancels out the majority of the residual contamination of foreground emission into the measurement. Therefore the power spectrum decreases in amplitude. The improvement is roughly one order of magnitude before source subtraction and only a factor of 2–3 after source subtraction. Point source removal is conducted independently on each integration, sporadic errors and source subtraction residuals will therefore also tend to manifest on the timescale of a single integration. This measurement therefore suggests that source subtraction residuals could be a limiting factor for this estimate of the 21 cm power spectrum.

### **Day–Night Jackknife**

The dominant subtraction residual in the preceding section is associated with the Sun, which is a difficult source to cleanly subtract due to its complex structure. We can therefore split the data into two halves: data collected while the Sun is above the horizon, and below the horizon. The data collected during the night has a number of advantages. Specifically, subtraction residuals associated with the Sun cannot impact data collected during the night. Additionally the ionospheric Total Electron Content (TEC) is lower during the night because the Sun acts as

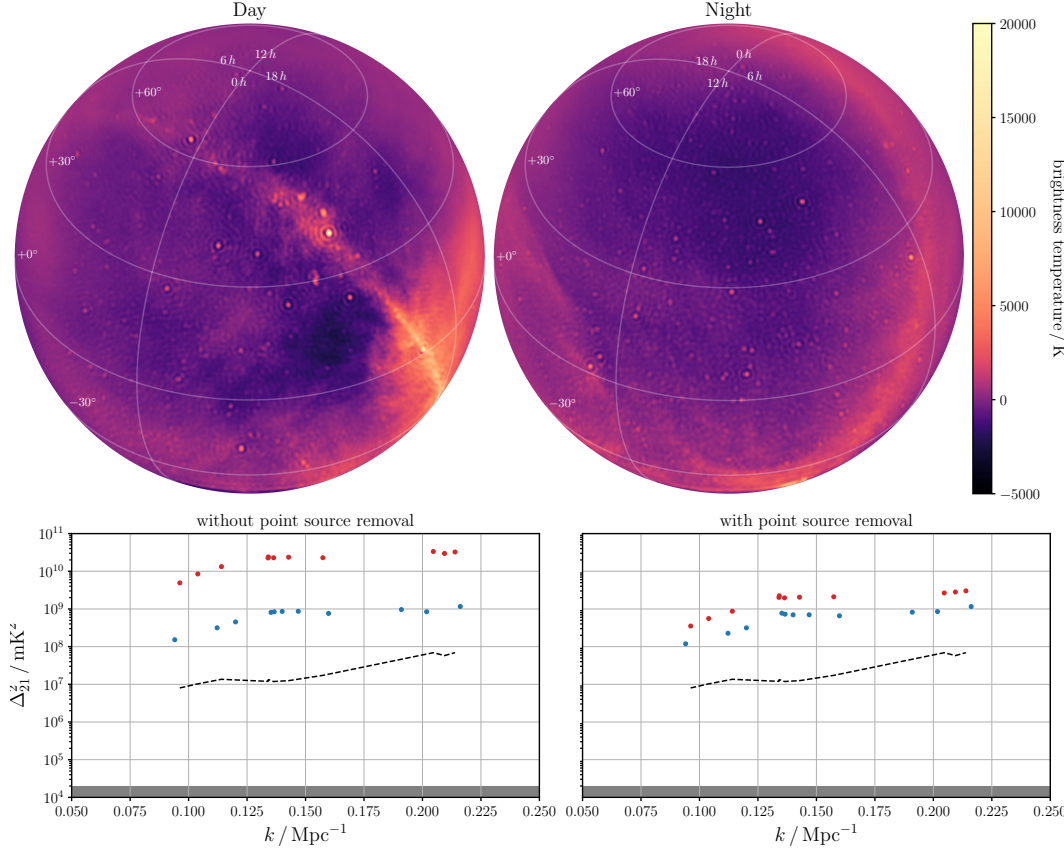


Figure 4.11: (top) Orthographic projection of the sky constructed from data collected only during the day (left), and only during the night (right). (bottom) The power spectrum estimated without point source removal (left) and with point source removal (right). Points correspond to the estimated power spectrum amplitude and the dashed line corresponds to the computed thermal noise. Measurements from the day are red, and measurements from the night are blue.

a source of ionization for the ionosphere. Specifically, the median vertical TEC measured within 200 km of OVRO rose to 20 TECU during the day, but drops to 6 TECU during the night. There were no geomagnetic storms during the observing period and the fact that these observations were collected during the winter months generally contributes to a reduction in the ionospheric TEC. Finally, due to the time of year, the sky temperature is lower at night. For these reasons, we generally expect an improvement in the nighttime data with respect to the daytime data.

In principle,  $m$ -mode analysis requires that data be collected for a full sidereal day because the  $m$ -modes are computed from the Fourier transform of the visibilities with respect to sidereal time. We relax that requirement here. When selecting half the data, we additionally apply a Blackman–Harris window function to prevent

ringing. Tikhonov-regularized images made from just the daytime and nighttime data can be seen in Figure 4.11. These dirty images serve as a proof of concept that  $m$ -mode analysis can reasonably be applied to datasets without a full sidereal day's worth of data.

We estimated the power spectrum from each half of data and the results are presented in Figure 4.11. Restricting the observations to nighttime-only leads to a substantial improvement in the power spectrum limits both with and without point source removal. In fact the measurements with and without point source removal are now comparable. This suggests the point source subtraction residuals are less of an issue in the nighttime data due to the fact that (due to the time of year) there are fewer bright point sources that were removed.

### **$xx$ - $yy$ Jackknife**

The polarization angle of linearly polarized emission rotates as it propagates through a magnetized plasma (e.g., Jelić et al., 2014). The rotation angle is  $\propto \lambda^2$ , where  $\lambda$  is the wavelength of the radiation. Therefore instrumental polarization leakage from a linear polarization (Stokes  $Q$  or Stokes  $U$ ) into total intensity (Stokes  $I$ ) can introduce additional spectral structure into the foreground emission that is not accounted for in our currently unpolarized analysis.

If Faraday-rotated linearly polarized emission is a problem, it will be exacerbated by computing the power spectrum from the  $xx$  correlations and  $yy$  correlations separately. For this comparison, the transfer matrix  $\mathbf{B}$  must be recomputed using the correct response pattern for the individual dipoles. An image of the sky computed from the difference of the  $xx$  and  $yy$  correlations is shown in Figure 4.12. This map is related to the linear polarization of the sky, but does not account for the full polarization of the beam, and therefore includes some amount of instrumental polarization.

We estimated the 21 cm power spectrum from the  $xx$  and  $yy$  correlations. This estimate is shown in Figure 4.12. The estimates are comparable to the total intensity estimate and we therefore conclude that polarization leakage is not currently a major source of systematic error.

### **Calibration Errors**

Multiple authors have investigated the impact of calibration errors on an experiment's ability to separate foreground emission from the cosmological 21 cm signal (Barry

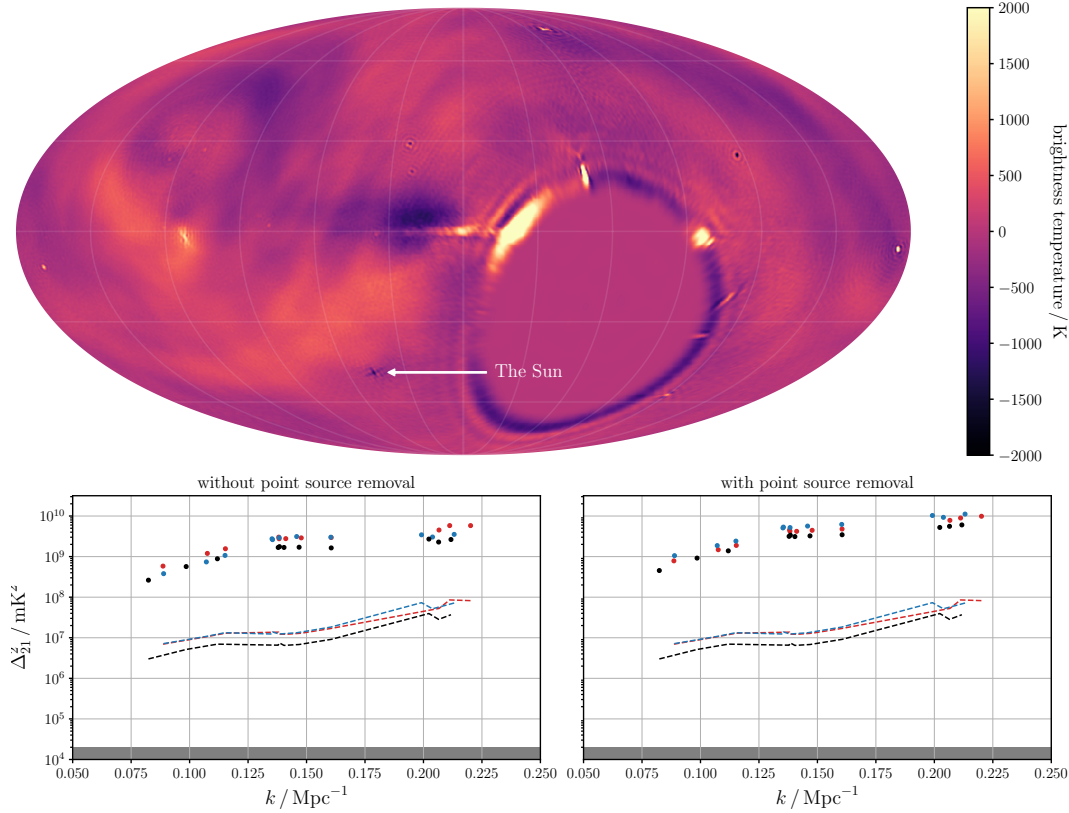


Figure 4.12: (top) Mollweide projection of the sky in galactic coordinates after differencing the  $xx$  and  $yy$  correlations. Note that this is not true linear polarization because it does not account for the full polarization of the antenna response pattern. (bottom) The power spectrum estimated without point source removal (left) and with point source removal (right). Point correspond to the estimated power spectrum amplitude and the dashed line corresponds to the computed thermal noise. Red and blue points are estimates from the  $xx$  and  $yy$  correlations respectively. Black points are estimates from the mean of the  $xx$  and  $yy$  correlations.

et al., 2016; Ewall-Wice et al., 2017). In this section we will compute the impact of calibration errors on the double KL transform foreground filter.

In this calculation will simulate a realistic set of visibilities for the foreground emission, and introduce errors into the calibration before applying the double KL transform filter. Finally we will estimate the power spectrum amplitude as a way to characterize the amount of contamination associated with the calibration errors.

The angular structure of the foreground model used here is measured from the data itself (shown in the bottom panel of Figure 4.2), but the frequency dependence of this emission is chosen to be a power-law with a fiducial spectral index of  $-2.3$ . This spectral index was chosen to be consistent with the results reported by LEDA

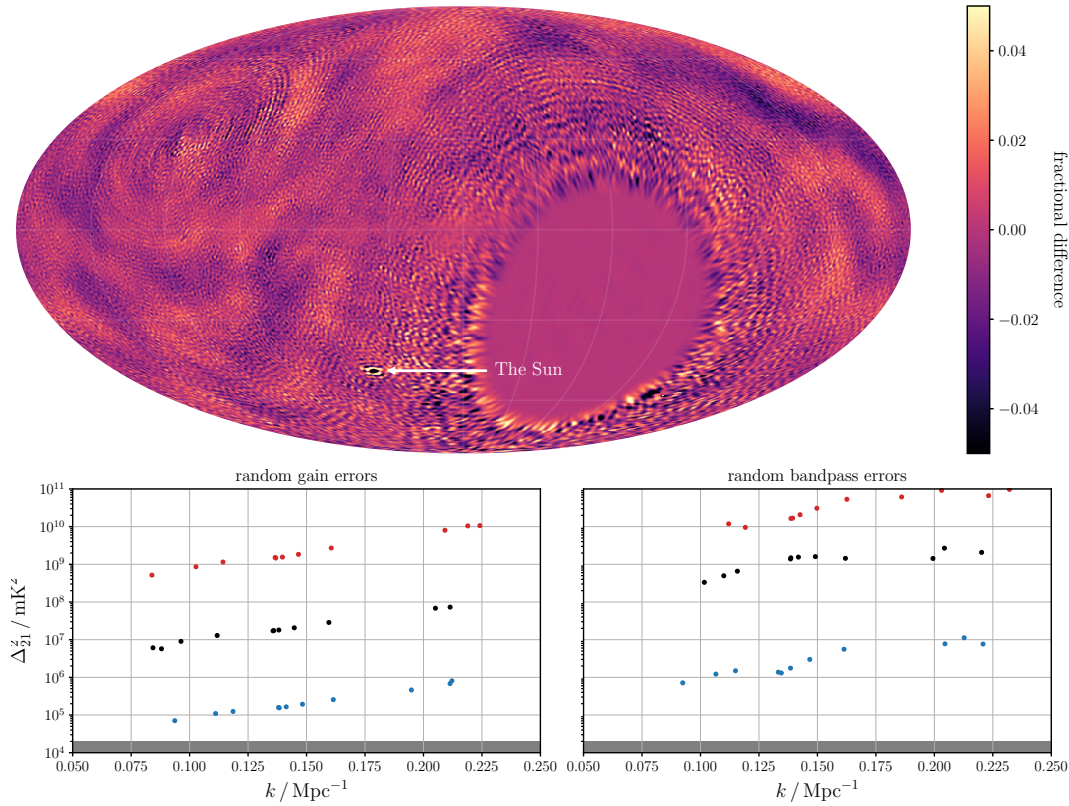


Figure 4.13: (top) Mollweide projection of the sky in galactic coordinates after differencing two adjacent 240 kHz frequency channels. (bottom) Simulated power spectrum estimates as a result of a foreground model and gain errors that are incoherent between antennas (left) and coherent between antennas (right). Blue corresponds to 0.1% errors, black corresponds to 1% errors, and red corresponds to 10% errors in the complex gains.

(Price et al., 2018), but due to the small fractional bandwidth of this measurement, we expect these results to be insensitive to the specific choice of spectral index. The set of  $m$ -modes we expect to measure with the interferometer  $\mathbf{v}_{\text{simulated}}$  is computed:

$$\mathbf{v}_{\text{simulated}} = \mathbf{B}\mathbf{a}_{\text{simulated}}, \quad (4.36)$$

where  $\mathbf{B}$  is the transfer matrix, and  $\mathbf{a}_{\text{simulated}}$  is a vector of the spherical harmonic coefficients of the foreground model.

At this point the simulated  $m$ -modes are corrupted with calibration errors. We explore two possibilities:

1. each antenna and frequency channel receives an incorrect gain calibration

2. each frequency channel receives an incorrect gain calibration, but this error is coherent across antennas

In each case, the gain errors are drawn from a complex normal distribution, and the amplitude of the error is varied between 0.1%, 1%, and 10%. The former case is coined “random gain errors” to indicate that each antenna is given an error in its complex gain calibration. The latter case is coined “random bandpass errors” to indicate that the overall bandpass of the interferometer is perturbed. The impact of these calibration errors can be seen in Figure 4.13.

In order to avoid biasing the 21 cm power spectrum, these results indicate that the gain calibration must be derived to an accuracy better than 0.1%. A general rule of thumb for the OVRO-LWA is that for equal amplitude errors, the foreground contamination generated by bandpass errors that are coherent across all antennas are an order of magnitude worse than for the random gain errors (in units of  $\Delta_{21}^2$ ). Therefore to achieve a comparable level of foreground contamination, the overall bandpass of the interferometer must be known to better than 0.01%.

The dataset presented in this paper is systematically limited at roughly  $\Delta_{21}^2 \sim (10^4 \text{ mK})^2$ . These limits are therefore consistent with  $\sim 1\%$  errors in the overall bandpass of the interferometer. The top panel of Figure 4.13 therefore presents the fractional difference in the sky images between two adjacent frequency channels (after averaging down to 240 kHz channel resolution). The residuals in this sky map are typically 2%–3%, but generally do not correlate with the sky brightness. We therefore conclude that between adjacent 240 kHz channels, the bandpass error is less than 1%.

In fact, the structure of the residuals in Figure 4.13 suggests a different terrestrial source. Terrestrial sources of radio emission do not move through the sky at a sidereal rate. Therefore when constructing images of the sky, this contaminating emission tends to be smeared along rings of constant declination. These ring-like structures are clearly visible in Figure 4.13 alongside some larger scale diffuse structures.

However, if we attribute the residual emission entirely to gain errors, then these simulations suggest that the antenna gains are known only to within a couple percent, which when considered alongside the RFI that contaminates the measurement, is likely sufficient to explain the current systematic limitations of our dataset.

#### 4.7 Conclusion

In this paper we estimated the amplitude of the 21 cm power spectrum of the Cosmic Dawn with 28 hr of data from the OVRO-LWA. This measurement was severely limited by systematic errors and therefore we interpret our measurements as upper limits, which are currently the most sensitive at this epoch and the first measurement at  $z > 18$ . We measured  $\Delta_{21}^2 \lesssim (10^4 \text{ mK})^2$  at  $k \approx 0.10 \text{ Mpc}^{-1}$ .

In making this measurement, we demonstrated the first application of the double KL transform foreground filter to a measured dataset. We demonstrated that the application of this foreground filter can lead to improved power spectrum limits, and in combination with Tikhonov-regularized imaging, we developed a physical intuition for the action of the foreground filter. The double KL transform derives its action from models for the foreground and 21 cm signal covariance. We measured the angular power spectrum of the foreground emission and found that the power-law index appears to steepen on large angular scales ( $l < 50$ ). The 21 cm signal covariance is derived from the flat-sky approximation, which we derive in Appendix .1.

Although application of the foreground filter leads to some improvement in our measurement of the 21 cm power spectrum, the improvement was relatively modest. This is essentially a reflection of the fact that the true covariance of the data does not match the expectations of the models. We performed a series of jackknife tests and simulations that appear to implicate a combination of source subtraction errors, terrestrial interference, and calibration errors as limiting factors in this measurement. A detection of the Cosmic Dawn 21 cm spatial power spectrum will require that gain errors are restricted to less than 0.1% and bandpass errors to less than 0.01%. Future work will focus on improving the instrumental calibration and source removal, which will help to prevent foreground emission leaking through the measurement and into the power spectrum estimate.

## ACKNOWLEDGMENTS

This material is based in part upon work supported by the National Science Foundation under grants AST-1654815 and AST-1212226. The OVRO-LWA project was initiated through the kind donation of Deborah Castleman and Harold Rosen.

Part of this research was carried out at the Jet Propulsion Laboratory, California Institute of Technology, under a contract with the National Aeronautics and Space Administration, including partial funding through the President's and Director's Fund Program.

This work has benefited from open-source technology shared by the Collaboration for Astronomy Signal Processing and Electronics Research (CASPER). We thank the Xilinx University Program for donations; NVIDIA for proprietary tools, discounts, and donations; and Digicom for collaboration on the manufacture and testing of DSP processors.

We thank the Smithsonian Astrophysical Observatory Submillimeter Receiver Lab for the collaboration of its members.

Development, adaptation, and operation of the LEDA real-time digital signal-processing systems at OVRO-LWA have been supported in part by NSF grants AST/1106059, PHY/0835713, and OIA/1125087.

### **.1 Converting a Spatial Power Spectrum to an Angular Power Spectrum**

The multi-frequency angular power spectrum  $C_l(\nu, \nu')$  is measured from the spherical harmonic coefficients of the sky  $a_{lm}(\nu)$  at the frequencies  $\nu$  and  $\nu'$ :

$$C_l^{21}(\nu, \nu') = \frac{1}{2l+1} \sum_{m=-l}^l \left\langle a_{lm}^{21}(\nu) a_{lm}^{21*}(\nu') \right\rangle, \quad (37)$$

where the angled brackets should be understood as an ensemble average over sky realizations. Here the average over  $m$  is indicated with an explicit sum to distinguish it from the ensemble average.

The spherical harmonic coefficients themselves are computed from an integral over the 21 cm brightness temperature  $T_\nu^{21}(\vec{r})$  over a spherical shell of the universe.

$$a_{lm}^{21}(\nu) = \int T_\nu^{21}(\vec{r}) Y_{lm}^*(\hat{r}) \delta(r - r_z) d^3r, \quad (38)$$

where  $Y_{lm}(\hat{r})$  is a spherical harmonic function, and the Dirac delta function  $\delta(r - r_z)$  is used to pick out the spherical shell of the universe at the comoving distance  $r_z$  to the redshift  $z$ .

The 21 cm brightness temperature is related to the power spectrum  $P_z^{21}(\vec{k})$  through its Fourier transform.

$$T_v^{21}(\vec{r}) = \int T_v^{21}(\vec{k}) e^{i\vec{k}\cdot\vec{r}} \frac{d^3k}{(2\pi)^3} \quad (39)$$

$$\langle T_v(\vec{k}) T_{v'}(\vec{k}') \rangle = (2\pi)^3 \delta^3(\vec{k} - \vec{k}') P_z^{21}(\vec{k}) \quad (40)$$

Finally, we will need the “plane wave expansion” that describes a plane wave in terms of spherical harmonics:

$$e^{i\vec{k}\cdot\vec{r}} = 4\pi \sum_{lm} i^l j_l(kr) Y_{lm}(\hat{r}) Y_{lm}^*(\hat{k}), \quad (41)$$

where the function  $j_l(kr)$  is the spherical Bessel function of the first kind.

Putting this all together we can find

$$\begin{aligned} C_l^{21}(v, v') &= \frac{1}{2l+1} \sum_{m=-l}^l \left\langle \iiint T_v^{21}(\vec{k}) T_{v'}^{21*}(\vec{k}') e^{i(\vec{k}\cdot\vec{r}-\vec{k}'\cdot\vec{r}')} Y_{lm}^*(\hat{r}) Y_{lm}(\hat{r}') \delta(r - r_z) \delta(r' - r_{z'}) d^3r d^3r' \frac{d^3k}{(2\pi)^3} \frac{d^3k'}{(2\pi)^3} \right\rangle \\ &= \frac{4\pi(-i)^l}{2l+1} \sum_{m=-l}^l \left\langle \iiint T_v^{21}(\vec{k}) T_{v'}^{21*}(\vec{k}') e^{i\vec{k}\cdot\vec{r}} j_l(k'r_z) Y_{lm}^*(\hat{r}) Y_{lm}(\hat{k}') \delta(r - r_z) d^3r \frac{d^3k}{(2\pi)^3} \frac{d^3k'}{(2\pi)^3} \right\rangle \\ &= \frac{(4\pi)^2}{2l+1} \sum_{m=-l}^l \left\langle \iint T_v^{21}(\vec{k}) T_{v'}^{21*}(\vec{k}') j_l(kr_z) j_l(k'r_{z'}) Y_{lm}^*(\hat{k}) Y_{lm}(\hat{k}') \frac{d^3k}{(2\pi)^3} \frac{d^3k'}{(2\pi)^3} \right\rangle \\ &= \frac{(4\pi)^2}{2l+1} \sum_{m=-l}^l \int P_z^{21}(\vec{k}) j_l(kr_z) j_l(kr_{z'}) Y_{lm}^*(\hat{k}) Y_{lm}(\hat{k}) \frac{d^3k}{(2\pi)^3} \end{aligned}$$

Where in the first two steps we used the plane-wave expansion, and in the final step we used the definition of the spatial power spectrum.

At this point if we assume that the power spectrum is isotropic and has no dependence on the orientation of the wave vector  $\hat{k}$ , then the angular component of the remaining integral can be performed to find:

$$C_l^{21}(v, v') = \frac{2}{\pi} \int P_z^{21}(k) j_l(kr_z) j_l(kr_{z'}) k^2 dk. \quad (42)$$

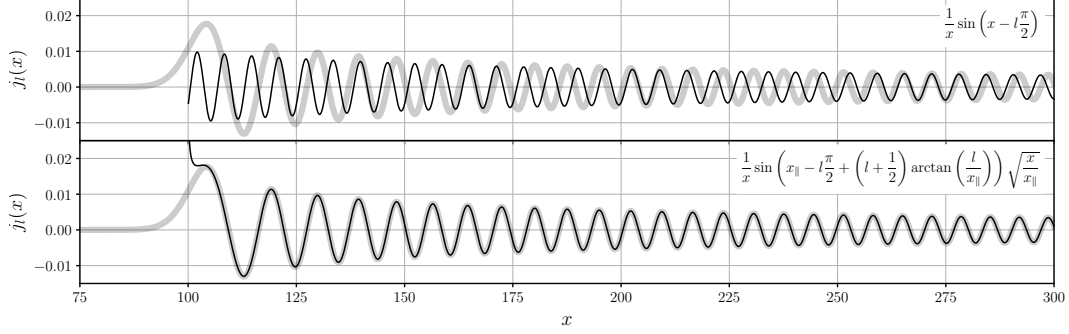


Figure .14: A comparison of two approximations (thin black lines) to the spherical Bessel function  $j_l(x)$  with  $l = 100$  (thick gray lines). The top panel shows the approximation derived from the limiting behavior of  $j_l(x)$  as  $x \rightarrow \infty$ . This is a poor approximation near  $x \sim l$ . The bottom panel shows the approximation derived from the method of steepest descent. This approximation maintains the same limiting behavior as  $x \rightarrow \infty$  and greatly improves the accuracy of the approximation near  $x \sim l$ .

Typically  $r_z \sim 10,000$  Mpc and  $k \sim 0.1$  Mpc $^{-1}$  so the spherical Bessel functions  $j_l(x)$  are typically evaluated in the limit of  $l < x < l^2$ . Equation 42 is exact for an isotropic power spectrum, but in practice integrals over the product of two spherical Bessel functions are numerically challenging due to their oscillatory behavior, so we will look for a scheme to approximate this integral. This approximation is simple in the regimes where  $x \ll l$  and  $x \gg l$ , because

$$\lim_{x \rightarrow 0} j_l(x) \propto x^l \approx 0 \quad (43)$$

$$\lim_{x \rightarrow \infty} j_l(x) = \frac{1}{x} \sin\left(x - l\frac{\pi}{2}\right) + O\left(\frac{l^2}{x^2}\right). \quad (44)$$

However, we are primarily interested in the intermediate regime where a better approximation can be obtained using the method of steepest descent (this method is also used, for example, to derive Stirling's approximation to  $\log n!$  for large  $n$ ). Starting with the integral representation of the spherical Bessel functions, the integration contour is deformed slightly to pass through saddle points of the integrand, approaching along paths of steepest descent. This allows the integral to be approximated as a Gaussian integral, which can be analytically evaluated to

$$j_l(x) \approx \frac{1}{x} \sin\left(x_{\parallel} - l\frac{\pi}{2} + \left(l + \frac{1}{2}\right) \arctan\left(\frac{l}{x_{\parallel}}\right)\right) \sqrt{\frac{x}{x_{\parallel}}}, \quad (45)$$

where we have suggestively defined  $x_{\parallel} = \sqrt{x^2 - l^2}$ . This approximation holds for  $l \gg 1$  and  $x > l$  (see Figure .14). The product of the two spherical Bessel functions

in Equation 42 therefore results in rapid oscillations on top of a slower beat frequency. After computing the integral—provided the power spectrum is sufficiently smooth—the rapid oscillations will average down. Therefore this integral can be approximated using only the latter term:

$$C_l^{21}(\nu, \nu') \approx \frac{1}{\pi r_z r_{z'}} \int P_z^{21}(k_\perp, k_\parallel) \cos \left( k_\parallel \Delta r_z + \left( l + \frac{1}{2} \right) \arctan \left( \frac{\Delta r_z / r_z}{k_\perp / k_\parallel + k_\parallel / k_\perp} \right) \right) dk_\parallel, \quad (46)$$

where  $k_\parallel = \sqrt{k^2 - k_\perp^2}$ ,  $k_\perp = l/r_z$ , and  $\Delta r_z = r_{z'} - r_z$ . Typically for nearby frequency channels, the argument to the arctangent will be small, and consequently we arrive at the “flat-sky approximation” used by Bharadwaj & Ali (2005) and Datta et al. (2007):

$$C_l^{21}(\nu, \nu') \approx \frac{1}{\pi r_z r_{z'}} \int P_z^{21}(k_\perp, k_\parallel) \cos(k_\parallel \Delta r_z) dk_\parallel. \quad (47)$$

In order to derive this approximation we required  $l \gg 1$ ,  $\Delta r_z / r_z \ll k_\parallel / k_\perp$ , and that the power spectrum is smooth on scales that allow the rapid oscillations of the spherical Bessel functions to average down. The flat-sky approximation is advantageous because piecewise linear representations of the power spectrum can be rapidly evaluated analytically. However, we separately need to verify that the piecewise linear representation is smooth enough to permit this approximation.

## Bibliography

- Ali, Z. S., Parsons, A. R., Zheng, H., et al. 2015, ApJ, 809, 61
- Anderson, E., Bai, Z., Dongarra, J., et al. 1990, in Proceedings of the 1990 ACM/IEEE Conference on Supercomputing, Supercomputing '90 (Los Alamitos, CA, USA: IEEE Computer Society Press), 2–11. <http://d1.acm.org/citation.cfm?id=110382.110385>
- Anderson, M. M., Hallinan, G., Eastwood, M. W., et al. 2017, ArXiv e-prints, arXiv:1711.06665
- Baars, J. W. M., Genzel, R., Pauliny-Toth, I. I. K., & Witzel, A. 1977, A&A, 61, 99
- Barkana, R. 2018, Nature, 555, 71
- Barry, N., Hazelton, B., Sullivan, I., Morales, M. F., & Pober, J. C. 2016, MNRAS, 461, 3135
- Beardsley, A. P., Hazelton, B. J., Sullivan, I. S., et al. 2016, ApJ, 833, 102
- Bharadwaj, S., & Ali, S. S. 2005, MNRAS, 356, 1519

- Bowman, J. D., Rogers, A. E. E., Monsalve, R. A., Mozdzen, T. J., & Mahesh, N. 2018, *Nature*, 555, 67
- Datta, K. K., Choudhury, T. R., & Bharadwaj, S. 2007, *MNRAS*, 378, 119
- DeBoer, D. R., Parsons, A. R., Aguirre, J. E., et al. 2017, *PASP*, 129, 045001
- Dillon, J. S., Liu, A., & Tegmark, M. 2013, *Phys. Rev. D*, 87, 043005
- Dowell, J., & Taylor, G. B. 2018, *ApJ*, 858, L9
- Eastwood, M. W., Anderson, M. M., Monroe, R. M., et al. 2018, *AJ*, 156, 32
- Ewall-Wice, A., Chang, T.-C., Lazio, J., et al. 2018, ArXiv e-prints, arXiv:1803.01815
- Ewall-Wice, A., Dillon, J. S., Liu, A., & Hewitt, J. 2017, *MNRAS*, 470, 1849
- Ewall-Wice, A., Dillon, J. S., Hewitt, J. N., et al. 2016, *MNRAS*, 460, 4320
- Fialkov, A., Barkana, R., & Cohen, A. 2018, *Physical Review Letters*, 121, 011101
- Fialkov, A., Barkana, R., Pinhas, A., & Visbal, E. 2014, *MNRAS*, 437, L36
- Fialkov, A., Barkana, R., Visbal, E., Tseliakhovich, D., & Hirata, C. M. 2013, *MNRAS*, 432, 2909
- Field, G. B. 1958, *Proceedings of the IRE*, 46, 240
- Furlanetto, S. R., Oh, S. P., & Briggs, F. H. 2006, *Phys. Rep.*, 433, 181
- Greig, B., & Mesinger, A. 2017, *MNRAS*, 472, 2651
- . 2018, *MNRAS*, 477, 3217
- Haslam, C. G. T., Klein, U., Salter, C. J., et al. 1981, *A&A*, 100, 209
- Haslam, C. G. T., Salter, C. J., Stoffel, H., & Wilson, W. E. 1982, *A&AS*, 47, 1
- Helmboldt, J. F., & Kassim, N. E. 2009, *AJ*, 138, 838
- Hicks, B. C., Paravastu-Dalal, N., Stewart, K. P., et al. 2012, *PASP*, 124, 1090
- Jelić, V., de Bruyn, A. G., Mevius, M., et al. 2014, *A&A*, 568, A101
- Kaurov, A. A., Venumadhav, T., Dai, L., & Zaldarriaga, M. 2018, ArXiv e-prints, arXiv:1805.03254
- Mitchell, D. A., Greenhill, L. J., Wayth, R. B., et al. 2008, *IEEE Journal of Selected Topics in Signal Processing*, 2, 707
- Morales, M. F., Hazelton, B., Sullivan, I., & Beardsley, A. 2012, *ApJ*, 752, 137

- Mozdzen, T. J., Bowman, J. D., Monsalve, R. A., & Rogers, A. E. E. 2017, MNRAS, 464, 4995
- Offringa, A. R., McKinley, B., Hurley-Walker, N., et al. 2014, MNRAS, 444, 606
- Paciga, G., Albert, J. G., Bandura, K., et al. 2013, MNRAS, 433, 639
- Padmanabhan, N., Seljak, U., & Pen, U. L. 2003, New A, 8, 581
- Parsons, A. R., Pober, J. C., Aguirre, J. E., et al. 2012, ApJ, 756, 165
- Patil, A. H., Yatawatta, S., Koopmans, L. V. E., et al. 2017, ApJ, 838, 65
- Planck Collaboration, Ade, P. A. R., Aghanim, N., et al. 2016, A&A, 594, A13
- Price, D. C., Greenhill, L. J., Fialkov, A., et al. 2018, MNRAS, 478, 4193
- Pritchard, J. R., & Loeb, A. 2012, Reports on Progress in Physics, 75, 086901
- Salvini, S., & Wijnholds, S. J. 2014, A&A, 571, A97
- Santos, M. G., Cooray, A., & Knox, L. 2005, ApJ, 625, 575
- Shaw, J. R., Sigurdson, K., Pen, U.-L., Stebbins, A., & Sitwell, M. 2014, ApJ, 781, 57
- Shaw, J. R., Sigurdson, K., Sitwell, M., Stebbins, A., & Pen, U.-L. 2015, Phys. Rev. D, 91, 083514
- Singh, S., Subrahmanyam, R., Udaya Shankar, N., et al. 2018, ApJ, 858, 54
- Taylor, G. B., Carilli, C. L., & Perley, R. A., eds. 1999, Astronomical Society of the Pacific Conference Series, Vol. 180, Synthesis Imaging in Radio Astronomy II
- Tegmark, M. 1997, Phys. Rev. D, 55, 5895
- Thyagarajan, N., Jacobs, D. C., Bowman, J. D., et al. 2015, ApJ, 804, 14
- Vedantham, H., Udaya Shankar, N., & Subrahmanyam, R. 2012, ApJ, 745, 176
- Venumadhav, T., Chang, T.-C., Doré, O., & Hirata, C. M. 2016, ApJ, 826, 116
- Venumadhav, T., Oklopčić, A., Gluscevic, V., Mishra, A., & Hirata, C. M. 2017, Phys. Rev. D, 95, 083010
- Wouthuysen, S. A. 1952, AJ, 57, 31

*Appendix A***CONCLUSION**